Probing Extraordinary Nanoscale Energy Transfer Using Bimaterial Microcantilevers
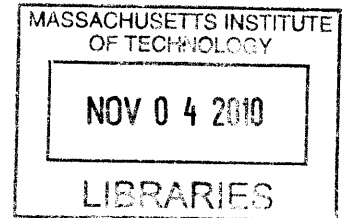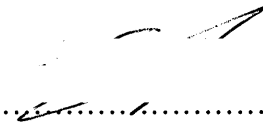
By

Sheng Shen

Submitted to the Department of Mechanical Engineering
in Partial Fulfillment of the Requirements for the Degree of
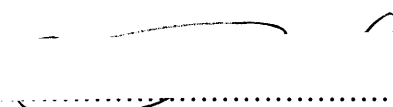Doctor of Philosophy in Mechanical Engineering

at the
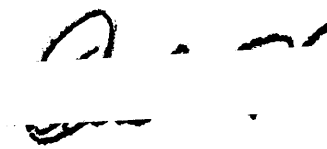Massachusetts Institute of Technology
September 2010

Signature of Author..
Department of Mechanical Engineering
July 31, 2010

Certified by...
Gang Chen
Carl Richard Soderberg Professor of Power Engineering
Thesis Supervisor

Accepted by..
David E. Hardt
Chairman, Department Committee on Graduate Students

Probing Extraordinary Nanoscale Energy Transfer Using Bimaterial Microcantilevers

By

Sheng Shen

Abstract

Nanostructured materials have recently drawn a great deal of attention in the field of energy research such as for solar photovoltaic, thermophotovoltaic and thermoelectric applications. The energy transport properties of nanostructures can differ greatly from their bulk counterparts because the characteristic dimensions of nanostructures are often comparable with the wavelength or the mean free path of energy carriers such as photons, phonons and electrons. Due to the small dimensions, probing energy transfer at the nanoscale is extremely challenging.

By developing new experimental techniques based on the bi-material microcantilevers used in Atomic Force Microscopes (AFM), this thesis has studied several extraordinary energy transfer phenomena at the nanoscale including near-field radiation beyond Planck's law, high thermal conductivity polymers and the optical absorption of micro/nanostructures. First, surface phonon polaritons, which is one type of electromagnetic surface waves, are demonstrated to enhance the thermal radiation between two surfaces at small gaps by measuring radiation heat transfer between a microsphere and a flat surface down to a 30 nm separation. The corresponding heat transfer coefficients at nanoscale gaps are three orders of magnitude larger than that of the Planck's blackbody radiation limit. This work will have practical impacts in areas such as thermophotovoltaic energy conversion, radiative cooling, and magnetic data recording. Next, a new technique is developed to fabricate ultra-drawn polyethylene nanofibers. We demonstrated that these ultradrawn nanofibers can have a thermal conductivity as high as ~ 100 W/m.K, which is about a 3 orders of magnitude enhancement compared to that of bulk polymers. Such high thermal conductivity polymers can potentially provide a cheaper alternative to conventional metal-based heat transfer materials. Finally, an experimental setup is presented to directly measure the spectral absorption of individual micro/nanostructures in applications to solar photovoltaics. Further refinement on experimental technique and characterization using the platform will guide the optimization of dimension, shape, and materials selections of nanostructures in order to maximize the efficiencies of solar cells.

Thesis Supervisor: Gang Chen
Title: Carl Richard Soderberg Professor of Power Engineering

Dedication

To my mother and my wife.

Acknowledgements

The opportunity to study at MIT for the past five years turned out to be one of most fortunate things in my life. I owe a great deal to the people who helped me throughout my PhD experience at MIT.

I have to show my foremost and deepest thanks to my thesis advisor and mentor, Prof. Gang Chen. In 2003, Prof. Chen first picked me from China. Unfortunately, I was not able to come to US at that time. When everyone including myself thought that I had missed a chance to admit MIT, Prof. Chen offered me a second opportunity to have me as his student in 2005. I am eternally grateful for his faith and confidence he showed me from the beginning. During my PhD study, he was intensively involved in each step of my research and gave me his guidance. His attitude and strictness on research helped me grow and become a mature researcher. His passion and optimism on research always encouraged me to solve hard problems. I am also grateful for his dedication to my career development. He has been very supportive for my faculty job searching in each aspect, and helped me find a postdoc position.

I was incredibly fortunate to have Prof. Mildred Dresselhaus, Prof. Borivoje Mikic, Prof. John H. Lienhard V, and Prof. Marin Soljacic in my thesis committee. Prof. Dresselhaus is remarkable. Her vision and philosophy on research have always inspired me to do high-quality work. My thesis was significantly improved by her meticulous and insightful comments. I really appreciate her time, energy and guidance on my thesis. Prof. Mikic is a heat transfer expert and was my heat transfer teacher at MIT. His insight and perspective were extremely helpful in my thesis research. I am also grateful for his constant encouragement on my thesis work. Prof. Lienhard is a heat transfer expert as well. The inspirational discussion with him greatly improved my thesis research. His view on energy research made me more confident on working on this field. Prof. Soljacic is truly a genius and a role model for junior professors. His expertise and insights on photonics were particularly instrumental for my thesis research on thermal radiation and optical absorption. I am also deeply grateful for all their recommendations in my faculty position applications.

Table of Contents

List of Figures

14

Chapter 1: Introduction

1.1 Nanoscale energy transfer

Nanostructured materials have recently drawn a great deal of attention in the field of energy research such as for solar photovoltaic, thermophotovoltaic and thermoelectric applications [1, 2]. The energy transport properties of nanostructures can differ greatly from their bulk counterparts because the characteristic dimensions of nanostructures are often comparable with the wavelength or the mean free path of energy carriers such as photons, phonons and electrons [3]. At the nanoscale, the properties of materials can be engineered to increase the energy density or energy conversion efficiencies.

Let us consider a few examples in the literature in which people have explored nanoscale effects for energy research. For solar energy conversion, nanostructures such as nanowires [4] and nanoparticles [5], as shown in Figs. 1-1 (a) and (b), have been proposed to strongly scatter photons because their dimensions are comparable with photon wavelength, and therefore more light can be absorbed. On the other hand, nanostructured semiconductors can work as the active layer of solar cells. Due to the small dimension of the nanostructures, they can also increase the charge collection efficiency for solar cells [4]. Thermophotovoltaic and thermoelectric systems are both capable of directly converting heat into electricity to harness heat sources such as

geothermal heat, solar heat and waste heat dissipated in energy conversion processes. In the case of thermophotovoltaics [6], photons are emitted from various heat sources, and photovoltaic cells are then used to convert infrared photons into electricity. In Fig. 1-1 (c), a microscopic spacer is designed by the company MPTV (Micron-gap Thermo Photovoltaics) to support photovoltaic cells in order to achieve a nanoscale gap between the heat source and photovoltaic cells [7]. In this design, the photon flux across the nanoscale gap can be increased by several orders of magnitude over the prediction from Planck's blackbody radiation law. In Chapter 3 of this thesis, this topic will be discussed in more detail. Thermoelectric materials are similar with thermocouples which utilize the temperature difference to generate electricity [8-11]. Their conversion efficiencies are determined by the Figure of Merit ZT

$$ZT = \frac{S^2 \sigma T}{k} \tag{1-1}$$

where S is the Seebeck coefficient that is a measure of the magnitude of an induced thermal electric voltage in response to a temperature difference, σ is the electrical conductivity, k is the thermal conductivity, and T is the average temperature. A thermoelectric material with a good efficiency, for example, 20 % will have a large Seebeck coefficient to maximize the induced voltage, a large electrical conductivity to minimize the joule heating, and a small thermal conductivity to minimize the heat loss from the hot side to the cold side. As theory predicts in Fig. 1-1 (d), when the structure becomes smaller, the Figure of Merit is higher [11]. This is because, as the size of the structure becomes smaller, its boundaries can strongly scatter phonons for heat conduction and therefore reduce the thermal conductivity [8, 9]. From these examples

discussed above, apparently, being able to exploit such nanoscale effects holds great potential in the field of energy research.

(a)

Cu/Au contact
CdTe
CdS nanopillar
AAM
In contact
PDMS

(Fan, Nature Mat., 2009)

(b)

SiN$_x$ antireflective coating
Al$_2$O$_3$ particles
Quartz slide
Ag back-reflector
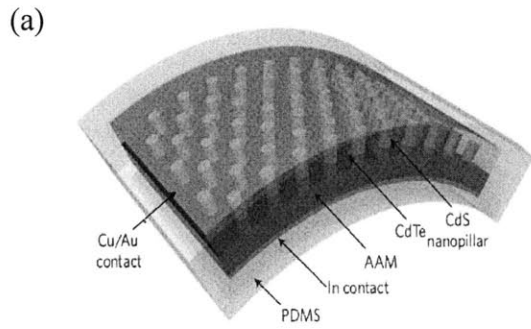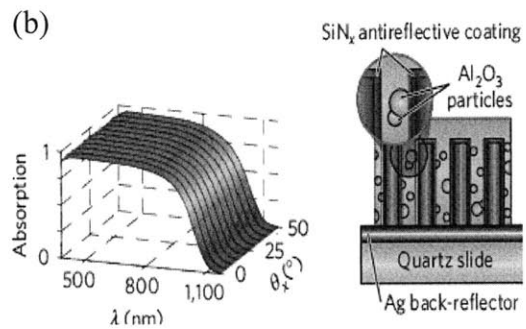
(Kelzenberg, Nature Mat., 2010)

(c)

(MPTV)

(d)
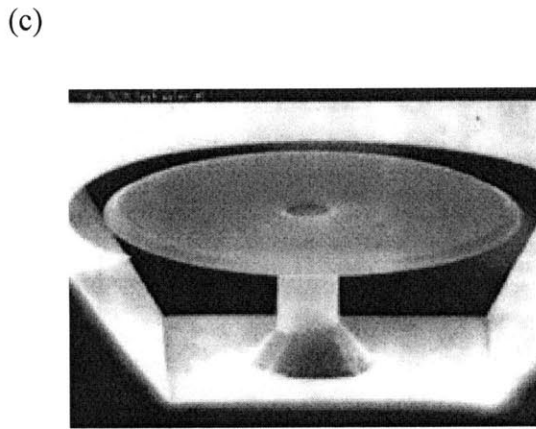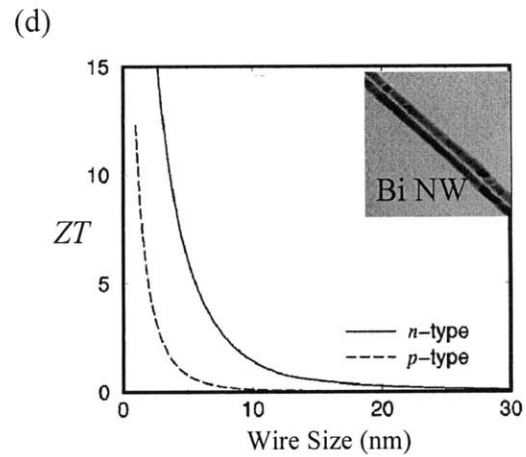
(Sun, Appl. Phys. Lett., 1999)

Figure 1- 1: Examples of nanostructures for energy research

One big challenge at the nanoscale is that the amount of energy transfer is very small. For a nanoparticle with a diameter of 100 nm shown in Fig. 1-2 (a), its absorption under solar radiation (~1000 W/m^2) is ~ 10 pW by simply using its cross sectional area multiplied with the incident power. For a nanowire with a length of 10 μm and a diameter of 100 nm, its absorption under solar radiation is ~ 1 nW. If we consider the heat

19

conduction through the same nanowire and assume its thermal conductivity to be 100 W/m.K (Fig. 1-2 (b)), its thermal conductance is ~ 1 nW/K. For two disks with a diameter of 10 μm in Fig. 1-2 (c), the thermal conductance of radiative heat transfer between them is ~ 10 nW/K when the gap size is 100 nm. Thus, due to the small dimension and the small magnitude of energy transfer, probing nanoscale energy transfer is extremely challenging.

(a) Optical absorption

~ 1,000 W/m^2

(b) Heat conduction
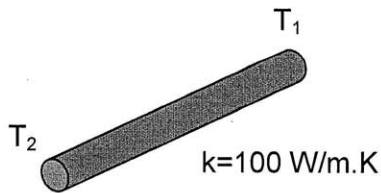
(c) Thermal radiation

T_1

T_2

k=100 W/m.K

Figure 1- 2: Energy transfer in nanostructures

Many existing techniques to measure energy transfer are often too insensitive to detect such small amounts of energy transfer. Shi and his coworkers [12-15] used microfabrication to create a device with two platforms suspended on long and slender silicon nitride beams, and demonstrated that such a device is capable of measuring

thermal conductivities of single nanowires or nanotubes. Each platform has a serpentine metallic heater which is also used as resistance thermometers to measure the temperature of the platform. Fujii *et al.* [16] used electron beam lithography to pattern a thin metallic line heater as a thermal sensor. A manipulation probe built in scanning electron microscope is used to suspend a nanotube between the line heater and a heat sink. Recently, Dames *et al.* [17] developed a hot-wire probe inside a transmission electron microscope to measure the thermal resistance of individual nanowires, nanotubes, and their contacts. One technique presented in this thesis which is able to probe nanoscale energy transfer is based on atomic force microscope (AFM) measurement. An AFM bi-material cantilever is used as a sensor. This bi-material cantilever, for example, has two layers with different thermal expansion coefficients: one is gold, the other is silicon nitride. When the temperature distribution along the cantilever changes, gold and silicon nitride layers will generate different amounts of thermal expansion and correspondingly different strain, causing the cantilever to bend. By using a laser beam to detect the bending of the cantilever in Fig. 1-3, we can measure the heat transfer to the cantilever. Such cantilevers had been demonstrated by previous authors to measure the temperature changes as small as 10^{-5} K, the power as small as 100 pW [18-19]. People have also developed infrared detectors [20, 21] and scanning thermal microscopes [22] based on these cantilevers. In this thesis, I will use these cantilevers as a platform to explore extraordinary energy transfer at the nanoscale including near-field radiation at nanoscale gaps, thermal conduction through a polymer nanofiber, and optical absorption of nanostructures.
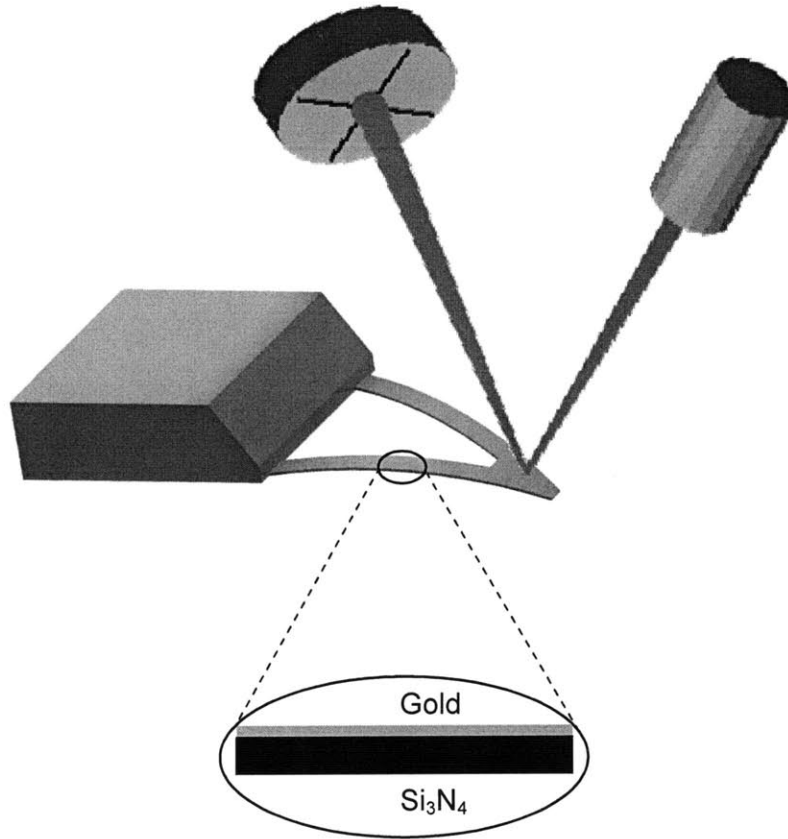
Figure 1- 3: AFM bi-material cantilevers with two layers of gold and silicon nitride

1.2 Outline of the thesis

The purpose of this thesis is to extensively discuss the physics of three nanoscale energy transfer phenomena: near-field radiation, high thermally conductive polymers and optical absorption of nanostructures and develop their corresponding experimental solutions to measure their magnitudes of energy transfer.

Chapter 2 describes the general beam theory that is used to model thermo-mechanical responses of bi-material cantilevers. Based on the beam theory and the thermal analysis of a bi-material cantilever, the effective thermal conductance of the cantilever and the temperature at the tip of the cantilever are determined by measuring the

bending of the cantilever in response to two different thermal inputs: power absorbed at the tip and the ambient temperature.

Chapter 3 discusses the near-field radiation in which the gap size between two bodies is smaller than the photon wavelength. The theoretical framework of near-field radiation is presented based on fluctuational electrodynamics theory. At nanoscale gaps, the near-field radiation is experimentally demonstrated to far exceed the prediction from Planck's blackbody radiation.

Chapter 4 theoretically evaluates the optical properties of a single nanoparticle or nanowire by Mie theory. A new experimental setup is presented to directly measure the spectral absorption of micro/nanostructures in applications to solar photovoltaics.

Chapter 5 develops a new technique to fabricate ultradrawn polyethylene nanofibers. These nanofibers are experimentally demonstrated to have a thermal conductivity as high as ~ 100 W/m.K, which is ~ 3 orders of magnitude enhancement compared to that of bulk polymers.

Chapter 6 summarizes the main contributions of this thesis and identifies the future directions.

1.3 References

[1] Kamat, P. V. Meeting the clean energy demand: Nanostructure architectures for solar energy conversion. *J. Phys. Chem. C* **111**, 2834-2860 (2007).

[2] Baxter, J. *et al*. Nanoscale design to enable the revolution in renewable energy. *Energy Environ. Sci.* **2**, 559–588 (2009).

[3] Chen, G. *Nanocale Energy Transport and Conversion* (Oxford, New York, 2005).

[4] Fan, Z. *et al*. Three-dimensional nanopillar-array photovoltaics on low-cost and

flexible substrates. *Nature Mat.* **8**, 648-653 (2009).

[5] Kelzenberg, M. D. *et al.* Enhanced absorption and carrier collection in Si wire arrays for photovoltaic applications. *Nature Mat.* **9**, 239-244 (2010).

[6] Marti, A. & Luque, A. *Next generation photovoltaics: High efficiency through full spectrum utilization* (Institute of Physics, Bristol, UK, 2003).

[7] DiMatteo, R. *et al.* Micron-gap thermalphotovoltaics (MTPV), *Thermophotovoltaic Generation of Electricity, sixth Conference*, Volume 738, Issue 1, pp. 42-51 (2004).

[8] Hicks, L. D & Dresselhaus, M. S. Effect of quantum-well structures on the thermoelectric figure of merit. *Phys. Rev. B* **47**, 12727 (1993).

[9] Hicks, L. D & Dresselhaus, M. S. Thermoelectric figure of merit of a one-dimensional conductor. *Phys. Rev. B* **47**, 16631 (1993)

[10] Lin, Y. M., Sun, X. & Dresselhaus, M. S. Theoretical investigation of thermoelectric transport properties of cylindrical Bi nanowires. *Phys. Rev. B* **62,** 4610 (1993).

[11] Sun, X., Zhang, Z. & Dresselhaus, M. S. Theoretical modeling of thermoelectricity in Bi nanowires. *Appl. Phys. Lett.* **74**, 4005 (1999).

[12] Kim, P., Shi, L., Majumda, A. & McEuen, P. L. Thermal transport measurements of individual multiwalled nanotubes. *Phys. Rev. Lett.* **87**, 215502 (2000).

[13] Shi, L. *et al.* Measuring thermal and thermoelectric properties of one dimensional nanostructures using a microfabricated device. *J. Heat Transfer* **125**, 881-888 (2003).

[14] Shi, L. *et al.* Thermal conductivities of individual tin dioxide nanobelts. *Appl. Phys. Lett.* **84**, 2638 (2004)

[15] Yu, C., Shi, L., Yao, Z., Li, D. & Majumdar, A. Thermal conductance and thermopower of an individual single-wall carbon nanotube, *Nano Lett.* **5**, 1842-1846 (2005).

[16] Fujii, M. *et al.* Measuring the thermal conductivity of a single carbon nanotube. *Phys. Rev. Lett.* **95**, 065502 (2005).

[17] Dames, C. *et al.* A hot-wire probe for thermal measurements of nanowires and nanotubes inside a transmission electron microscope, *Rev. Sci. Instrum.* **78**, 104903 (2007).

[18] Barnes, J. R., Stephenson, R. J., Welland, M. E., Gerber, C. & Gimzewski, J. K. Photothermal spectroscopy with femtojoule sensitivity using a micromechanical device. *Nature* **372**, 79-81 (1994).

[19] Barnes, J. R. *et al.* A femtojoule calorimeter using micromechanical sensors. *Rev. Sci. Instrum.* **65**, 3793 (1994).

[20] Varesi, J., Lai, J., Perazzo, T., Shi, Z. & Majumda, A. Photothermal measurements at picowatt resolution using uncooled micro-optomechanical sensors *Appl. Phys. Lett.* **71**, 306 (1997).

[21] Datskos, P.G. *et al.* Remote infrared detection using piezoresistive microcantilevers *Appl. Phys. Lett.* **69**, 2986 (1996).

[22] Nakabeppu, O., Chandrachood, M., Wu, Y., Lai, J. and Majumda, A. Scanning thermal imaging microscopy using composite cantilever probes. *Appl. Phys. Lett.* **66**, 694 (1995).

Chapter 2: Bi-material microcantilevers

as thermal sensors

2.1 Introduction

The bi-material microcantilever considered in this thesis consists of two layers which are made from two materials with different thermal expansion coefficients, such as Si_3N_4 and Au, or Si and Al, or Si and a polymer [1-3]. When the temperature of the microcantilever changes, the different amounts of thermal expansion generated by the two layers cause the cantilever to bend. Thus, the microcantilevers can be used as temperature and heat flow sensors [4, 5]. Besides the thermal expansion coefficients of two materials, the sensitivity of the bi-material microcantilever also depends on its dimensions, mechanical properties and thermal properties, such as Young's modulus, thermal conductivities and heat capacities [1, 2]. A typical commercially available bi-material microcantilever is the Si_3N_4 atomic force microscope (AFM) cantilever (200 μm long and 0.6 μm thick) coated with 70 nm gold film.

Bi-material cantilevers were first introduced as a calorimeter to measure the heat generated in chemical reactions [4]. The same device was demonstrated to be sensitive enough to measure a power as small as 100 pW or an energy of 150 fJ in photothermal measurements due to its small size and thermal mass [2, 6]. Bi-material cantilevers were also used as IR detectors [7, 8] or as scanning thermal imaging probes [9]. In this chapter, the thermo-mechanical properties of bi-material microcantilevers are characterized. Section 2.2 introduces the beam theory for modeling bi-material slabs. Based on the beam theory, an experimental technique is developed in Section 2.3 to determine the thermal conductance of the microcantilevers.

2.2 Beam theory

Figure 2-1 shows a microscope image of a silicon nitride cantilever beam used in our study. The cantilever is coated with a 70 nm thick gold film and has a length of 200 μm and a thickness of 600 nm, and two arms with a width of 30 μm. The triangular shaped cantilever is modeled as a rectangular beam for the sake of simplicity. Using beam theory, the deflection of a bi-material strip with different thermal expansion coefficients can be solved from the following differential equation [2, 6]

$$\frac{d^2 Z}{dx^2} = 6(\gamma_2 - \gamma_1)\frac{t_1 + t_2}{t_2^2 K}\left(T(x) - T_0\right), \tag{2-1}$$

where $Z(x)$ is the vertical deflection at a location x, γ is the thermal expansion coefficient, t is the thickness of the layers, $T(x)$ is the temperature distribution along the cantilever, T_0

is the reference temperature at zero deflection, K is a constant defined by the thickness ratio (t_1/t_2) and the Young's modulus of the layers as

$$K = 4 + 6\left(\frac{t_1}{t_2}\right) + 4\left(\frac{t_1}{t_2}\right)^2 + \frac{e_1}{e_2}\left(\frac{t_1}{t_2}\right)^3 + \frac{e_2}{e_1}\left(\frac{t_2}{t_1}\right),$$

where e is Young's modulus. The boundary conditions for the differential equation Eq. (2-1) are $Z(l) = 0$, and $dZ(l)/dx = 0$ since the base of the cantilever is fixed at $x=l$, where l is the length of the cantilever. The subscripts 1 and 2 refer to the two layers: "1" for Au and "2" for Si_3N_4. Obviously, the temperature distribution of $(T(x) - T_0)$ must be determined to solve the deflection $Z(x)$ from Eq. (2-1). Here, the temperature difference in the thickness direction is negligible because the thickness of the cantilever is much smaller than its length.
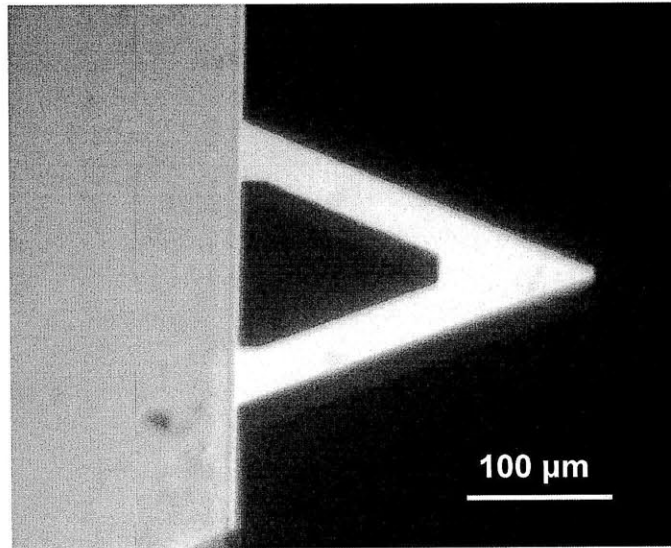
Figure 2- 1: Microscope image of an AFM bi-material cantilever

To determine the temperature distribution along the cantilever, let us consider one example where a laser beam, as a heat source, illuminates at the tip of the cantilever. The laser beam is also used to detect the deflection of the cantilever. During our following

experiments, the area of the laser spot ($\sim 20\ \mu m \times 20\ \mu m$) on the cantilever is usually observed. Two cases will be considered: (1) the assumed case that all the heat from the laser is absorbed at one point and (2) a finite distribution of heat across some length, $l_1 = 20\mu m$ from the tip, as shown in Fig. 2-2. The heat loss from the cantilever due to heat convection and radiation is assumed to be negligible compared to the absorbed heat from the laser.

(a)

Case 1

(b)
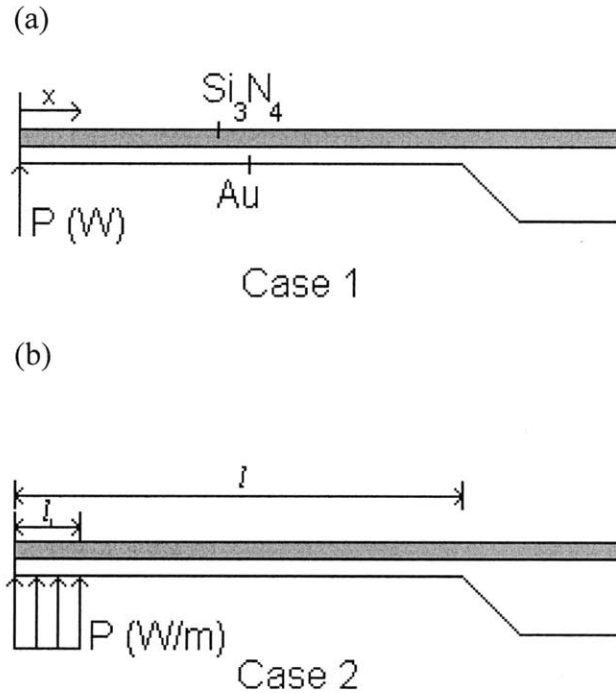
Case 2

Figure 2- 2: (a) Case 1: heat penetrated only at the tip, (b) Case 2: Heat distributed at the tip

For case 1 (Fig. 2-2 (a)), the temperature distribution is linear along the length,

$$(T(x)-T_0)_1 = (l-x)\frac{P}{w(k_1 t_1 + k_2 t_2)},\tag{2-2}$$

where P is the total heat absorbed in the cantilever, l is the length of the cantilever, w is the effective width of the cantilever, and k_i is the thermal conductivity for layer i. For

29

case 2 in Fig. 2-2 (b), the temperature distribution can be described by a piece wise distribution where $T(l) - T_0 = 0$ and continuity is assumed at l_1,

$$(T(x) - T_0)_2 = \begin{cases} \dfrac{P}{w(k_1 t_1 + k_2 t_2)} \left[l - \dfrac{l_1}{2} - \dfrac{x^2}{2l_1} \right] ; 0 \leq x \leq l_1 \\ \dfrac{P}{w(k_1 t_1 + k_2 t_2)} [l - x] \qquad ; l_1 \leq x \leq l \end{cases} \qquad (2\text{-}3)$$

It can be observed that a distinct parabolic region exists near the tip of the cantilever. But overall, this distribution is approximately linear because $l_1 \ll l$.

Given these temperature distributions, integration of Eq. (2-1) will yield a tip displacement $Z(0)$, which can be compared between both cases to test how close they are. For case 1, integration using Eq. (2-2) will yield,

$$Z_1(0) = Cl^3, \qquad (2\text{-}4)$$

Similarly, for case 2, integration using Eq. (2-3) yields,

$$Z_2(0) = 6C \left(-\frac{l_1^3}{24} + \frac{l^3}{6} \right), \qquad (2\text{-}5)$$

where,

$$C = (\gamma_2 - \gamma_1) \frac{t_1 + t_2}{t_2^2 K} \frac{P}{w(k_1 t_1 + k_2 t_2)} .$$

Upon substitution of known values, the tip displacements become $Z_1(0) = 8 \times 10^6 C$ and $Z_1(0) = 7.998 \times 10^6 C$. As observed, the assumed case where all incident heat is incident at the tip only differs by the more realistic case by 0.025 % uncertainty. Hence, based on this analysis, the assumption that all the heat is incident at a point is validated for an approximation.

2.3 Thermal conductance

Although the bi-material cantilevers are often used as temperature or heat flux sensors, the exact temperature at the tip of the cantilever is usually unknown. Directly measuring the temperature is difficult due to the small geometry of the cantilever structure. To find out the temperature of the cantilever, one should obtain the thermal conductance of the cantilever. However, since the thermal properties of the two layers of the cantilever are dependent on their thickness, one cannot rely on theoretical calculation. In this section, one technique is developed to determine the thermal conductance of the cantilever by measuring the bending of the cantilever in response to the variations of the absorbed power at the tip and the ambient temperature [10].

As shown in Fig. 2-3 (a), a semiconductor laser beam is focused on the tip of the cantilever and reflected onto a position sensing detector (PSD). The deflection of the reflected laser beam spot on the PSD is used as a measure of the deflection of the cantilever. A part of the laser power is absorbed by the cantilever and thus creates a temperature rise at the end of the cantilever. The output of the PSD is converted into an X or Y signal corresponding to the position of the laser spot on the PSD and a sum signal proportional to the incident laser power on it.

31

(a)

(b)

(c)
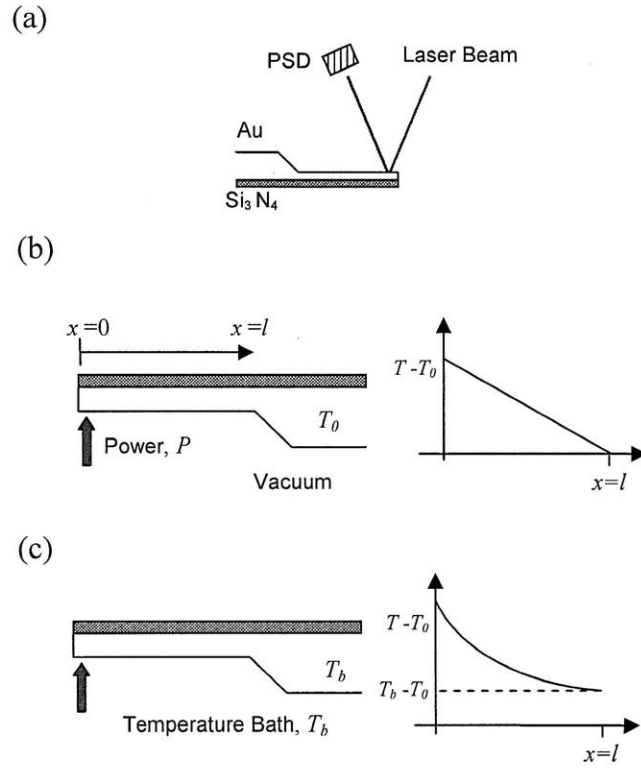
Figure 2- 3: (a) Schematic drawing of the cantilever, laser beam and PSD. (b) Heating is at the end of the cantilever in vacuum. (c) The cantilever is put in a uniform temperature bath with the heating at the end.

First, let us consider the deflection of the cantilever in vacuum when the absorbed power by the cantilever is changed. As shown in Fig. 2-3 (b), the temperature profile in the steady state is

$$T(x) - T_0 = \left(1 - \frac{x}{l}\right)\frac{P}{G},\qquad(2\text{-}6)$$

where G is the effective thermal conductance of the cantilever and P is the absorbed power. Based on the temperature distribution, the slope of the cantilever at the tip, namely the bending angle at the tip because the bending angle is tiny, can be determined using Eq. (2-1) to be $dZ(0)/dx = -3lPH/G$, where the constant H is

$H = (\gamma_2 - \gamma_1)(t_1 + t_2)/t_2^2 K$. As the deflection angle of the cantilever is very small, the slope at the tip is approximately equal to half the deviation angle of the reflected beam as $\theta = dZ(0)/dx = 0.5\Delta d/s$, where Δd is the displacement of the reflected laser spot on the PSD, s is the distance between the cantilever tip and the PSD [11], as shown in Fig. 2-4. Thus, the deviation Δd or the slope $dZ(0)/dx$ is what is actually measured [12, 13]. The sensitivity of the cantilever to the absorbed power can be theoretically expressed as $S_P = \partial(\Delta d)/\partial P = -6slH/G$. Since the thermal conductivity of thin films can be significantly lower than their corresponding bulk value, the sensitivity cannot be calculated directly [14]. However, it is possible to estimate the time constant for thermal relaxation to ensure that the time scale for measurements below is long enough to reach a steady-state deflection. The time constant of the cantilever was predicted to be approximately 1 millisecond by $\tau = \dfrac{l^2}{3}\dfrac{\rho_1 C_1 t_1 + \rho_2 C_2 t_2}{k_1 t_1 + k_2 t_2}$, where ρ is density, and C is specific heat [2].
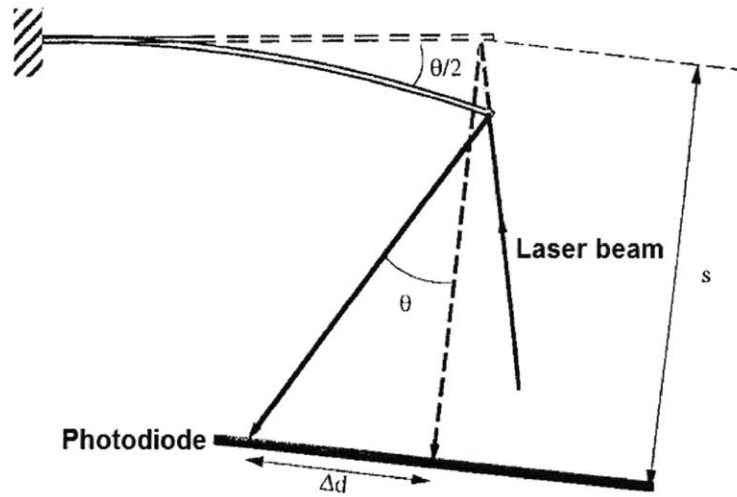
Figure 2- 4: Schematic drawing of bending detection system

33

In order to determine the heat absorbed by the cantilever, the absorptance of the cantilever to incident radiation needs to be known. A power meter (Newport, Model: 818-UV) is used to measure the radiant power in the incident beam (1.66 mW, 650 nm wavelength), the reflected beam (1.25 mW) and the strayed beam (0.20 mW). Thus, the absorbed power by the cantilever is calculated to be 0.21 mW by (1.66 mW-1.25 mW-0.20 mW). The strayed beam is defined as the beam passing through the unblocked area of the cantilever and is measured behind the cantilever perpendicular to the laser incidence direction. We also put the power meter very close to the cantilever at different locations around the cantilever to measure the scattered light from the cantilever. The scattered light intensity was measured to be negligibly small because the cantilever is very thin and flat. During the experiments, it is not the incident light that is measured but the reflected light. The ratio of absorbed to reflected light is 0.168, which is calculated by the ratio of 0.21 mW and 1.25 mW. These numbers can vary depending on the shape of the cantilever and optical arrangement. In Fig. 2-5, the PSD sum signal of the reflected light is plotted as a function of the reflected laser power. The linear relationship between them corresponds to a slope of 0.6436 mW/V. The absorption of the cantilever can be calculated from the PSD sum signal as $0.168 \times 0.6436 \times$ (PSD sum signal). Finally, the PSD deflection signal versus the absorbed power is shown in Fig. 2-6, which gives the measured sensitivity S_P to be -0.0928 V/μW. In our experiment (Fig. 2-7), the heat absorbed from the laser beam heats up the cantilever and causes an initial bending δ_1 on its tip, which is used as the starting point for subsequent changes to the system. For example, when the absorbed power by the cantilever changes, the heat flux conducted by the cantilever changes its temperature and leads to the bending δ_2. What we measured

directly during the experiment, via the photodetector, is the relative change $(\delta_1 - \delta_2)$ of the bending on the cantilever tip. The measurement is intrinsically differential since the initial deflection of the cantilever is already recorded by the photodetector.
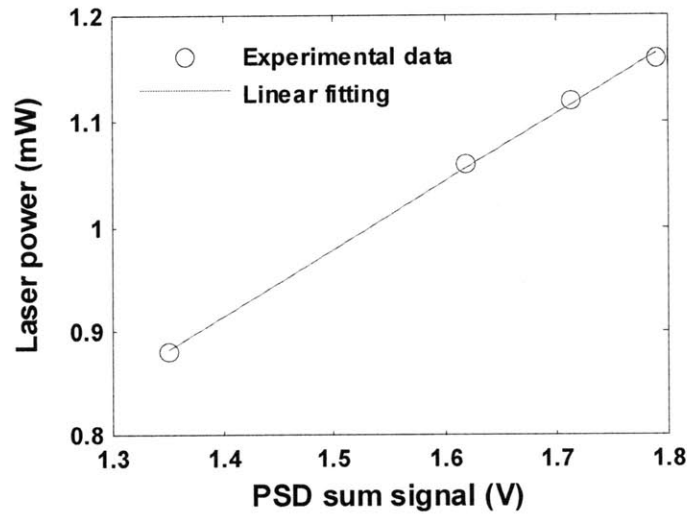
Figure 2- 5: Variation of PSD sum signal with the reflected laser power
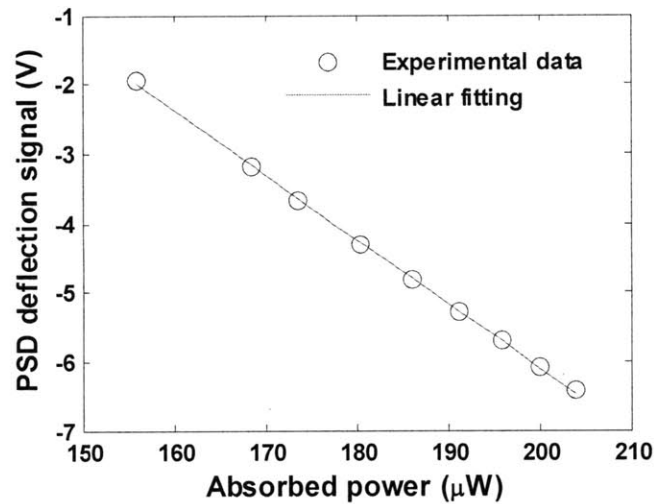
Figure 2- 6: The deflection of the cantilever in vacuum due to the change of heating power
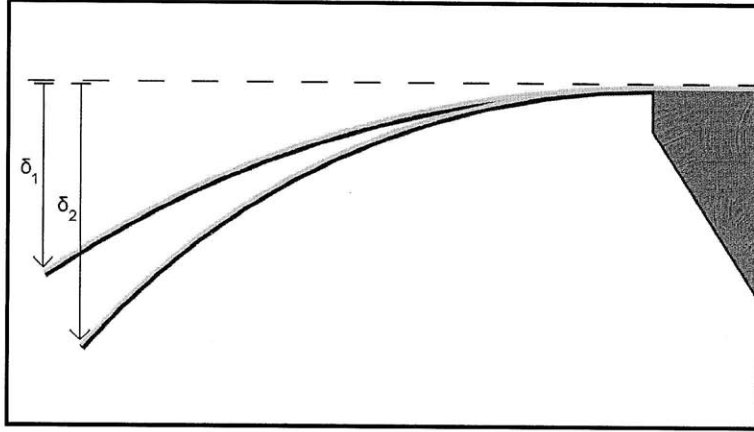
Figure 2- 7: The bending of the cantilever measured in the experiment

The above experiments give the deflection of the laser beam as a function of the input laser power. Next, consider the deflection of the cantilever when the incident power is kept a constant, but the ambient temperature is varied. In Fig. 2-3 (c), the cantilever is in a gaseous environment with a temperature T_b. The support of the cantilever is assumed to have the same temperature T_b. In this case, the cantilever still has a nonuniform temperature distribution due to the incident probing laser beam at the tip. We will show, however, that the existence of such a nonuniform temperature distribution does not matter. Since the composite layer of the cantilever is very thin compared with its length, it is treated as a "fin" with a natural convention heat transfer coefficient h. As shown in Fig. 2-3 (c), the temperature profile in this case is non-linear,

$$T(x) - T_b = \frac{P}{G} \frac{Sinh[\beta(l-x)]}{\beta l Cosh(\beta l)}, \tag{2-7}$$

where β is the fin parameter defined as $\sqrt{2h(w+t_1+t_2)/lG}$ and w is the effective width ($w \approx 60$ μm). The natural convective heat transfer coefficient is predicted to be 500 W/m.K or even larger because of the small geometry of the cantilever [15]. The corresponding slope at the end of the cantilever is given by

36

$$\frac{dZ(0)}{dx} = -6H\left[(T_b - T_0)l + \frac{P}{G}\frac{\left(1 - Sech(\beta l)\right)}{\beta^2 l}\right].$$ (2-8)

Thus, the sensitivity of the cantilever to the ambient temperature variation is obtained

by $S_T = \partial(\Delta d)/\partial T_b = -12sHl$. The conductance G is found to be $G = 0.5S_T/S_P$ [10].

To measure the sensitivity to the ambient temperature, we place the experimental

set-up inside the bell jar of a vacuum chamber and used a hair dryer to increase the air

temperature inside. Once the hair dryer is turned off, the experimental set-up naturally

cools. A K-type thermocouple is attached to the chip that holds the cantilever to measure

the ambient temperature change. After an initial rapid temperature change, the

temperature recorded by the thermocouple shows a slow exponential decay

$(\leq 1.11 \times 10^{-3} K/s)$. The variation of temperature at the base is slow enough compared to

the time constant of the cantilever that the steady state approximation is valid. Figure 2-8

shows that the PSD deflection signal varies with the ambient temperature. Clearly, the

slope of PSD deflection-temperature curve gives the sensitivity of the cantilever to the

ambient temperature S_T, -0.8388V/K.
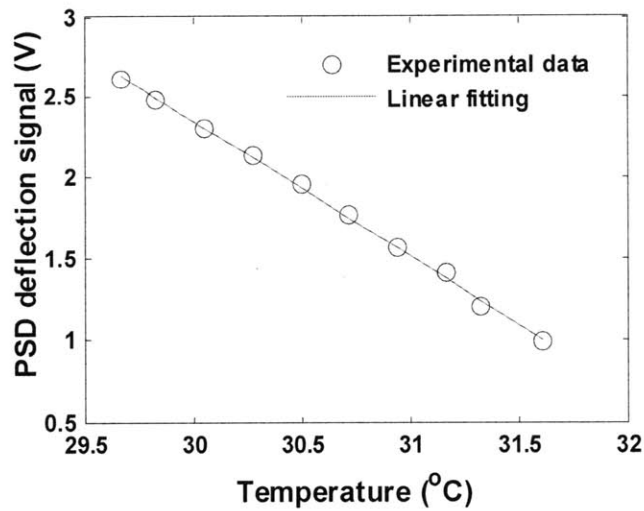
Figure 2- 8: The deflection of the cantilever due to the change of ambient temperature

Based on S_P and S_T, the effective thermal conductance of the cantilever G is determined to be 4.50 μW/K. Using the dimensions of the cantilever and assuming the thermal conductivities of the Si$_3$N$_4$ and Au films to be 2.5 W/m·K and 190 W/m·K, respectively, the theoretical value of thermal conductance is estimated to be around 5.88 μW/K. We point out that the thermal conductivities of Si$_3$N$_4$ [16] and Au [17] films used here are smaller than their bulk values due to grain-boundary and boundary scattering. The agreement between measurement and estimation is reasonable as the exact values of the thermal conductivities for both layers are not known accurately. Once the power absorbed by the cantilever is known, the temperature difference between the tip and the ambient can be obtained from Eq. (2-6). For example, when the PSD sum signal of the reflected light is 1.80V, the absorbed power is given by $0.168 \times 0.6436 \times 1.80 \approx 194.6$ μW, and the temperature difference is 43.1 K.

In summary, we use simple beam theory and the thermal analysis of a bi-material cantilever to demonstrate that the effective thermal conductance of the cantilever can be determined by measuring the sensitivities of the cantilever to variations in the absorbed power and the ambient temperature. This method does not rely on the knowledge of the geometric parameters of the cantilever, such as the length or thickness of either layer, which could vary from cantilever to cantilever. Our experimental results on a Si$_3$N$_4$/Au bi-material cantilever are in agreement with expectations.

2.4 References

[1] Barnes, J. R., Stephenson, R. J., Welland, M. E., Gerber, C. & Gimzewski, J. K. Photothermal spectroscopy with femtojoule sensitivity using a micromechanical device. *Nature* **372**, 79-81 (1994).

[2] Lai, J., Perazzo, T., Shi, Z., & Majumda A. Optimization and performance of high-resolution micro- optomechanical thermal sensors. *Sens. Actuators A* **58**, 113 (1997).

[3] Singamaneni, S. *et al.* Bimaterial microcantilevers as a hybrid sensing platform. *Adv. Mater.* **20**, 653–680 (2008).

[4] Gimzewski, J. K., Gerber, Ch., Meyer, E., & Schlittler, R. R. Observation of a chemical reaction using a micromechanical sensor. *Chem. Phys. Lett.* **217**, 589 (1994).

[5] Majumdar A. Scanning thermal microscopy. *Annu. Rev. Mater. Sci.* **29**, 505-585 (1999).

[6] Barnes, J. R. *et al.* A femtojoule calorimeter using micromechanical sensors. *Rev. Sci. Instrum.* **65**, 3793 (1994).

[7] Varesi, J., Lai, J., Perazzo, T., Shi, Z. & Majumda, A. Photothermal measurements at picowatt resolution using uncooled micro-optomechanical sensors *Appl. Phys. Lett.* **71**, 306 (1997).

[8] Datskos, P.G. *et al.* Remote infrared detection using piezoresistive microcantilevers *Appl. Phys. Lett.* **69**, 2986 (1996).

[9] Nakabeppu, O., Chandrachood, M., Wu, Y., Lai, J. and Majumda, A. Scanning thermal imaging microscopy using composite cantilever probes. *Appl. Phys. Lett.* **66**, 694 (1995).

[10] Shen, S., Narayanaswamy, A., Goh, S. & Chen, G. Thermal conductance of bimaterial microcantilevers. *Appl. Phys. Lett.* **92**, 63509 (2008).

[11] Moulin, A. M., Stephenson, R. J. & Welland, M. E. Micromechanical thermal sensors: Comparison of experimental results and simulations. *J. Vac. Sci. Technol. B* **15**, 590 (1997).

[12] Butt, H. J. & Jaschke, M. Thermal noise in atomic force microscopy. *Nanotechnol.* **6**, 1 (1995).

[13] Lévy, R. & Maaloum, M. Measuring the spring constant of atomic force microscope

cantilevers: thermal fluctuations and other methods. *Nanotechnol.* **13**, 33 (2002).

[14] Chen, G. *Nanoscale Energy Transport and Conversion.* (Oxford, New York, 2005).

[15] Mills, A. F. *Heat Transfer*, 2nd ed. (Prentice Hall, NJ, 1999).

[16] D. Song. *Phonon Heat Conduction in Nano and Micro-Porous Thin Films.* PhD thesis, University of California, Los Angeles, 2003.

[17] Langer, G., Hartmann, J. & Reichling, M. Thermal conductivity of thin metallic films measured by photothermal profile analysis. *Rev. Sci. Instrum.* **68**, 1510 (1996).

Chapter 3: Nanoscale thermal radiation: Breaking down Planck's law

3.1 Introduction

Any object with a temperature larger than zero Kevin emits thermal radiation. Physically, thermal radiation originates from the thermal oscillations of charges inside the body. For a material at thermal equilibrium, charges such as electrons in metals or ions in polar crystals undergo random thermal oscillations and generate fluctuating currents. A body with a temperature T can be regarded as a medium with random currents which radiate an electromagnetic field [1-3]. Hence, the thermal radiation emitted from a body is essentially electromagnetic waves which are generally governed by Maxwell's equations.

When the characteristic length scales of objects are larger than the wavelength of thermal radiation, the radiative heat transfer between two bodies is modeled by classical radiative transfer theory based on Planck's blackbody radiation law [4]. In Fig. 3-1 (a), two semi-infinite bodies with different temperatures are placed in vacuum and separated

by a gap of length *d*. Let us first consider the "far-field" radiation in which the gap distance between two bodies is much larger than the wavelength of thermal radiation, as given by Wien's displacement law [5]. When the incident angle of the electromagnetic wave originated within one body is smaller than the critical angle, the wave is reflected at the interface of the body and transmitted out into vacuum. Then the transmitted wave can propagate and reach the other body, thus transferring energy between them. The radiative heat transfer between these two bodies can be calculated by the classical ray tracing method. In this case, blackbody radiation gives the maximum of heat radiation between them. When the incident angle is larger than the critical angle in Fig. 3-1(b), the phenomenon of total internal reflection occurs where the transmitted wave becomes evanescent. In this case, the electromagnetic field of the transmitted wave decays exponentially across the vacuum gap. Since the gap distance is much larger than the wavelength, the evanescent wave will totally attenuate across the gap and not contribute to the heat transfer between the two bodies. In the "near-field" radiation shown in Fig. 3-1 (c), if two bodies are brought closer such that the gap is smaller than the wavelength, the evanescent wave can tunnel through the gap and enhance the radiative energy transfer between the two bodies. Apparently, Planck's law only deals with propagating waves and fails to predict the contribution from evanescent waves.
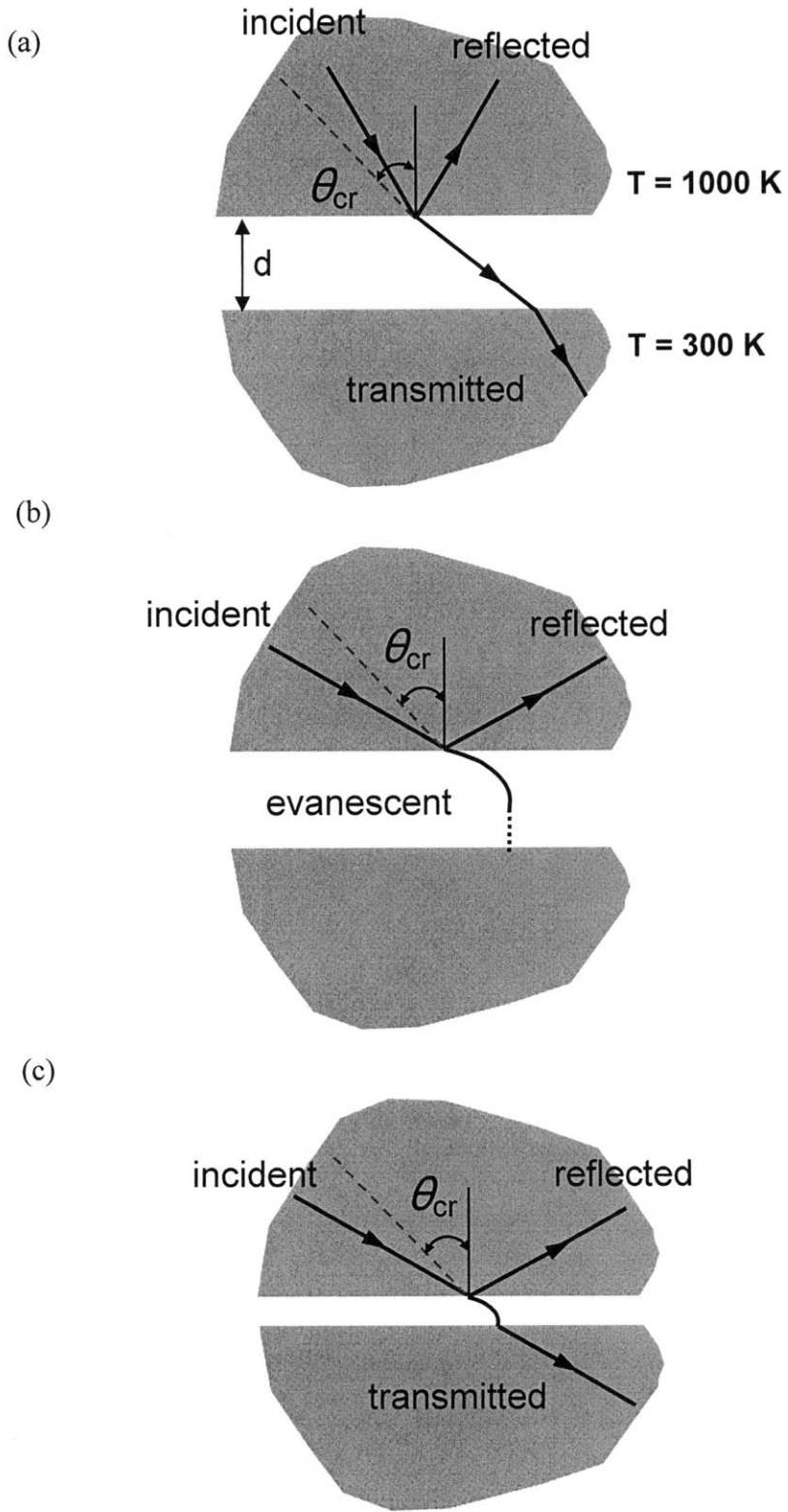
Figure 3- 1: Thermal radiation between two bodies with different gaps. (a) Far-field radiation with propagating waves. (b) Evanescent waves at far-field. (a) Near-field radiation with the contribution from evanescent waves.

In this chapter, near-field thermal radiation is experimentally and theoretically demonstrated to far exceed (~3 orders of magnitude) predictions by Planck's blackbody radiation law. Our work demonstrates conclusively the breakdown of Planck's law at nanoscale gaps. Section 3.2 introduces the theoretical framework about near-field radiation. Section 3.3 describes our experimental techniques to demonstrate the enhancement of near-field radiation.

3.2 Theoretical Framework

Although Planck's blackbody radiation is often considered as the maximum of heat radiation between two surfaces, Planck himself recognized that the law bearing his name is not valid when the characteristic length scales are comparable to or smaller than the wavelength of thermal radiation [4]. Tien and his coworkers first theoretically investigated the enhancement of thermal radiation between two closely spaced bodies [6]. The theoretical foundation of near-field radiation was established by solving Maxwell's equations based on fluctuational electrodynamics theory in which the source of thermal emission is the thermal fluctuation of random currents [1]. The whole theoretical framework has been employed by previous authors to study near-field radiation between the surfaces of metals [7], dielectrics [8-10] and semiconductors [11]. To obtain the electromagnetic field radiated by the random currents, we need to know: (i) the radiative response due to a point source (a random current), which is given by the dyadic Green's

function; (ii) the statistical properties of the random currents, which is given by the fluctuation-dissipation theorem [2].

3.2.1 Dyadic Green's function and fluctuation-dissipation theorem

Let us first recall Maxwell's equations governing the electromagnetic response at a frequency ω [12]:

$$\nabla \times \vec{E}(\vec{r}, \omega) = i\omega \vec{B}(\vec{r}, \omega), \tag{3-1}$$

$$\nabla \times \vec{H}(\vec{r}, \omega) = -i\omega \vec{D}(\vec{r}, \omega) + \vec{J}(\vec{r}, \omega), \tag{3-2}$$

$$\nabla \cdot \vec{D}(\vec{r}, \omega) = \rho, \tag{3-3}$$

$$\nabla \cdot \vec{B}(\vec{r}, \omega) = 0, \tag{3-4}$$

where $\vec{E}$ is the electric field, $\vec{H}$ is the magnetic field, $\vec{D}$ is the electric displacement, $\vec{B}$ is the magnetic flux density, $\vec{J}$ is the current density, and ρ is the charge density. In this following, all the materials are assumed to isotropic and nonmagnetic, and have a linear response, as shown below. One can define the constitutive relations as

$$\vec{D} = \varepsilon_0 \varepsilon \vec{E}, \tag{3-5}$$

$$\vec{B} = \mu_0 \mu \vec{H}, \tag{3-6}$$

where ε is called the dielectric function or relative permittivity, μ is the relative permeability which is equal to 1 for nonmagnetic media. In general, ε is complex and frequency dependent, $\varepsilon(\omega) = \varepsilon'(\omega) + i\varepsilon''(\omega)$, and it is related by the complex refractive index $\tilde{n}(\omega) = n(\omega) + i\kappa(\omega)$ by $\tilde{n} = \sqrt{\varepsilon}$, where n, κ are called the optical constants of materials (κ is also sometimes called the extinction coefficient), and can be

45

experimentally determined by reflectivity measurement. A very useful database of optical constants for solids is available in the handbook edited by Palik [13]. The dielectric function ε can be also derived based on classical theories. For example, the dielectric function of metals can be described by a Drude model [14]

$$\varepsilon(\omega) = \varepsilon_\infty - \frac{\omega_p^2}{\omega^2 + i\Gamma\omega}, \tag{3-7}$$

where ε_∞ is the dielectric function at high frequency, ω_p is the plasma frequency and Γ accounts for the losses or damping. For polar dielectrics, their dielectric function can be modeled by a Lorentz model [15]

$$\varepsilon(\omega) = \varepsilon_\infty \left(1 + \frac{\omega_{LO}^2 - \omega_{TO}^2}{\omega_{TO}^2 - \omega^2 - i\Gamma\omega} \right), \tag{3-8}$$

where ω_{LO} and ω_{TO} are the longitudinal and transverse optical phonon frequencies.

In the Green's function method to solve Maxwell's equations, the electric field $\vec{E}(\vec{r}, \omega)$ and the magnetic field $\vec{H}(\vec{r}, \omega)$ outside a medium containing the sources are given by [16, 17]

$$\vec{E}(\vec{r}, \omega) = i\mu_0 \omega \int_V \overline{\overline{G}}^E (\vec{r}, \vec{r}', \omega) \cdot J(\vec{r}', \omega) d^3\vec{r}', \tag{3-9}$$

$$\vec{H}(\vec{r}, \omega) = \int_V \overline{\overline{G}}^H (\vec{r}, \vec{r}', \omega) \cdot J(\vec{r}', \omega) d^3\vec{r}', \tag{3-10}$$

where $\overline{\overline{G}}^E (\vec{r}, \vec{r}', \omega)$ and $\overline{\overline{G}}^H (\vec{r}, \vec{r}', \omega)$ are the dyadic Green's functions due to the point source at $\vec{r}'$, $J(\vec{r}', \omega)$ represents the fluctuating current source, and μ_0 is the permeability of vacuum. $\overline{\overline{G}}^E (\vec{r}, \vec{r}', \omega)$ and $\overline{\overline{G}}^H (\vec{r}, \vec{r}', \omega)$ are related by

$$\overline{\overline{G}}^H (\vec{r}, \vec{r}', \omega) = \nabla \times \overline{\overline{G}}^E (\vec{r}, \vec{r}', \omega). \tag{3-11}$$

The radiative heat flux can be determined by the Poynting vector $\langle \vec{S}(\vec{r}, \omega) \rangle = \frac{1}{2} \mathrm{Re}(\vec{E} \times \vec{H}^*)$, where the bracket $\langle \ \rangle$ denotes the statistical ensemble average. To calculate the Poynting vector, we need to calculate the component of $\langle \vec{E}_i \vec{H}_j^* \rangle$, where the $*$ denotes the complex conjugate, and i, j refer to the different Cartesian components. In terms of the dyadic Green's functions from Eqs. (3-9) and (3-10), the component $\langle \vec{E}_i \vec{H}_j^* \rangle$ can be written as:

$$\langle \vec{E}_i(\vec{r}, \omega) \vec{H}_j^*(\vec{r}, \omega) \rangle = i\mu_0 \omega \int_V d^3\vec{r}' \int_V d^3\vec{r}'' \left\{ \overline{\overline{G}}_{ik}^E(\vec{r}, \vec{r}', \omega) \overline{\overline{G}}_{jl}^{H*}(\vec{r}, \vec{r}'', \omega) \langle J_k(\vec{r}', \omega) J_l^*(\vec{r}'', \omega) \rangle \right\}. \quad (3\text{-}12)$$

Although the time average of fluctuation currents is zero, its autocorrelation is not zero, and is related to local temperature T and the imaginary part of the dielectric constant ε'' through the fluctuation-dissipation theorem [1, 18, 19]

$$\langle J_k(\vec{r}', \omega) J_l^*(\vec{r}'', \omega) \rangle = \frac{\varepsilon_0 \varepsilon''(\omega) \omega \Theta(\omega, T)}{\pi} \delta_{kl} \delta(\vec{r}' - \vec{r}''), \quad (3\text{-}13)$$

where ε_0 is the permittivity of vacuum and $\Theta(\omega, T) = \hbar \omega \left[\frac{1}{2} + \frac{1}{\exp(\hbar\omega / k_B T) - 1} \right]$. The correlation of fluctuating currents only relates to the imaginary part of the dielectric function which corresponds to the dissipation of energy. δ_{kl} indicates the fact that there is no coupling between two orthogonal fluctuating currents for an isotropic medium, and $\delta(\vec{r}' - \vec{r}'')$ is the Dirac delta function due to a point source. Substituting Eq. (3-13) into Eq. (3-12), we obtain:

$$\langle \vec{E}_i(\vec{r}, \omega) \vec{H}_j^*(\vec{r}, \omega) \rangle = \frac{i\mu_0 \omega^2 \varepsilon_0 \varepsilon''(\omega) \Theta(\omega, T)}{\pi} \int_V d^3\vec{r}' \left\{ \overline{\overline{G}}_{ik}^E(\vec{r}, \vec{r}', \omega) \overline{\overline{G}}_{jk}^{H*T}(\vec{r}, \vec{r}', \omega) \right\}. \quad (3\text{-}14)$$

Based on Eqs. (3-9) and (3-10), we can similarly calculate the density of electromagnetic energy which is the sum of the electrical energy and the magnetic energy

$$\langle U(\vec{r},\omega)\rangle = \frac{\varepsilon_0}{2}\left\langle \left|\vec{E}(\vec{r},\omega)\right|^2\right\rangle + \frac{\mu_0}{2}\left\langle \left|\vec{H}(\vec{r},\omega)\right|^2\right\rangle. \tag{3-15}$$

Using statistical physics, the electromagnetic energy density for a system with an equilibrium temperature T can also be written as the product of the density of states and the mean energy of a state at the temperature T

$$\langle U(\vec{r},\omega)\rangle = \rho(\vec{r},\omega)\frac{\hbar\omega}{\exp(\hbar\omega/k_B T)-1}, \tag{3-16}$$

where $\rho(\vec{r},\omega)$ is defined as the "local" density of states (LDOS) [20]. In far-field, the LDOS is independent of the location and is equal to that in vacuum, whilst it is a function of the location in near-field. In vacuum, the photon energy density is presented by Planck's law as $\langle U(\vec{r},\omega)\rangle = \frac{\omega^2}{\pi^2 c^3}\frac{\hbar\omega}{\exp(\hbar\omega/k_B T)-1}$, where $\frac{\omega^2}{\pi^2 c^3}$ is the photon density of states in vacuum which is a constant [21, 22].

3.2.2 Local density of states and radiative heat flux

Once the dyadic Green's function for a given geometry is known, the radiative heat transfer and the electromagnetic energy density can be numerically calculated. Figure 3-2 shows the calculated local density of states (LDOS) in vacuum at 10 μm and 50 nm above an interface between vacuum and three different materials: silicon dioxide (glass), doped silicon and gold. Here, we only plot the values in the infrared range for the interest of thermal radiation, and these three materials are assumed to be at 300 K. In the near-field shown in Fig. 3-2 (b), the LDOS is much larger than the far-field LDOS (Fig. 3-2

48

(a)) at all wavelengths due to the contribution of evanescent waves. This means that there are more photon modes in the near-field, and thus radiative heat transfer can be enhanced. In particular, the large peaks in the local density of states (Fig. 3-2 (b)) are observed near the surface of silicon dioxide at certain wavelengths, which results from the presence of surface phonon polaritons. And those peaks correspond to the resonance of surface phonon polaritons.
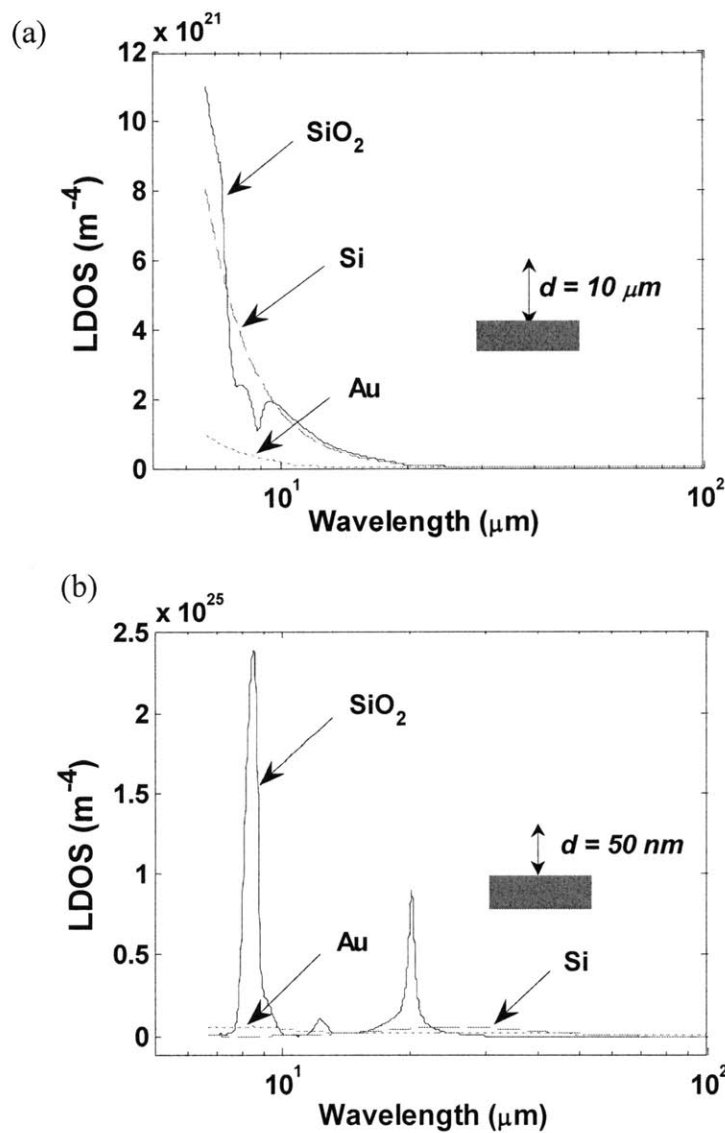
Figure 3- 2: Photon local density of states (LDOS) above an interface between vacuum and different materials at (a) 10 μm and (b) 50 nm

49

The surface phonon-polariton, which originates from the resonant coupling between the electromagnetic field and optical phonons in polar dielectrics such as SiC, SiO_2, and BN, is the infrared counterpart of the surface plasmon-polariton which usually exists on metal surfaces in the visible and ultraviolet range. In both cases, these surface waves share the following properties: they are modes of the system that can be resonantly excited; they are characterized by large energy densities at the interface, which decay rapidly with distance from the surface [23-24]. The dispersion relation (ω vs. k relation) for such surface waves can be obtained from the solution of Maxwell's equations and their corresponding boundary conditions [25],

$$k_{//} = \frac{\omega}{c} \sqrt{\frac{\varepsilon_1 \varepsilon_2}{\varepsilon_1 + \varepsilon_2}}, \qquad (3\text{-}17)$$

where $k_{//}$ is the wavevector along the surface. Equation (3-17) shows that a singularity exists at $\varepsilon_1 = -\varepsilon_2$, at which a large density of states exist, and the surface energy density is extremely high. This is also called as a "resonant effect". In the case that one medium is vacuum, the resonance condition becomes $\varepsilon_1 = -1$. Since surface phonon polaritons exist in the infrared range, they can be thermally excited, and they significantly contribute to thermal radiation. Figure 3-3 shows the real and imaginary parts of the dielectric function of SiC, where the frequency is normalized to the longitudinal optical phonon frequency. The real part of the dielectric function becomes negative between the transverse and longitudinal optical phonon frequencies. Pendry [10] discussed the maximized heat flow for thermal radiation using quantum information theory and derived

a relationship between the real and imaginary parts of dielectric functions of materials to maximize the near-field radiation between flat plates separated by a vacuum gap.
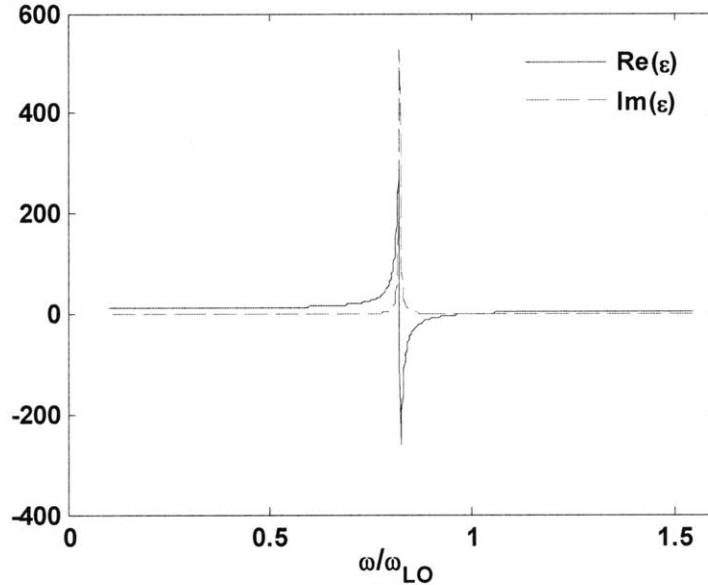
Figure 3- 3: Real and imaginary parts of the dielectric function of SiC solid

In Fig. 3-2 (b), the large peaks in the LDOS are observed near the surface of silicon dioxide at certain wavelengths ($\lambda \approx 8.5 \mu m$ and $\lambda \approx 20.3 \mu m$ for glass) that correspond to surface phonon-polariton resonances. Silicon dioxide SiO_2 (glass) is a polar dielectric material that can support surface phonon polaritons, although compared to crystalline polar materials such as SiC, the resonance is broadened due to stronger damping in amorphous materials. Silicon and gold surfaces, however, do not exhibit any strong resonant excitation peaks in the spectral region under consideration. These surface waves on a SiO_2 surface decay rapidly as we move away from the interface. Hence, despite the high energy density near the interface (Fig. 3-2 (b)), these surface waves do not lead to far-field emission. When another surface is brought close by, the surface waves can tunnel from one side to the other, contributing significantly to heat transfer. Figures 3-4

(a) and (b) show, respectively, the spectral and total radiative heat transfer coefficients defined as the net radiative flux (per unit wavelength interval for spectral heat transfer coefficients) divided by the temperature difference between two parallel plates made of different material combinations (SiO_2-SiO_2, SiO_2-Si, and SiO_2-Au). Resonant peaks similar to those seen in Fig. 3-2 (b) appear for the case of SiO_2 - SiO_2 (Fig. 3-4 (a)), and thus the radiative heat transfer (Fig. 3-4 (b)) can be significantly enhanced. At nanoscale gaps, near-field radiation can be several orders of magnitude larger than the blackbody radiation limit [8].
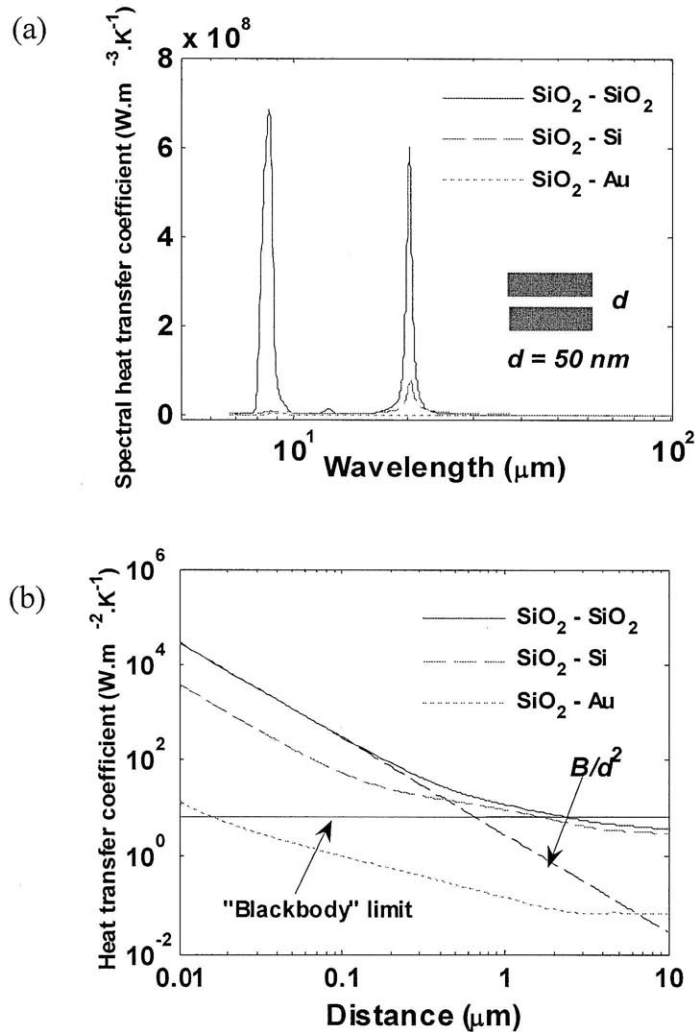
Figure 3- 4: (a) Spectral radiative heat transfer coefficients for two parallel plates separated by a distance $d = 50$ nm at $T = 300$ K; (b) Radiative heat transfer coefficients versus the distance between two parallel plates at an average temperature $T = 300$ K. The plot is on a *log-log* scale. The black solid line is the limit of thermal radiation predicted by the blackbody radiation law, where the heat flux is calculated from the Stefan-Boltzmann law as $\sigma\left(T_1^4 - T_2^4\right)$. The black dashed line is the asymptotic relation at small gaps (B/d^2).

However, in Figs. 3-4 (a) and (b), the radiation enhancement in the cases of $SiO_2 -$ Si and $SiO_2 -$ Au is much smaller than that between SiO_2-SiO_2. To further explain those trends, we asymptotically expand the spectral radiative heat transfer coefficients as [2, 8]

$$h^R(\lambda) \approx \frac{k_B}{\pi^2 d^2}\left(\frac{hc}{\lambda k_B T}\right)^2 \frac{\text{Im}(\varepsilon_1)\text{Im}(\varepsilon_2)}{\left|1+\varepsilon_1\right|^2\left|1+\varepsilon_2\right|^2} \frac{e^{hc/\lambda k_B T}}{\left(e^{hc/\lambda k_B T} - 1\right)^2}, \qquad (3-18)$$

where d is the gap size, T is the temperature, λ is the wavelength, ε_1 and ε_2 are the dielectric constants of two materials, $\text{Im}(\varepsilon)/\left|1+\varepsilon\right|^2$ is the imaginary part of the Fresnel reflection coefficient for waves with large in-plane wavevectors. According to Eq. (3-18) equation, we find that the near-field spectral radiative heat transfer coefficients are inversely proportional to the square of the gap distance, as shown in Fig. 3-4 (b). Near-field radiation is also strongly material-dependent. In Fig. 3-5, the factor $\text{Im}(\varepsilon)/\left|1+\varepsilon\right|^2$ for different materials is plotted as a function of wavelength. The factor $\text{Im}(\varepsilon)/\left|1+\varepsilon\right|^2$ for glass has singularities at the wavelengths ($\lambda \approx 8.5\mu m$ and $\lambda \approx 20.3\mu m$) determined by $\text{Re}(\varepsilon) = -1$, which corresponds to the surface phonon-polariton resonances. Hence, the heat transfer enhancement is stronger for SiO_2 - SiO_2 because the resonances on these two surfaces coincide with each other. Gold, like many metals, can support surface plasmon-polariton, which is the resonant excitation due to the coupling of free electrons with an electromagnetic field. But the plasma frequency of gold is in the near ultraviolet range.

So we cannot observe any resonance of surface plasmon-polariton in the infrared range for gold. For the near-field radiation between two parallel metallic surfaces, Chaputis *et al.* [26] demonstrated that *s*-polarized evanescent waves dominate the heat transfer rather than the *p*-polarized surface-wave dominance in dielectrics. Compared with gold, the plasma frequency of doped silicon can be adjusted to the infrared region with doping. Thus it may support surface plasmon polaritons in the spectral region under consideration, which can thus contribute to near-field radiation. The requirement for the resonance of surface plasmon-polariton between vacuum and a medium is that $Re(\varepsilon) = -1$ and $Im(\varepsilon)$ (absorption) is not too large [27]. For doped silicon, $Re(\varepsilon)$ can be negative in the infrared region, but its surface plasmon-polariton resonance peak shown in Fig. 3-5 is highly damped and very broad because $Im(\varepsilon)$ is large. On the other hand, the resonance of surface phonon-polariton on the glass side is much narrower and almost monochromatic. In the wavelength range where the surface phonon-polariton of glass overlaps with surface plasmon-polariton of silicon, the energy density on the silicon side is small. This is why we cannot observe higher flux using a silicon substrate in Fig. 3-4 (b). In conclusion, the mismatch of materials' properties in $SiO_2 - Si$ or $SiO_2 - Au$ offsets the resonance effects from the SiO_2 surface and results in a smaller enhancement on radiative heat transfer than the case in $SiO_2 - SiO_2$.
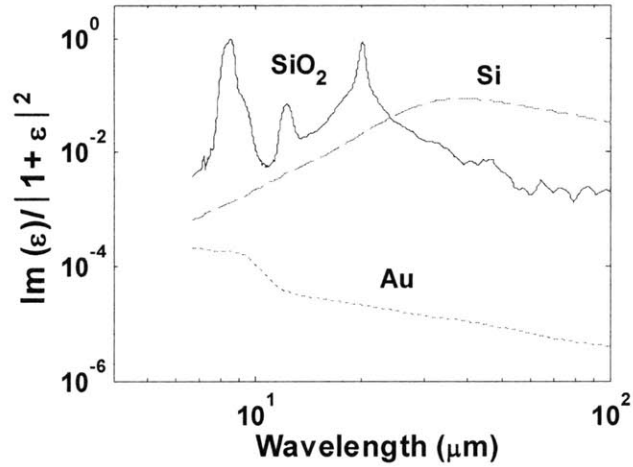
Figure 3- 5: $\mathrm{Im}(\varepsilon)\big/\left|1+\varepsilon\right|^{2}$ versus wavelength for different materials

Besides the resonance effects of surface phonon polaritons, it is well known that non-resonant evanescent waves can contribute to near-field radiation for any material [6, 10]. For an optical medium with a refractive index n and a negligible extinction coefficient κ, the blackbody power spectral density of a medium is n^2 times larger than that of free space because the photon density of states in the medium is increased by a factor n^3, and the speed of light is decreased by a factor of $1/n$. Hence, the upper limit of the near-field radiation between two parallel plates made from the medium is $q = n^2 \sigma (T_1^4 - T_2^4)$, where σ is the Stefan-Boltzmann constant, T is the temperature. Figure 3-6 (a) and (b) shows the heat transfer between two parallel gold plates and the refractive index of gold in the infrared range, respectively. Without the contribution from surface waves, evanescent waves dominate the heat transfer [26]. In the interested wavelength range, the averaged refractive index of glass (plain silica) is ~ 2.0, and the maximum is 3.0. To estimate the contribution from non-resonant evanescent waves, we calculate the near-field radiation between two plates whose optical constants are both

assumed to be $2 + 0.0001i$. Here, we choose the same refractive index with glass, but a much smaller extinction coefficient to eliminate the surface wave effects. In Fig. 3-7, the heat transfer coefficients with resonant surface phonon polaritons can be several orders of magnitude larger than non-resonant ones at small gaps. The non-resonant heat transfer coefficients are also saturated to ($n^2 \times$ heat transfer between two blackbodies) with decreasing gap distances, as predicted.

(a)
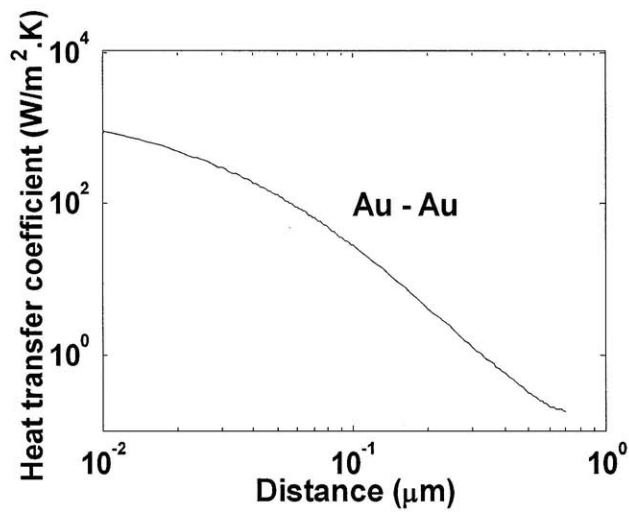
(b)
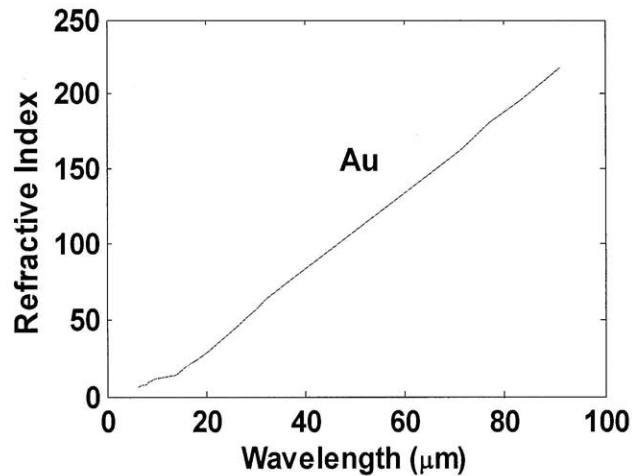
Figure 3- 6: (a) Radiative heat transfer coefficients versus the distance between two parallel gold plates at an average temperature $T = 300$ K. (b) Refractive index n versus the wavelength.
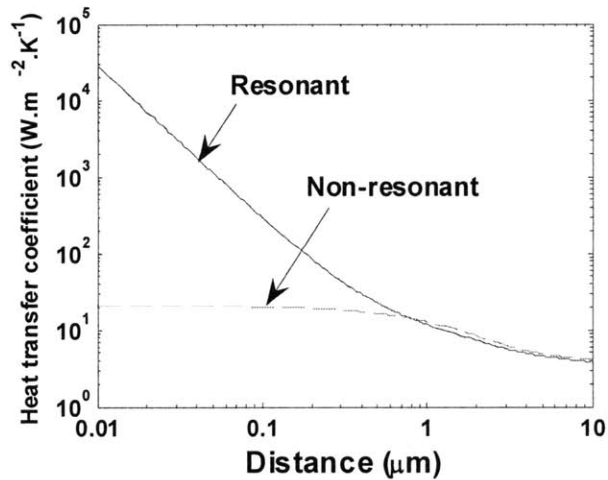
Figure 3- 7: Resonant and non-resonant heat transfer coefficients between two parallel plates for SiO_2 - SiO_2

In summary, the theoretical framework of near-field radiation was well established based on fluctuational electrodynamics theory. In particular, theory has predicted that near-field radiation between polar dielectric materials (SiO_2, SiC, BN, *etc.*), which support resonant surface phonon polaritons, is dominated by the surface phonon-polariton contribution and can be enhanced by several orders of magnitude beyond the Planck's blackbody radiation limit [8]. However, a big challenge is how to experimentally demonstrate such significant enhancement of energy transfer in the near-field.

3.3 Experimental investigation

In comparison with the extensive theoretical studies [7-11], only a few experiments were reported to measure thermal radiation between closely spaced bodies. Domoto *et al.* [28] investigated the radiative transfer between two parallel metallic surfaces with gaps of 50 μm to 1 mm at cryogenic temperature. Hargreas [29] carried out experiments between

two metallic films of chromium at room temperature and showed the enhanced heat transfer around 1 μm. But the near-field radiation heat transfer between two chromium surfaces is still less than 50 % of blackbody radiation. Xu *et al.* [30] measured radiative transfer between a deformed indium surface and a small gold surface but could not confirm any near-field effects. Kittel *et al.* [31] measured radiative heat transfer between a scanning probe microscope tip and a flat substrate. The saturation of heat flux was observed at extremely small distances ($\sim$ 10 nm). They attributed it to spatial dispersion effects and the contribution of the infrared magnetic dipole component. However, the complicated geometry of the tip makes it difficult to interpret the experimental data. Hu *et al.* [32] measured radiative heat transfer between two glass plate and observed radiative heat transfer exceeding predictions of the Planck blackbody radiation law by 35% when the two plates are separated by $\sim$1 μm. More precise measurements are needed to confirm theoretical predictions of near-field enhancement, especially for cases exceeding Planck's blackbody radiation limit.

Experimentally it is very difficult to configure two parallel plates separated by nanoscale gaps and hence the several orders of magnitude increase by surface phonon polaritons in radiation exchange beyond Planck's blackbody radiation law as predicted in Fig. 3-4 (b) have not yet been demonstrated experimentally. Recently, Narayanaswamy [33, 34] developed a sensitive technique of measuring near–field radiative transfer between a microsphere and a substrate using a setup similar to the one in Casmir force measurements and demonstrated that this technique is capable of measuring radiative heat transfer between the sphere and the flat plate when the clearance between them varies from hundreds of nanometers to microns. To follow his technique, I will push to a

much smaller gap (~ 30 nm) and study different materials (dielectric, metal and semiconductor) in this thesis so that the surface phonon polaritons mediated near-field radiation can be clearly demonstrated to break down Planck's law [35].

In Fig. 3-8, a glass (silica) microsphere (Corpuscular Inc.) 50 μm or 100 μm in diameter is attached to the tip of a bi-material (Si_3N_4/Au) AFM cantilever with UV adhesive. Glass spheres are chosen because of their availability over a wide range of diameters with good spherical shapes as well as their ability to support surface phonon polaritons. The output of the position sensing detector (PSD) is converted into an X or Y signal corresponding to the deflection of the AFM cantilever and a sum signal proportional to the incident laser power on it. A part of the laser power is absorbed by the gold film on the cantilever and thus creates a temperature rise on its tip and the sphere. The substrate and the supporting base of the cantilever are passively maintained at the ambient temperature. Based on the beam theory and the thermal analysis of a bi-material AFM cantilever, we calibrate the cantilever and determine its effective thermal conductance between the laser spot and the base (7.91 μW/K) and tip temperature (16.5 K higher than the ambient temperature at the given laser power) by measuring the bending of the cantilever in response to two different thermal inputs: power absorbed at the tip and ambient temperature, as described in Chapter 2.

(a)
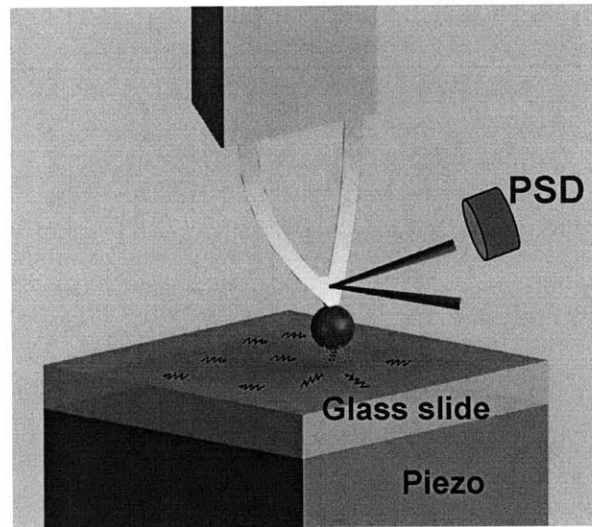
(b)
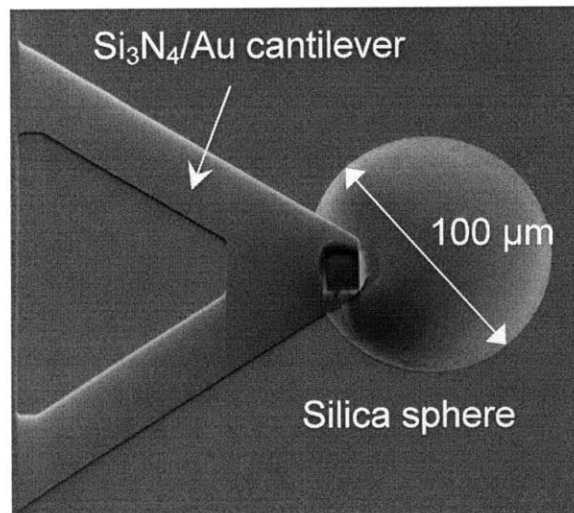
Figure 3- 8: (a) Schematic diagram of experimental setup. The thermal sensor is a silicon nitride AFM cantilever coated with a 70 nm gold film. Application of voltage to the piezoelectric translation stage results in the movement of the substrate towards the sphere. In near-field, surface phonon polaritons can tunnel through the gap and they thus significantly contribute to the radiative heat transfer. The "cooling" effect on the cantilever due to the enhanced near-field radiation leads to the bending of the cantilever. (b) A scanning electron microscope image of a silica (glass) sphere mounted on an AFM cantilever.

The substrate in Fig. 3-8 (a) is rigidly fixed to a piezoelectric motion controller which is able to reduce the gap between the sphere and the substrate below ~ 10 nm. The

cantilever with the microsphere is oriented perpendicularly to the substrate to reduce the bending caused by Casimir and electrostatic forces during the experiment. When the system is pumped down to pressures less than 1×10^{-3} Pa, the heat conduction across the air gap between the sphere and the substrate can be neglected. Most of the laser power absorbed by the cantilever tip is transferred along the cantilever to its supporting base, but a small amount (< 0.5 %) of absorbed heat is radiated to the surrounding (including the substrate) from the cantilever and the sphere. The deflection signal of the cantilever is linearly related to the heat transferred through the cantilever, where the proportionality constant is determined by the properties and dimensions of the cantilever. In the far-field where the gap between the sphere and the substrate is large, surface phonon polaritons are bound to the surfaces and cannot contribute to thermal radiation. Once the gap between the sphere and the substrate is small enough (Fig. 3-8), the enhanced near-field radiation causes the cantilever to bend, responding to the change of temperature distribution in the cantilever due to the different thermal expansion coefficients of the two materials comprising the cantilever. The measured heat flux through the near-field radiation at small gaps is on the order of 100 nW, corresponding to a $\sim 10^{-2}$ K temperature change of the sphere. In the experiment, the far-field radiation loss from the sphere to the rest surrounding (including vacuum chamber, optics assembly, *etc.*) remains constant for a small sphere in a large enclosure [5], where the large enclosure (vacuum chamber) is passively maintained at the ambient temperature. A ~ 0.01 K temperature change of the sphere corresponds to ~ 1 nW change in the far-field radiation loss from the sphere, which is much smaller than the measured near-field radiative flux (~ 100 nW). Hence we conclude that our technique is sensitive to near-field radiation only.

In order to quantitatively measure and correct the force (Casimir and electrostatic forces) effects on our measurement [36, 37], a very weak laser power is used to minimize the temperature difference between the sphere and the substrate (< 1 K) and therefore the near-field radiation between them. Figure 3-9 shows the raw data measured under the laser light with different power for SiO_2-SiO_2. The blue curve is the typical near-field radiation signal measured under a high laser power. During the experiment, we use a piezosystem to change the gap between the sphere and the substrate and hold it constant for several seconds. When the substrate is held at a constant position, the average of deflection signals does not change, and the deflection signal looks flat as a "plateau". The jumps between two such plateaus are due to the change in the position of the substrate. The sharp change of the bending signal indicates the "contact" made between the sphere and the substrate, thereby providing a reference to determine the substrate-sphere separation distance. The green curve is the force signal under a weak laser power. In Fig. 3-9, when the cantilever is carefully oriented in a perpendicular manner to the substrate, the bending caused by the force is almost zero. At the steady state, the temperature of the microsphere is approximated as equal to the tip temperature of the cantilever because the radiation loss from the sphere is much smaller than the heat flow through the cantilever, considering that the conductance of the cantilever is much larger. Finally, the cantilever deflection signal measured by the PSD in Fig. 3-9, which is also linearly proportional to the heat transfer between the sphere and the substrate because the total absorbed laser power by the cantilever is a constant (corresponding to a constant sum signal of the PSD during the experiment), is converted into heat transfer-distance curves. The sensitivity of

the cantilever can be calibrated to be ~ 3 nm/μW. Thus, if the thermal conductance of the cantilever is ~ 5 μW/K, the sensitivity of the cantilever to temperatures is ~ 15 nm/K.
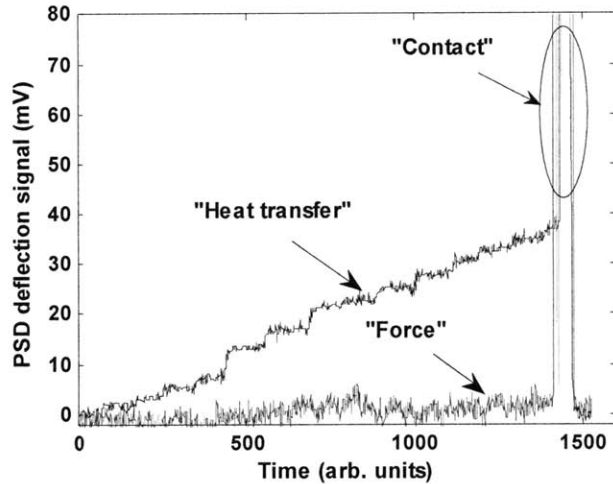
Figure 3- 9: The raw data measured under the laser light with two different power leads. The typical near-field radiation signal (blue curve) is measured under high laser power, where each plateau corresponds to a gap size. The force signal (green curve) is measured under weak laser power. The "contact" between the sphere and the substrate is manifested by the sharp change of the bending signal (PSD deflection signal).
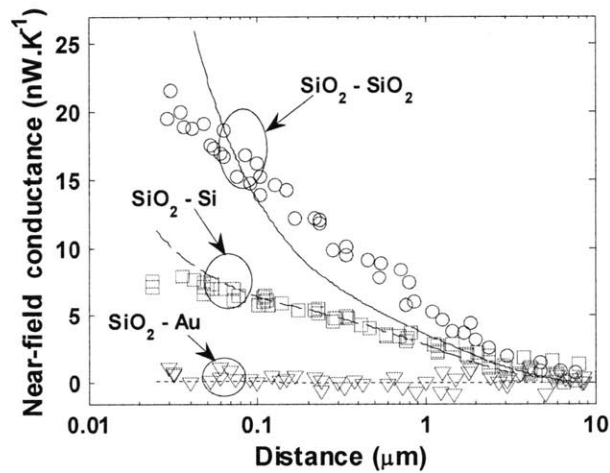
Figure 3- 10: Experimental data from the heat transfer-distance measurement and comparison with the theoretical prediction from the proximity force theorem (black curves). Each conductance data point presented here is the averaged value of ~ 100 measurements with the standard deviation ~ 0.4 nW/K. The experimental error on distance measurements is the resolution of the piezo system (~ 5 nm).

We tested the near-field signals between a glass sphere and each of the substrates considered (glass, doped silicon and gold). The glass plate is a glass microscope slide. The silicon used in our work is n-type, arsenic doped with a carrier concentration of ~ 2.6 $\times 10^{19}$ cm^{-3} measured using the Hall effect technique. The optical constants of the doped silicon are calculated from the models [11]. Higher carrier concentrations usually lead to larger near-field radiation [11]. The metal plate is fabricated by coating a 1 μm thick gold film on a glass slide. The skin depth of gold in the infrared range is estimated to be $\sim$ 15 nm so that a 1 μm thick gold film is sufficient to neglect the effect from the glass slide underneath it. All the substrates are rinsed with isopropanol and are blown dry with nitrogen before testing. In Fig. 3-10, the measured near-field radiative heat conductance, defined as the heat transfer divided by the temperature difference, is plotted as a function of the gap between the sphere and the substrates. Using an AFM we measured the average surface roughness amplitude of three surfaces as 3.3 nm for glass, 3.9 nm for silicon and 3.4 nm for gold. The gap size ranges from $\sim$ 30 nm to 10 μm, considering the surface roughness and the resolution of piezoelectric motion system. The effect of surface phonon polaritons is clearly shown in Fig. 3-10, where we see that near-field radiation is strongly enhanced when the sphere and the substrate are both made of polar dielectric materials.

There is no rigorous theoretical calculation for the near-field radiation between a microsphere and a plate because of computational difficulties [38]. A similar situation occurs in the Casimir force measurement [36, 37]. So, for the sphere-plate geometry, the near-field radiation is estimated by the so-called proximity force theorem which approximates curved surfaces by differential flat areas and using the known solutions for

near-field radiation between parallel surfaces to obtain the sphere-plate near-field radiative conductance [39],

$$G_{near-field}^{sphere-plate}(d) \cong 2\pi R \int_{s=d}^{\infty} h_{near-field}^{plate-plate}(s)ds, \qquad (3\text{-}19)$$

where G is the near-field conductance, h is the heat transfer coefficient and R is the radius of the sphere. We see from Fig. 3-4 (b) that the heat transfer coefficient between two glass surfaces follows an asymptotic relation given by $h \approx B/d^2$, where B is a constant and d is gap distance. At small gaps, equation (3-19) can be further simplified as $G_{near-field}^{sphere-plate}(d) \cong 2\pi Rd(B/d^2)$. The above relation for the near-field conductance between a sphere and a flat surface can also be interpreted as the near-field conductance between two flat surfaces of area $2\pi Rd$ or a disk of radius $\sqrt{2Rd}$. In Fig. 3-10, the calculated conductance-distance (black curves) from Eq. (3-19) is compared with our experimental data. In general, the proximity theory gives a correct order of magnitude in the experimental range and is in reasonable agreement with experimental results. The discrepancies between experiment and proximity theory in Fig. 3-10 for SiO_2-SiO_2 shows that the proximity approximation may be not entirely valid for the near-field radiation between a sphere and a plate because of significant mathematical simplifications. In addition, we used the microscope glass slide for the substrate. Compared to the silica sphere, the glass of the microscope slide is not very pure. But the optical constants used in our calculation are for the pure glass. It may also result in the discrepancies in Fig. 3-10. Due to the large ratio of relevant length scales of the problem (nanometer size gap, tens of microns of sphere radius, and zero radius of curvature of the flat plate), however, no exact numerical solution has been obtained for the sphere-plate problem so far and

detailed mechanisms for the discrepancy between experiments and the proximity theory calculation should be investigated in future studies. The reason for the better agreement between experiment and theory for Si and Au surfaces may be that the near-field radiation for SiO_2-Si or SiO_2-Au increases less rapidly with decreasing gap distances than for that between SiO_2-SiO_2 (Fig. 3-4). Hence, to some extent, the above issues discussed for SiO_2-SiO_2 are mitigated for SiO_2-Si and SiO_2-Au.

In the present sphere-plate experimental system, only a small fraction of the sphere area contributes to the near field radiation transfer between the sphere and the plate. A direct comparison of the conductance of the near-field radiation to that of a blackbody, treating the whole sphere as a blackbody, is hence not appropriate. It was mentioned earlier that the near-field radiation between a sphere and a flat surface can be interpreted as near-field radiation between two parallel planar surfaces of area $2\pi Rd$. When normalized to this equivalent area, the near-field radiative heat transfer coefficient in SiO_2 - SiO_2 is $\sim$ 2230 W/m·K at a $\sim$30 nm gap, compared to $\sim$ 3.8 W/m·K for blackbody radiation (Fig. 3-11). This is the first time, to our knowledge, that the near-field radiation mediated by resonant surface phonon polaritons is observed to exceed the blackbody radiation limit by three orders of magnitude at nanoscale gaps. In the same figure, we also plotted the near-field portion of the radiation heat transfer coefficient between two parallel plates (dashed curves), after subtracting the far field contribution. The magnitude of the sphere-plate heat transfer coefficient compares well with that between two parallel plates. However, the discrepancies between the two are also clear and consistent with our discussions earlier.
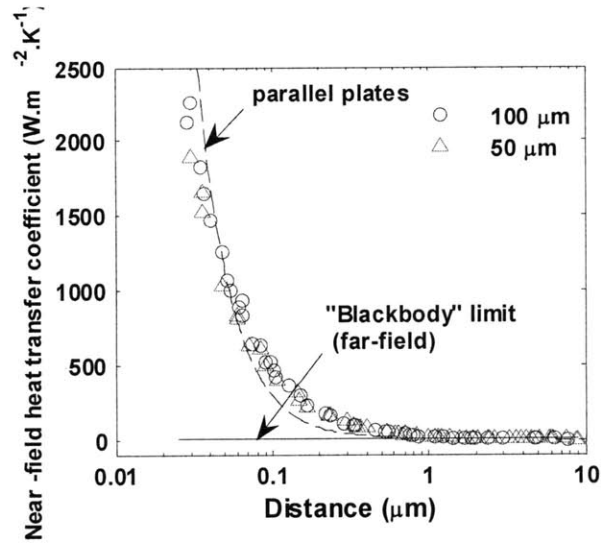
Figure 3- 11: Equivalent sphere-plate near-field heat transfer coefficients normalized to the area $2\pi Rd$ versus the gap distance for a 100 μm (blue circles) and a 50 μm (violet triangles) diameter sphere. The flat line is the limit predicted by Planck's blackbody radiation law. The dashed line is the near-field heat transfer coefficients obtained after subtracting the far-field part taken from Fig. 3-4 (b).

In summary, our experimental demonstration of the extremely high radiative heat transfer between polar dielectric surfaces at nanometer gaps, exceeding by three orders of magnitude the predictions of Planck's blackbody radiation law, may bring new opportunities to fundamental and applied research on radiative cooling and thermophotovoltaic technologies. Many devices rely on working at small gaps. For instance, the clearance between the slider and the disk in a present hard disk drive is only around 10 nm. In such a small gap, near-field radiation becomes important for the heat transfer between the slider and the disk. Thus, near-field radiation is also important for the thermal management of magnetic heads in data storage, heat-assisted data storage, and other microelectromechanical devices.

3.4 References

[1] Rytov, S. M. *Theory of Electric Fluctuations and Thermal Radiation.* (Air Force Cambridge Research Center, Bedford, MA, 1959).

[2] Joulain, K., Mulet, J.P., Marguier, F., Carminati, R., & Greffet, J.J. Surface electromagnetic waves thermally excited: Radiative heat transfer, coherence properties and Casimir forces revisited in the near field. *Surf. Sci. Reports* **57**, 58-112 (2005).

[3] Volokitin, A. I. & Persson, B. N. Near-field radiative heat transfer and noncontact friction. *Rev. Mod. Phys.* **79**, 1291(2007).

[4] Planck, M. *The Theory of Heat Radiation* (Dover Publications, New York,1991)

[5] Siegel, R. & Howell, J. *Thermal Radiation Heat Transfer* (Taylor and Francis, New York, 2002).

[6] Cravolho, E.G., Tien, C.L., & Caren, R.P. Effect of small spacing on radiation transfer between two dielectrics. *J. Heat Transfer* **89**, 351-358 (1967).

[7] Polder, D. and Van Hove, M. Theory of radiative heat transfer between closely spaced bodies. *Phys. Rev. B* **4**, 3303-3314 (1971).

[8] Mulet, J.P., Joulain,K., Carminati, R. & Greffet, J. J. Enhanced radiative transfer at nanometric distance. *Microscale Thermophys. Eng.* **6**, 209-222 (2002).

[9]Mulet, J. P., Joulain,K., Carminati, R. & Greffet, J. J. Nanoscale radiative heat transfer between a small particle and a plane surface. *Appl. Phys. Lett.* **78**, 2931 (2001).

[10] Pendry, J. B. Radiative exchange of heat between nanostructures. *J. Phys. : Condens. Matter* **11**, 6621(1999).

[11] Fu, C.J. & Zhang, Z. M. Nanoscale radiation heat transfer for silicon at different doping levels. *Int. J. Heat Mass Transfer* **49**, 1703 (2006).

[12] Kong, J. A. *Electromagnetic Wave Theory* (Wiley-Interscience, 2000).

[13] Palik, E. *Handbook of Optical Constants of Solids* (Academic Press, 1985).

[14] Ashcroft, N. W. & Mermin, N. D. *Solid State Physics* (Thomson Learning, 1976).

[15] Mills, D. L. & Burstein, E. Polaritons: the electromagnetic modes of media. *Rep. Prog. Phys.* **37**, 817-926 (1974)

[16] Tsang, L., Kong, J. A. & Ding, K. H. *Scattering of Electromagnetic Waves: Theories and Applications* (Wiley Interscience, New York, 2000).

[17] Chew, W. C. *Waves and Fields in Inhomogenous Media* (IEEE Press, Piscataway, NJ, 1995).

[18] Weber, J. Fluctuation dissipation theorem. *Phys. Rev.* **101**, 1620-1626 (1956).

[19] Landau, L. D. & Lifshitz, E. M. *Statistical Physics* (Addison-Wesley, 1969).

[20] Joulain, K., Carminati, R., Mulet, J. P. & Greffet, J. J. Definition and measurement of the local density of electromagnetic states close to an interface. *Phys. Rev. B* **68**, 245405. (2003).

[21] Chen, G. *Nanoscale Energy Transport and Conversion.* (Oxford, New York, 2005).

[22] Modest, M. *Radiative Heat Transfer* (Academic Press, 2003).

[23] Greffet, J. J. *et al.* Coherent emission of light by thermal sources. *Nature* **416**, 61 (2002).

[24] Hillenbrand, R., Taubner, T. & Keilmann, F. Phonon-enhanced light–matter interaction at the nanometre scale. *Nature* **418**, 159 (2002).

[25] eds. Wallis, R. F. & Stegeman, G. I. *Electromagnetic Surface Excitations* (Springer-Verlag, Berlin, 1985).

[26] Chapuis, P.-O., Volz, S., Henkel, C., Joulain, K. & Greffet, J.-J. Effects of spatial dispersion in near-field radiative heat transfer between two parallel metallic surfaces. *Phys. Rev. B* **77**, 035431 (2008).

[27] Raether, H. *Surface Plasmons on Smooth and Rough Surfaces and on Gratings* (Springer-Verlag, Berlin , 1988).

[28] Domoto, G.A., Boehm, R.F. & Tien, C.L., Experimental investigation of radiative transfer between metallic surfaces at cryogenic temperatures. *J. Heat Transfer* **92**, 412-417 (1970).

[29] Hargreaves, C.M. Anomalous radiative transfer between closely-spaced bodies. *Phys. Lett.* **30A**, 491-492 (1969).

[30] Xu, J. B., Lauger, K., Moller, R., Dransfeld, K. & Wilson, I. H. Heat transfer between two metallic surfaces at small distances. *J. Appl. Phys.* **76**, 7209 (1994).

[31] Kittel, A. *et al.* Near-field heat transfer in a scanning thermal microscope. *Phys. Rev. Lett.* **95**, 224301(2005).

[32] Hu, L., Narayanaswamy, A. , Chen, X. Y. & Chen, G. Near-field thermal radiation between two closely spaced glass plates exceeding Planck's blackbody radiation law. *Appl. Phys. Lett.* **92**, 133106 (2008).

[33] Narayanaswamy, A. *Investigation of Nanoscale Thermal Radiation: Theory and Experiments*, PhD Thesis, MIT, Cambridge, 2007.

[34] Narayanaswamy, A., Shen, S. & Chen, G. Near-field radiative heat transfer between a sphere and a substrate. *Phys. Rev. B* **78**, 115303 (2008).

[35] Shen, S., Narayanaswamy, A. & Chen, G. Surface phonon polaritons mediated energy transfer between nanoscale gaps. *Nano Lett.* **9**, 2909-2913 (2009).

[36] Lamoreaux, S. K. Demonstration of the Casimir force in the 0.6 to 6μm range. *Phys. Rev. Lett.* **78**, 5–8 (1997).

[37] Mohideen, U. & Roy, A. A precision measurement of the Casimir force between 0.1 to 0.9 μm. *Phys. Rev. Lett.* **81**, 4549–4552 (1998).

[38] Narayanaswamy, A. & Chen, G. Thermal near-field radiative transfer between two spheres. *Phys. Rev. B* **77**, 075125 (2008).

[39] Blocki, J., Randrup, J., Swiatecki, W. J. & Tsang, C. F. Proximity forces. *Ann. Phys.* **105**, 427 (1977).

Chapter 4 : Optical absorption of micro/nano structures for solar energy conversion

4. 1 Introduction

Solar energy is essentially unlimited and consequently, and it is one of the most promising sources to meet the world's growing energy demand [1]. Solar photovoltaic systems can directly convert photons to electrical power, but the main limitations with present solar cells are their high materials cost and low conversion efficiencies. Nanostructures, such as nanowires [2-4], nanocones [5] and nanoparticles [6-9], have attracted significant attention in solar energy conversion due to their abilities to enhance light trapping and to improve the charge collection efficiency of solar cells, and due to the potential for low cost solar cells by using self-assembled nanostructures. Several groups have demonstrated the broadband reflection suppression due to the strong

scattering of light by nanostructures [2-9]. On the other hand, nanostructured semiconductors can also be fabricated as the active layers of solar cell [2, 3]. Due to their small sizes, the charge collection efficiencies can be significantly increased as well. Clearly, the optical properties of such nanostructured solar cells over the solar spectrum are crucial for their performance. Optimized designs of nanostructures can significantly increase the light trapping of the solar cells, and thus reduce their cost by using less material.

Characterizing of the optical properties of nanostructures such as nanowire and nanocone arrays has often been based on the traditional measurement techniques for bulk materials, for example, using an integrating sphere [5, 9]. However, measuring the optical properties of individual nanostructures and probing the optical coupling between them still remains a great challenge, as discussed in Chapter 1. For individual semiconductor nanostructures such as a single silicon or germanium nanowire, its optical absorption can be evaluated by indirectly measuring their photocurrents generated under illumination. For instance, Cao *et al.* characterized the light absorption properties of single germanium nanowires by measuring their photocurrents [10]. The photocurrent measurement of the nanowires has several drawbacks: (i) it is an indirect and qualitative measurement because not all the light absorbed will generate the current; (ii) it can only measure semiconductors, thus excluding metals and dielectrics.

In this chapter, we will discuss theoretical and experimental methods of determining the optical properties of nanostructures. Section 4.2 introduces Mie theory which can be used to calculate the radiation properties of one single nanoparticle or

nanowire. Section 4.3 presents an experimental setup which is able to directly measure the absorption properties of micro/nano structures.

4. 2 Mie theory

The characteristic dimensions of nanostrutures are often comparable with the photon wavelength. In theory, the optical properties of an individual nanostructure such as a single nanoparticle or nanowire can be calculated by Mie theory which is essentially a set of analytical solutions to Maxwell's equations [15, 16]. This theory is named after German physicist Gustav Mie who published his classical paper in 1908 to study the absorption and scattering properties of aqueous suspensions of gold colloidal particles in the visible range [17]. When electromagnetic waves interact with small particles, the radiative intensity may be changed by the absorption and/or scattering from particles [16]. A typical example is that the scattering of sunlight by the atmosphere (which includes various kinds of air molecules) results in a blue sky. Based on Mie theory, we can calculate the optical absorption of individual nanostructures and determine how large the sensitivity is required for the measurement.

4.2.1 Mathematical formulation

The amount of the incident radiation scattered and absorbed by a particle is usually expressed in terms of the scattering cross section, C_{sca}, and the absorption cross section, C_{abs} [15]. They are defined as

$$C_{sca} = \frac{W_{sca}}{I_i}, \qquad (4\text{-}1)$$

$$C_{abs} = \frac{W_{abs}}{I_i}, \qquad (4\text{-}2)$$

where W_{sca} and W_{abs} are the scattering and absorption energy flux, respectively, and I_i is the incident irradiance. The total amount of absorption and scattering is called extinction which describes the deviation of a photon from its initial trajectory, either by scattering or by absorption. The corresponding extinction cross section C_{ext} is written as

$$C_{ext} = C_{abs} + C_{sca}. \qquad (4\text{-}3)$$

Often, efficiency factors Q, which are the cross sections normalized with the projected surface area, are used instead of cross sections [16]. For example, the scattering and absorption efficiency factors of a sphere are defined, respectively,

$$Q_{sca} = \frac{C_{sca}}{\pi a^2}, \qquad (4\text{-}4)$$

$$Q_{abs} = \frac{C_{abs}}{\pi a^2}, \qquad (4\text{-}5)$$

where a is the radius of the sphere.

In Mie theory, two simple geometries are often considered: small spheres or thin cylinders with an infinite length. To introduce the mathematical formulation of Mie theory, we will present the typical analytical solution from Mie theory to evaluate the scattering and absorption of a small sphere. The mathematical treatment for a thin cylinder with an infinite length is similar. The difference is that a cylindrical coordinate system is used for the small cylinder instead of a spherical coordinate system. The mathematics of Mie theory is rather tedious because the physics of the interaction of an

electromagnetic wave with a sphere is extremely complicated. In this thesis, we will simply quote the analytical expression of the scattered electromagnetic fields $\vec{E}(\vec{r},t)$, $\vec{H}(\vec{r},t)$. More details about the mathematics of Mie theory can be found in the classical book written by Bohren and Huffman [15].

Let us consider a spherical particle with a radius a (labeled "1") placed in some non-absorbing host medium (labeled "2"). In Fig. 4-1, the spherical particle is illuminated by an incident plane wave,

$$E_{inc}(\vec{r}) = \vec{E}_0 \exp(i\vec{k}_2 \cdot \vec{r}) \ , \tag{4-6}$$

where $\vec{k}$ is wave vector. In the spherical coordinate system (r,θ,φ), the scattered electromagnetic fields $\vec{E}(\vec{r},t)$, $\vec{H}(\vec{r},t)$ resulting from Mie theory are represented by the following expression as

$$\vec{E}_{sca}(r,\theta,\varphi) = \sum_{n=1}^{\infty} E_n \left[-b_n \vec{M}_{o1n}^{h2}(r,\theta,\varphi) + i a_n \vec{N}_{e1n}^{h2}(r,\theta,\varphi) \right], \tag{4-7}$$

$$\vec{H}_{sca}(r,\theta,\varphi) = \frac{k_2}{i\omega\mu_2} \sum_{n=1}^{\infty} E_n \left[-b_n \vec{N}_{o1n}^{h2}(r,\theta,\varphi) + i a_n \vec{M}_{e1n}^{h2}(r,\theta,\varphi) \right]. \tag{4-8}$$

where $\vec{H}_{sca}(r,\theta,\varphi) = \dfrac{\nabla \times \vec{E}_{sca}(r,\theta,\varphi)}{i\omega\mu_2}$. The coefficients $E_n (n \geq 1)$ are given by

$$E_n = i^n E_0 \frac{2n+1}{n(n+1)}. \tag{4-9}$$

The two sequences a_n and b_n are usually called the Mie sequences. When the particle and the host medium have the same magnetic permeability, a_n and b_n can be expressed as

$$a_n = \frac{m\psi_n(m\chi)\psi_n'(\chi) - \psi_n(\chi)\psi_n'(m\chi)}{m\psi_n(m\chi)\xi_n'(\chi) - \xi_n(\chi)\psi_n'(m\chi)}, \tag{4-10}$$

$$b_n = \frac{\psi_n(m\chi)\psi_n'(\chi) - m\psi_n(\chi)\psi_n'(m\chi)}{\psi_n(m\chi)\xi_n'(\chi) - m\xi_n(\chi)\psi_n'(m\chi)}. \tag{4-11}$$

The functions ψ_n and ξ_n are known as Riccati-Bessel functions defined by

$$\psi_n(\rho) = \rho j_n(\rho), \tag{4-12}$$

$$\xi_n(\rho) = \rho h_n(\rho), \tag{4-13}$$

where j_n and h_n are the spherical Bessel and Hankel functions. The quantity χ is the size parameter defined by $\chi = k_2 a$, where k is the magnitude of wave vector. The quantity m is the relative refractive index defined by $m = k_1/k_2$. The functions $\vec{M}_{e1n}^{h2}$, $\vec{M}_{o1n}^{h2}$, $\vec{N}_{e1n}^{h2}$, and $\vec{N}_{o1n}^{h2}$ are called vector spherical harmonics with the following expressions as

$$\vec{M}_{e1n}^{h2}(r,\theta,\varphi) = -h_n(k_2 r)\frac{P_n^l(\cos\theta)}{\sin\theta}\sin\varphi\,\hat{e}_\theta - h_n(k_2 r)\frac{dP_n^l(\cos\theta)}{d\theta}\cos\varphi\,\hat{e}_\varphi, \tag{4-14}$$

$$\vec{M}_{o1n}^{h2}(r,\theta,\varphi) = h_n(k_2 r)\frac{P_n^l(\cos\theta)}{\sin\theta}\cos\varphi\,\hat{e}_\theta - h_n(k_2 r)\frac{dP_n^l(\cos\theta)}{d\theta}\sin\varphi\,\hat{e}_\varphi, \tag{4-15}$$

$$\begin{aligned}\vec{N}_{e1n}^{h2}(r,\theta,\varphi) &= n(n+1)\frac{h_n(k_2 r)}{k_2 r}P_n^l(\cos\theta)\cos\varphi\,\hat{e}_r \\ &+ \frac{1}{k_2 r}\frac{d[rh_n(k_2 r)]}{dr}\frac{dP_n^l(\cos\theta)}{d\theta}\cos\varphi\,\hat{e}_\theta \\ &- \frac{1}{k_2 r}\frac{d[rh_n(k_2 r)]}{dr}\frac{P_n^l(\cos\theta)}{\sin\theta}\sin\varphi\,\hat{e}_\varphi\end{aligned} \tag{4-16}$$

$$\begin{aligned}\vec{N}_{o1n}^{h2}(r,\theta,\varphi) &= n(n+1)\frac{h_n(k_2 r)}{k_2 r}P_n^l(\cos\theta)\sin\varphi\,\hat{e}_r \\ &+ \frac{1}{k_2 r}\frac{d[rh_n(k_2 r)]}{dr}\frac{dP_n^l(\cos\theta)}{d\theta}\sin\varphi\,\hat{e}_\theta \\ &+ \frac{1}{k_2 r}\frac{d[rh_n(k_2 r)]}{dr}\frac{P_n^l(\cos\theta)}{\sin\theta}\cos\varphi\,\hat{e}_\varphi\end{aligned} \tag{4-17}$$

where P_n^l are the associated Legendre functions, and $(\hat{e}_r, \hat{e}_\theta, \hat{e}_\varphi)$ are the local right-hand orthogonal basis related to the spherical coordinates (r, θ, φ).
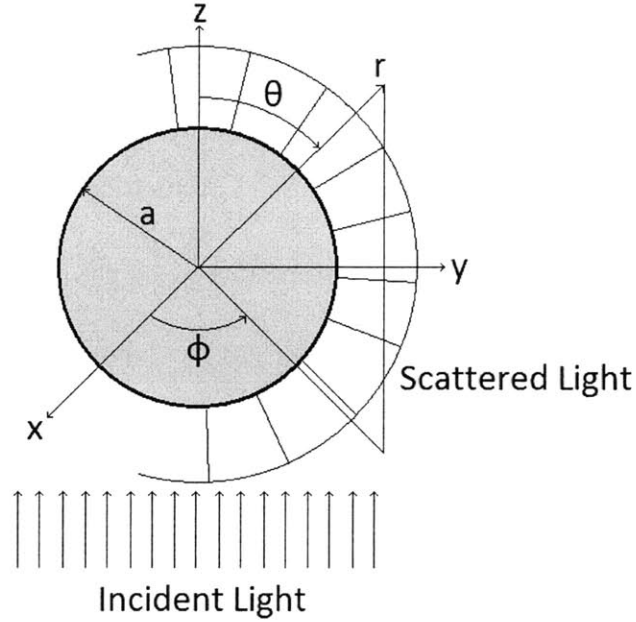
Figure 4- 1: Spherical coordinate system centered on a sphere with a radius a

From Eq. (4-7) and (4-8), the scattering energy flux can be calculated by the Poynting vector. The scattering cross section and the scattering efficiency factor of the particle can be written as

$$C_{sca} = \frac{2\pi}{k_2^2} \sum_{n=1}^{\infty} (2n+1)(|a_n|^2 + |b_n|^2),$$ (4-18)

$$Q_{sca} = \frac{2}{\chi^2} \sum_{n=1}^{\infty} (2n+1)(|a_n|^2 + |b_n|^2).$$ (4-19)

Similarly, the extinction cross section and the extinction efficiency factor of the particle are

$$C_{ext} = \frac{2\pi}{k_2^2} \sum_{n=1}^{\infty} (2n+1) \operatorname{Re}(a_n + b_n),$$ (4-20)

$$Q_{ext} = \frac{2}{\chi^2} \sum_{n=1}^{\infty} (2n+1) \operatorname{Re}(a_n + b_n) . \qquad (4\text{-}21)$$

Once all Mie sequences a_n and b_n are determined, the cross sections or efficiency factors of absorption and scattering can be calculated.

Two limiting cases of Mie theory are often discussed in the literature. When the particle size is large ($\chi \gg 1$ and $|m|\chi \gg 1$), the geometrical optics (ray tracing method) can be employed to calculate the optical properties of the particle [16]. If the particle size is much smaller than the photon wavelength ($\chi \ll 1$ and $|m|\chi \ll 1$), Mie theory reduces to the well known Rayleigh theory. Rayleigh theory is named after Lord Rayleigh who first discussed the absorption and the scattering by single particles during the later part of the nineteenth century [18]. In this case, the interaction of a small particle with electromagnetic waves can be solved using a simple quasi-static approximation. The phase of the oscillating electromagnetic field is practically treated as constant over the particle volume because its size is much smaller than the wavelength of the electromagnetic wave [19]. Thus, one can calculate the spatial field distribution by assuming that the particle is in an electrostatic field. Based on Rayleigh theory, the cross sections for absorption and scattering can be calculated to be

$$C_{abs} = 4\pi k_2 a^3 \operatorname{Im}\left(\frac{\varepsilon_1 - \varepsilon_2}{\varepsilon_1 + 2\varepsilon_2} \right), \qquad (4\text{-}22)$$

$$C_{sca} = \frac{8\pi}{3} k_2^4 a^6 \left| \frac{\varepsilon_1 - \varepsilon_2}{\varepsilon_1 + 2\varepsilon_2} \right|^2 . \qquad (4\text{-}23)$$

From Eqs. (4-22) and (4-23), for small particles with $a \ll \lambda$, absorption in which its cross section scales with a^3 dominates over scattering in which its cross section scales with a^6.

4.2.2 Numerical results

Based on Mie theory, we can calculate the optical properties of a single nanoparticle or nanowire. In the following, we conducted the numerical calculation using the computer codes in the Appendixes of the book written by Bohren and Huffman [15]. In Fig. 4-2, we calculated the spectral absorption and scattering efficiency factors of a silver nanoparticle as a function of its radius. For a small particle ($a < 0.02 \mu m$), the absorption is dominant over the scattering (Fig. 4-2 (a)), whilst for larger particles, the scattering is much larger than the absorption (Fig. 4-2 (b)). This is consistent with the prediction by Rayleigh theory. In particular, large peaks in the absorption and scattering efficiency factors are observed in Fig. 4-2 at the wavelength of light around 300 nm which corresponds to the surface plasmon resonance of sliver particles. In Fig. 4-2 (b), the resonance peaks show a "red" shift due to retardation effects as the size of the nanoparticle increases [20].

(a)

Absorption Efficiency Factor, Qabs

(b)

Scattering Efficiency Factor, Qsca
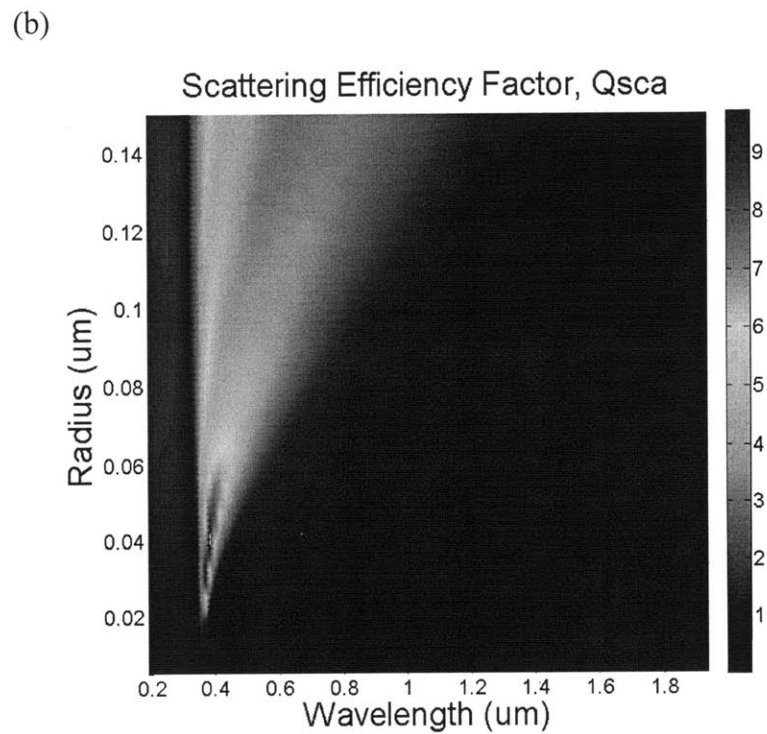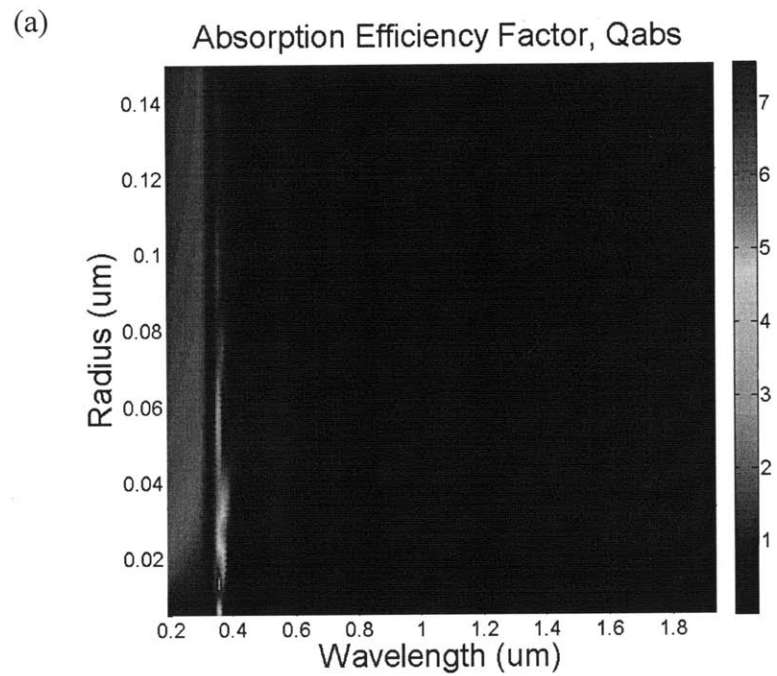
Figure 4- 2: (a) Spectral absorption efficiency factors as a function of the particle size; (b) Spectral scattering efficiency factors as a function of the particle size.

In Fig. 4-3, we calculate the absorption of a silicon micro/nanowire with a length of 50 μm as a function of its radius at normal incidence. Since the length of the micro/nanowire is much larger than its radius in Fig. 4-3, we simply assume that the micro/nanowire is infinitely long. Figure 4-3 (a) shows the calculated absorption efficiency factor of the micro/nanowire. At certain wavelengths of light (for example, 700 nm in wavelength), oscillations in the absorption efficiency factors are observed when the radius of the wire changes. This is because under certain radii, more light corresponding to higher order modes can be coupled. When we fix the radius of the wire, the oscillations of the absorption efficiency factors also occurs in the wavelength range from 600 nm to 800 nm. This results from the interference effects. If the incident power density is assumed to be 100 W/m^2, the absorbed power by the micro/nanowire is plotted in Fig. 4-3 (b). The incidence power of 100 W/m^2 is chosen to correspond to the power density in our experiment, as shown in the next section. We can see from Fig. 4-3 (b), in order to measure the absorption of a single nanowire, our technique is required to measure a power as small as 1 nW (red dashed line). As discussed in previous chapters, an AFM bi-material cantilever is able to measure the power as small as 100 pW. This motivated us to build one setup based on AFM bi-material cantilevers to measure the absorption of nanowires.

(a)

Absorption Efficiency Factor, Q_{abs}
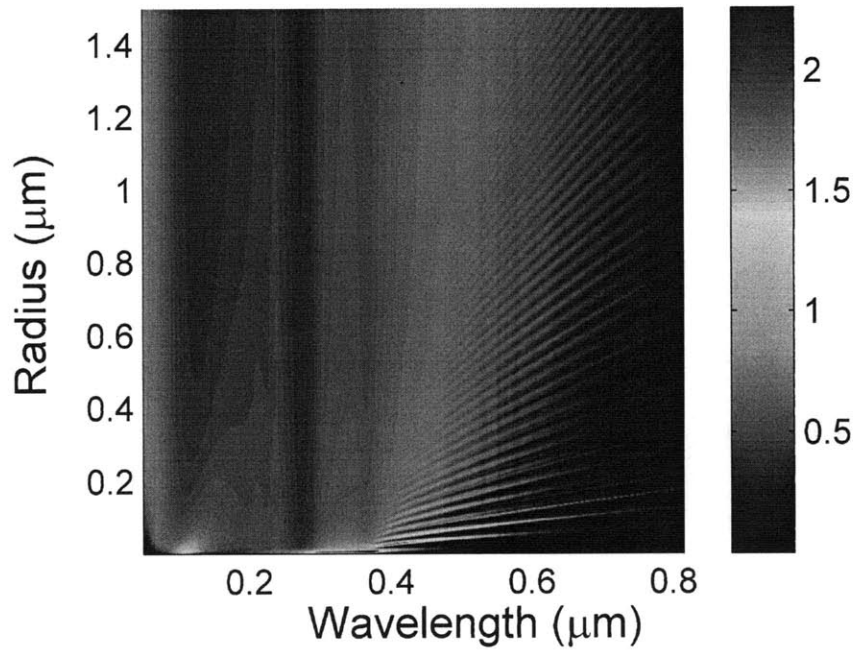
(b)

Absorbed Power (nW)
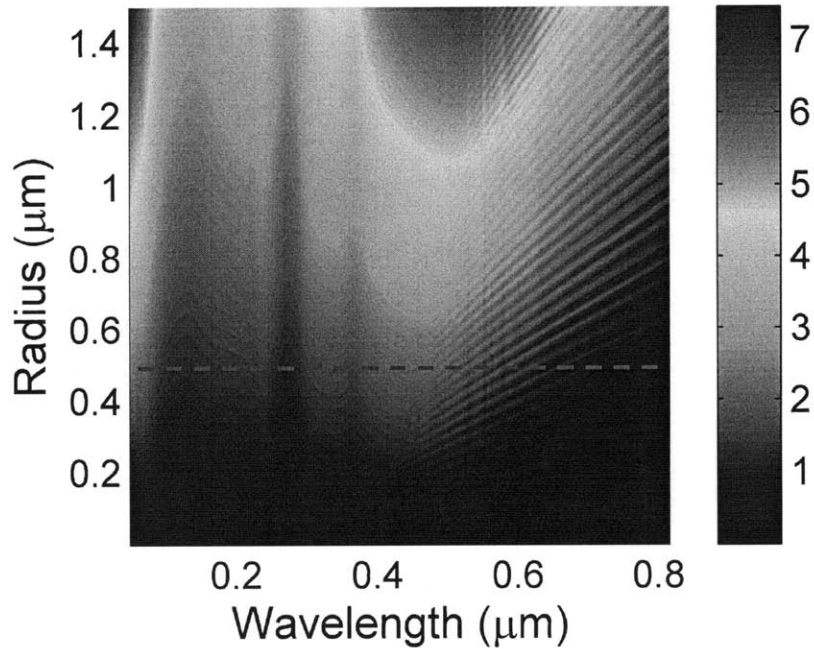
Figure 4- 3: (a) Spectral absorption efficiency factors as a function of the radius of the wire; (b) Spectral absorbed power as a function of the radius of the wire. The red dashed line is marked at the radius 500 nm.

4.3 Experimental investigation

The experimental setup for the optical absorption measurement is illustrated in Fig. 4-4 [21]. A monochromatic light source is focused by an optical lens group and coupled to an optical multimode fiber (200 μm core diameter). The light from the end of the optical fiber illuminates a sample at normal incidence, which is attached to a bi-material AFM cantilever. A motorized moving stage with a resolution 100 nm is used to control the gap between the optical fiber and the sample around 50 μm. At such a small gap, the divergence of the light from the optical fiber end to the sample is negligible; thus the incident field is assumed to be collimated. The multiple reflections between the sample and the optical fiber are also neglected due to the very small reflectivity ($\sim$ 0.04) of the silica optical fiber [22]. The light source is mechanically chopped at $\sim$ 650 Hz so that the cantilever can have a sufficiently fast response to follow the optical modulation generated by the chopper. On the other hand, the modulation frequency of $\sim$ 650 Hz is chosen because below 500 Hz, the noise is dominated by the $1/f$-type behavior arising from the electronics and the optics [23]. The light absorbed by the cantilever or the sample attached on it increases the temperature of the cantilever and thus causes it to bend. On the bottom left is the optical assembly used to measure the deflection of the cantilever using a laser focused onto the tip of the cantilever and reflected onto a position sensing detector. To eliminate the influence from background light and to improve the sensitivity

of our measurement, a lock-in amplifier with the chopper signal as a reference is used. Since the cantilever directly measures the heat generated by the absorption of the sample, the present experimental setup is able to directly and quantitatively characterize the optical properties of the sample compared to the previous indirect photocurrent measurements.
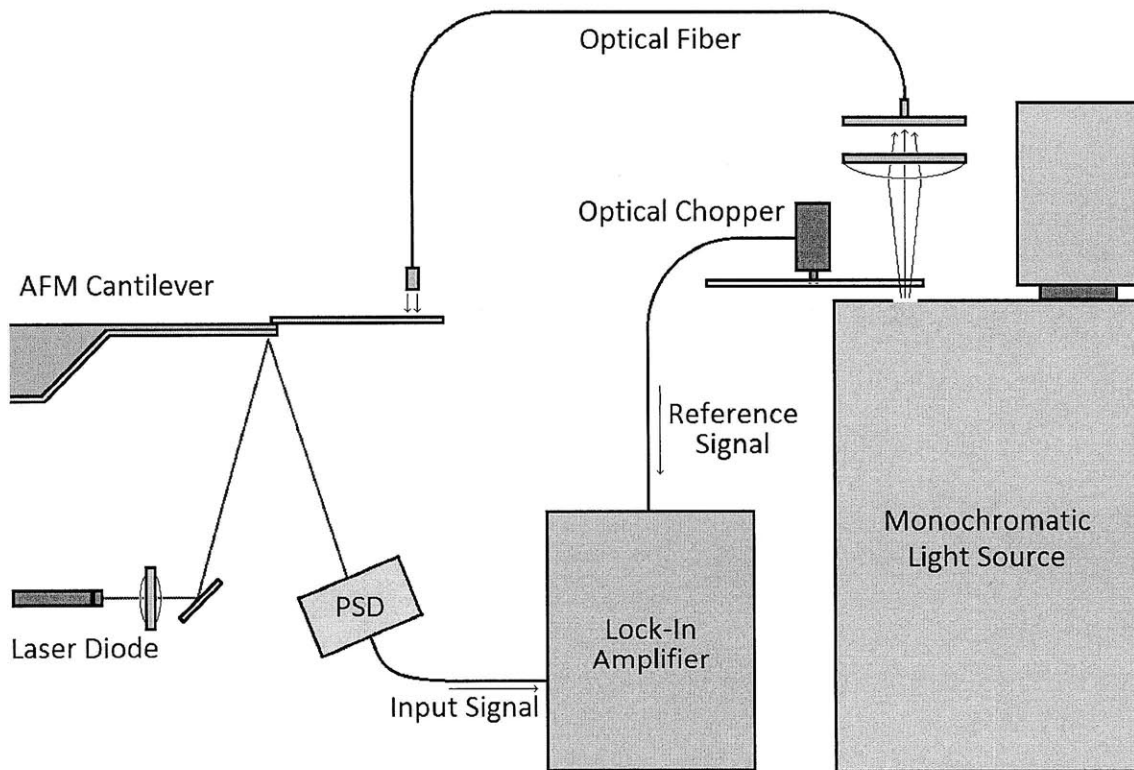
Figure 4- 4: Schematic diagram of experimental setup to measure the optical absorption of micro/nanostructures

To measure the absorptance of a sample, the power spectrum from the light source needs to be measured and calibrated. The power calibration uses a very similar setup, where the AFM cantilever and optics assembly is replaced by a power meter. Figure 4-5 shows the measured spectral response of the source by collecting the light from the end

of the optical fiber. The lowest power measured in the spectrum shown in Fig. 4-5 is ~ 4 μW which corresponds to a power density ~ 100W/m^2. In the following experiments, we first measure the absorptance of the gold layer on a silicon nitride AFM cantilever. The entire cantilever (200 μm in length) is illuminated by the optical fiber (200 μm in diameter). The thickness of the gold layer on the cantilever is ~ 70 nm, which is optically thick for the wavelength range considered. Thus, it is the bulk properties of gold that are measured in the present experiment. The measured absorptance of the gold layer is plotted in Fig. 4-6 (a) and compared with the calculation using Fresnel formulas at normal incidence based on the optical constants of bulk gold in the literature [22].The absorptance of aluminum was also measured, as shown in Fig. 4-6 (b). Overall, our experimental results for these two metals agree well with the calculation based on their bulk properties. The discrepancies between experiment and calculation in Fig. 4-6 may be due to the fabrication process of the samples, for example, sputtering deposition.
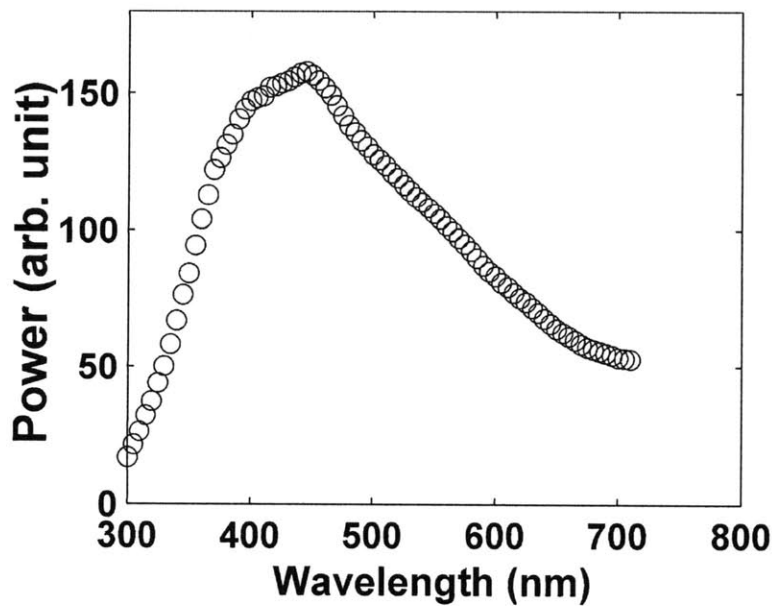
Figure 4- 5: Spectral response of the light source at the end of the optical fiber
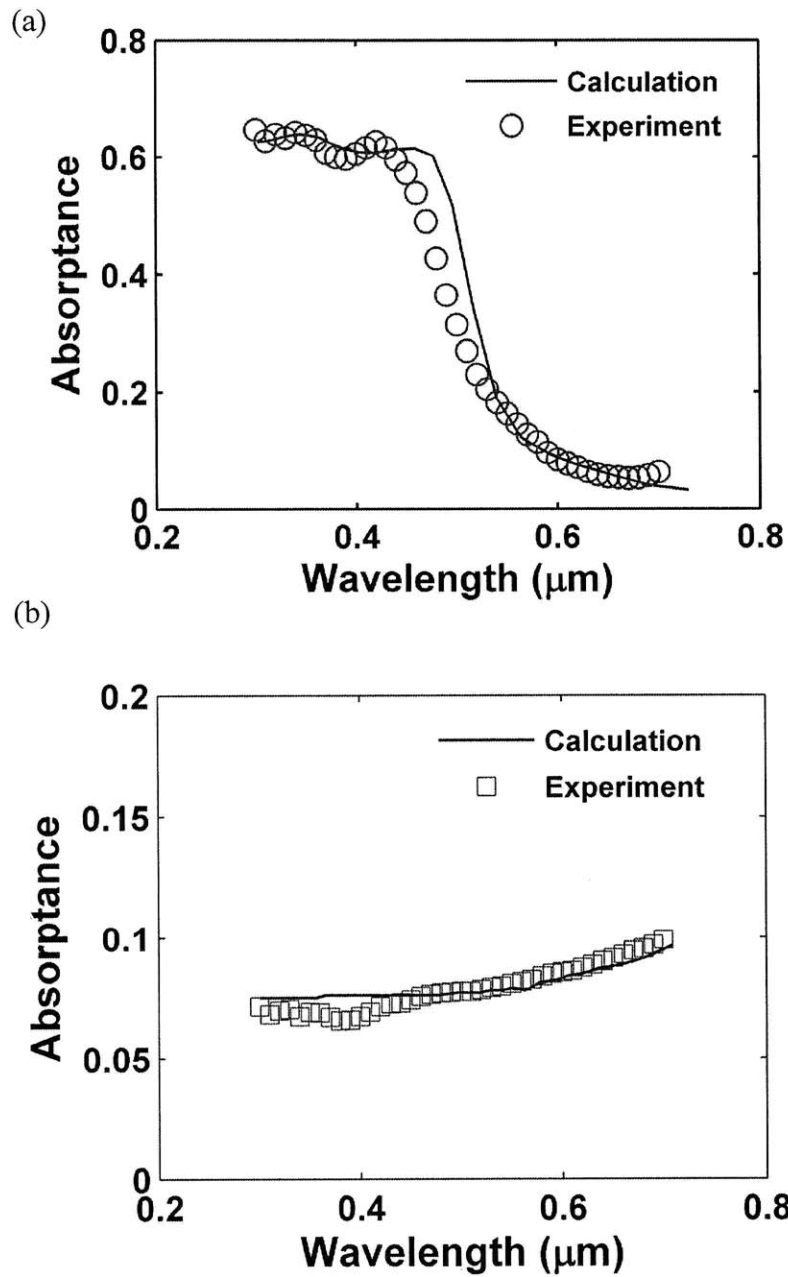
Figure 4- 6: Spectral absorptance of metallic films. (a) Gold; (b) Aluminum. The absorptance is calculated using Fresnel formulas for a semi-infinite body at normal incidence.

The present experimental setup is also able to measure absorption (or absorptance) of a sample attached to the bi-material microcantilever. In Fig. 4-7 (a), a silicon thin film with a thickness of ~ 2 μm is attached to the cantilever with UV adhesive. The same procedure is used to measure the asborptance of the silicon thin film except that the light from the optical fiber illuminates the sample instead of the entire cantilever. The measured absorptance of the silicon thin film is shown in Fig. 4-7 (b) and compared with the calculation using Fresnel formulas where the silicon thin film is sandwiched between two semi-infinite air layers. The experimental data in Fig. 4-7 (b) are in a reasonable agreement with the calculation. From the calculation in Fig. 4-7 (b), we observe the oscillations of absorptance at larger wavelengths because of interference effects. But the resolution of our current monochromator is insufficient to catch those sharp dips and peaks in the oscillations. Indeed, what we measured in the experiment is more like the average of the oscillations.

(a)

100 µm

(b)
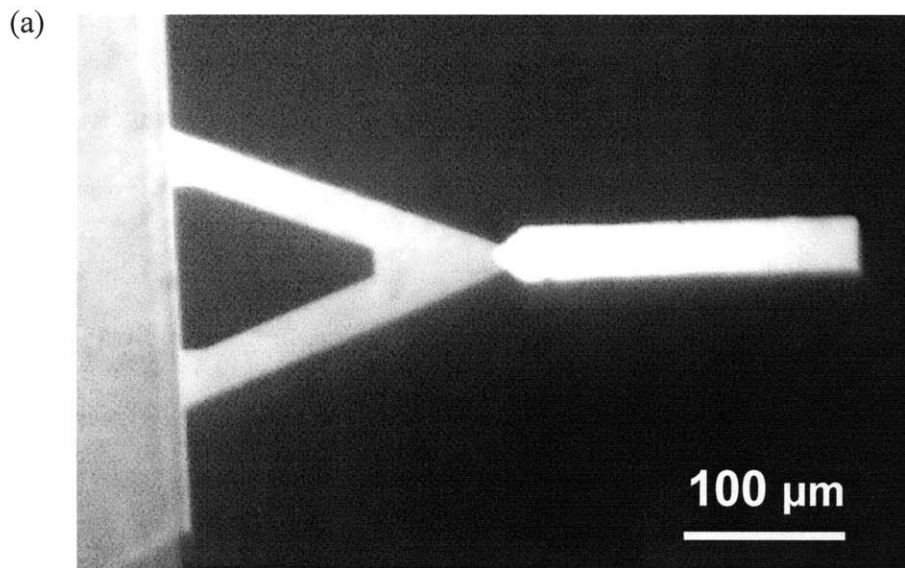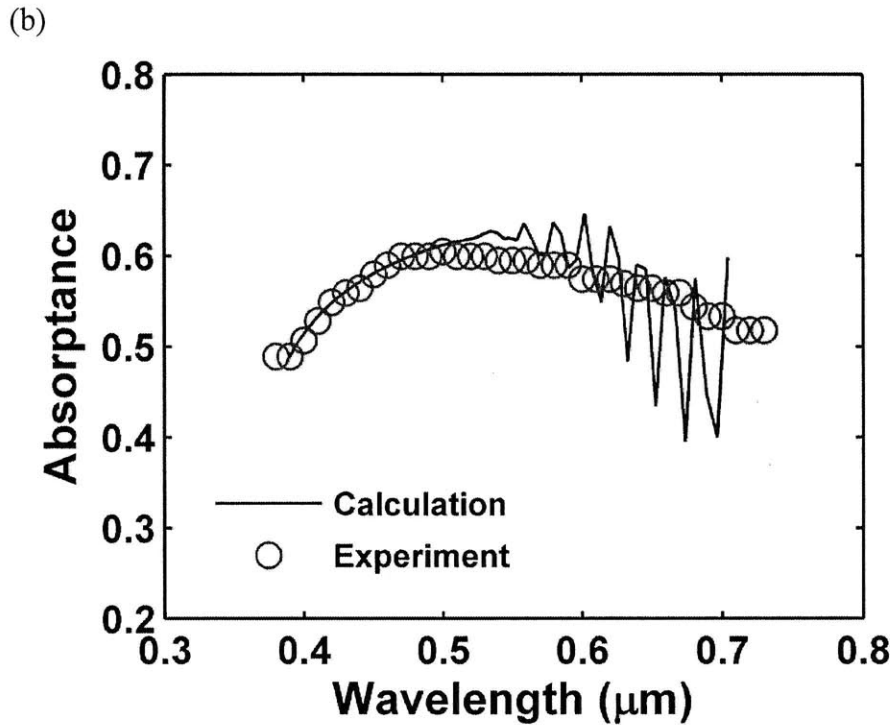
Figure 4-7: (a) Microscope image of the bi-material microcantilever with a silicon thin film attached on it; (b) Spectral absorptances of a 2 μm thick silicon thin film. The absorptance is calculated from Fresnel formulas, assuming the silicon thin film is sandwiched between two semi-infinite air layers.

Figure 4-8 shows the typical deflection signals of the cantilever as the wavelength of the incident light changes. Each step in Fig. 4-8 corresponds to one wavelength with a 10 nm interval. During the measurement, we also hold each wavelength for a few seconds, thus the deflection signal does not change and is seen as a "plateau". The deflection signal under one single wavelength is not a constant but exhibits some oscillations, as shown in the inset of Fig. 4-8. These oscillations represent the measurement noise which limits the sensitivity of our measurement. The fundamental noise limitation is determined by the thermal vibration noise of the cantilever [21]. For frequencies well below the

natural resonant frequency of the cantilever, the root-mean-square thermal noise amplitude can be calculated by

$$\sqrt{\langle z_{th} \rangle^2} = \sqrt{\frac{4k_b TB}{k w_0 Q}},$$ (4-24)

where k_b is Boltzmann constant, T is temperature, B is the measurement bandwidth, k is the spring constant of the cantilever, w_0 is its resonant frequency, and Q is its quality factor. k, w_0, Q can be measured using a standard AFM. B is determined by the parameters of the lock-in amplifier.

The sensitivity of our measurement can also be estimated from the experimental data of power calibration and cantilever deflection measurement. From the power calibration in Fig. 4-5, the power of the light impinging on the cantilever can be calculated by the ratio of the cross sectional area of the optical fiber to the area of the sample. In the case of the gold sample, once the absorptance of gold is measured in Fig. 4-6 (a), the power absorbed by the gold layer at the certain wavelength Q_λ is known. As discussed in Chapter 2, the deflection of the cantilever is linear together with its absorbed power. Hence, based on the deflection signal V_λ (Fig. 4-8) and the noise level ΔV (the inset of Fig. 4-8) at that wavelength, we can estimate the sensitivity of our measurement by calculating $S = \Delta V \dfrac{Q_\lambda}{V_\lambda}$. In Fig. 4-8, the sensitivity is calculated to be ~ 1 nW, which limits the minimum measurable power. Although we estimate the sensitivity using the data at one wavelength, the sensitivity and the noise level are independent of the wavelength, as shown in Eq. (4-24). As discussed in Section 4.2.2, a sensitivity of 1 nW is required to measure the absorption of a submicron diameter silicon wire with a length

of 50 μm. The demonstrated sensitivity of 1 nW in Fig.4-8 is therefore able to measure the optical absorption of a submicron wire with a length of 50 μm or an even thinner wire with a longer length than 50 μm. The sensitivity in our present measurement is poorer than the literature values [21], which is ~ 100 pW, because we used a smaller time constant for the lock-in amplifier and therefore a larger measurement bandwidth. By increasing the time constant used for the lock-in amplifier, the sensitivity of our measurement can be improved, and thus the optical absorption of a thinner (much smaller than 1 μm) or shorter (smaller than 50 μm) nanowire can be measured. Our present technique shows great potential to characterize the optical properties of individual nanowires.
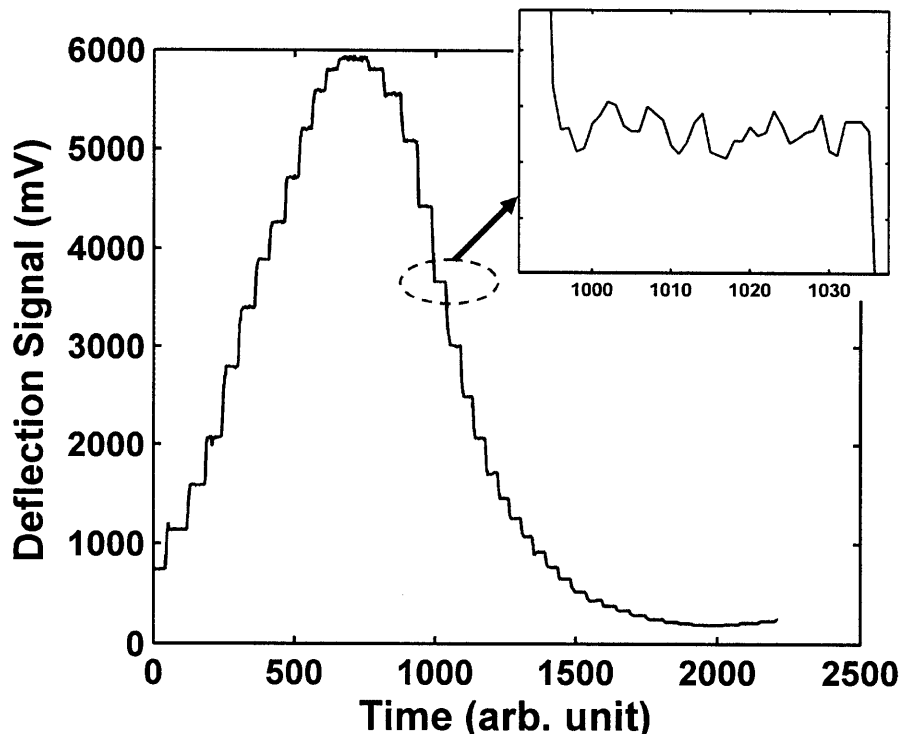
Figure 4- 8: A typical deflection signal of the cantilever. Inset: the oscillation of the deflection signal at a certain wavelength.

In summary, we described an experimental setup which is able to directly measure the spectral absorption of individual micro/nanostructures in application to solar photovoltaics. We have demonstrated the optical absorption measurements for thin metal films and a thin silicon film. The present technique in this thesis is shown to be sensitive enough to characterize the optical properties of individual nanowires. The optical properties of such nanostructured solar cells over the solar spectrum are crucial for their performance. The characterization of the optical properties of individual micro/nanostructures will guide the optimization of dimension, shape, and material selections in order to maximize the efficiencies of solar cells.

4.4 References

[1] Baxter, J. *et al.* Nanoscale design to enable the revolution in renewable energy. *Energy Environ. Sci.* **2**, 559–588 (2009).

[2] Tian, B. Z. *et al.* Coaxial silicon nanowires as solar cells and nanoelectronic power sources. *Nature* **449**, 885–889 (2007).

[3] Fan, Z. *et al.* Three-dimensional nanopillar-array photovoltaics on low-cost and flexible substrates. *Nature Mat.* **8**, 648-653 (2009).

[4] Hu, L. & Chen, G. Analysis of Optical Absorption in Silicon Nanowire Arrays for Photovoltaic Applications, *Nano Lett.* **7**, 3249-3252 (2007).

[5] Zhu, J. *et al.* Enhancement in Amorphous Silicon Nanowire and Nanocone Arrays" *Nano Lett.* **9**, 279-282 (2009)

[6] Derkacs, D. *et al.* Optical Absorption Nanoparticle-induced light scattering for improved performance of quantum-well solar cells. *Appl. Phys. Lett.* **93**, 091107 (2008).

[7] Beck, F. J., Polman, A. & Catchpole, K. R. Tunable light trapping for solar cells using localized surface plasmons. *J. Appl. Phys.* **105**, 114310(2009)

[8] McPheeters, C. O. *et al.* Improved performance of InGaAs/GaAs quantum dot solar cells via light scattering by nanoparticles. *J. Appl. Phys.* **106**, 056101 (2009).

[9] Kelzenberg, M. D. *et al.* Enhanced absorption and carrier collection in Si wire arrays for photovoltaic applications. *Nature Mat.* **9**, 239-244 (2010).

[10] Cao, L. *et al.* Engineering light absorption in semiconductor nanowire devices. *Nature Mat.* **8**, 643-647 (2010).

[15] Bohren, C. F & Huffman, D. R. *Absorption and Scattering of Light by Small Particles* (Wiley-Vch, Weinheim, 2004).

[16] Modest, M. *Radiative Heat Transfer* (Academic Press, 2003).

[17] Mie, G. A. Beiträge zur Optik trüber Medien, speziell kolloidaler Metallösungen. Leipzig, *Ann. Phys.* **330**, 377–445 (1908).

[18] Rayleigh, L. On the light from the sky, its polarization and colour. *Philos. Mag.* **41**, 107-120, 274-279 (1871).

[19] Maier, S. A. *Plasmonics: Fundamentals and Applications* (Springer, 2007).

[20] Su, K. - H. *et al.* Interparticle coupling effects on plasmon resonances of nanogold particles. *Nano Lett.* **3**, 1087-1090 (2003).

[21] Barnes, J. R., Stephenson, R. J., Welland, M. E., Gerber, C. & Gimzewski, J. K. Photothermal spectroscopy with femtojoule sensitivity using a micromechanical device. *Nature* **372**, 79-81 (1994).

[22] Palik, E. *Handbook of Optical Constants of Solids* (Academic Press, 1985).

[23] Varesi, J., Lai, J., Perazzo, T., Shi, Z. & Majumda, A. Photothermal measurements at picowatt resolution using uncooled micro-optomechanical sensors *Appl. Phys. Lett.* **71**, 306 (1997).

Chapter 5: High thermal conductivity polymer nanofibers

5. 1 Introduction

Bulk polymers are generally regarded as thermal insulators and have thermal conductivities on the order of 0.1 W/m.K [1]. Typical methods for improving polymer thermal conductivity have often focused on composite materials, where additives, such as metallic nanoparticles or carbon nanotubes, are embedded in polymer matrices [2, 3]. In particular, the use of carbon nanotubes as an additive has been motivated by reports that individual tubes have high thermal conductivities [4]. The thermal conductivity enhancement in polymer carbon nanotube composites, however, is usually limited to within one order of magnitude due to the high thermal interface resistance between the additives and the polymer matrix [5, 6].

The alignment of polymer chains, on the other hand, can yield large enhancement on the mechanical strength and thermal conductivity of polymers [7, 8]. In the limit of an individual chain of polyethylene which is the simplest and the most widely used polymer

illustrated in Fig. 5-1, Henry and Chen [9] used molecular dynamics simulation to study the heat conduction along the molecular chain. They found that the thermal conductivity of one individual polymer chain can be very high (~ 350 W/m.K) (black curve in Fig. 5-1) or even divergent in some cases (red curve in Fig. 5-1), consistent with the nonergodic characteristics of one-dimensional conductors originally studied by Fermi, Pasta and Ulam [10]. Several experimental studies have shown that self assembled monolayers of aligned polyethylene chains also exhibit a very high thermal conductance [11, 12]. Although the polyethylene chains were theoretically and experimentally demonstrated to have a very high thermal conductivity, practical applications may require these polymers to be fabricated as fibers or films.
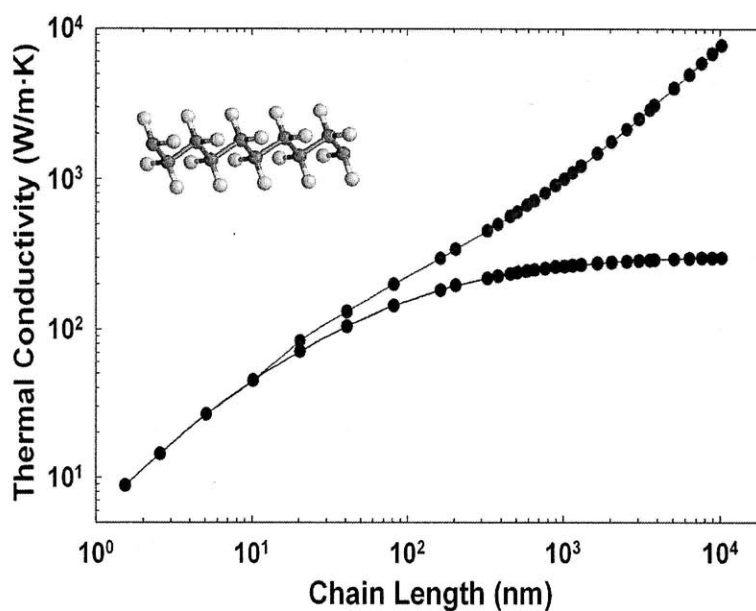
(Henry and Chen, Phys. Rev. Lett., 2008)

Figure 5-1: Thermal conductivity prediction for a single polyethylene chain from molecular dynamics simulation

94

(a)
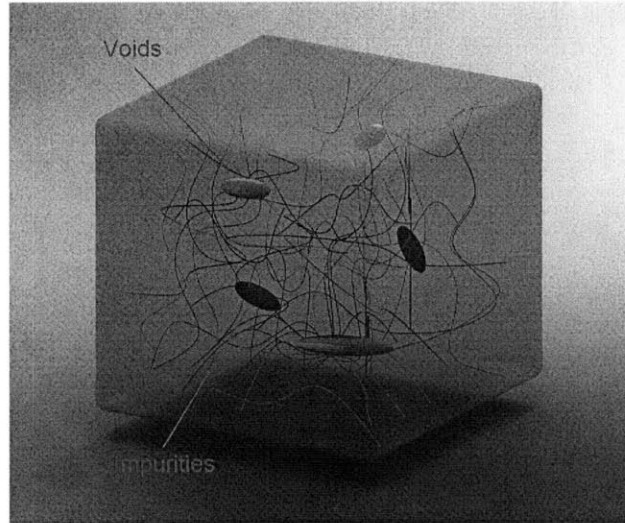
(b)
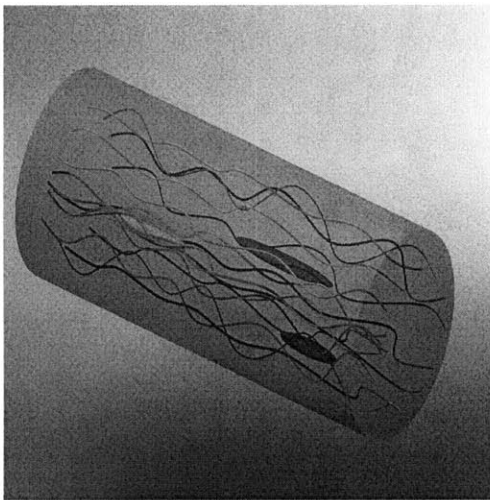
(c)
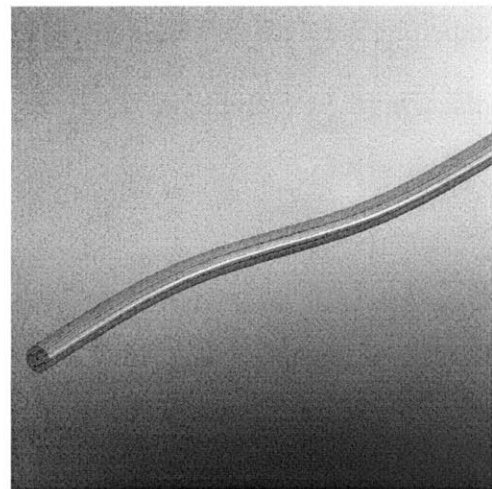
Figure 5- 2: (a) Bulk polyethylene containing chain ends, entanglements, voids and defects. (b) Stretched PE microfiber. (c) "Ideal" polyethylene nanofiber with perfectly aligned molecular chains.

In bulk polyethylene, however, the defects (polymer chain ends, entanglement, voids and impurities, *etc.*) (Fig. 5-2 (a)) all act as stress concentration points and phonon scattering sites for heat transfer [13]. As a result, bulk polyethylene has low strength and low thermal conductivity. For many years, it has been well known that the mechanical and thermal properties of polyethylene can be improved by processing or stretching bulk

samples into thin films or fibers to reduce the number of defects and increase the chain alignment [14, 15]. Commercial oriented polyethylene fibers, with diameters ranging from 10 μm to 25 μm (Fig. 5-2 (b)), have been measured to have an enhanced Young's modulus of ~ 200 GPa and a thermal conductivity of 30-40 W/m.K at around room temperature [16, 17]. In this thesis, the polyethylene fiber size is further scaled down to submicron diameters. A new method is developed to fabricate ultradrawn nanoscale fibers (Fig. 5-2 (c)). The thermal conductivity of these nanofibers reached as high as 104 W/m.K, which is higher than that for many metals. Section 5.2 introduces the detailed fabrication process of ultradrawn polyethylene nanofibers. Section 5.3 describes the experimental techniques to measure the thermal conductivity of the nanofibers and discusses the experimental results.

5.2 Fabrication of ultradrawn polyethylene nanofibers

The technique presented in this thesis to fabricate high-quality ultra-drawn polyethylene nanofibers uses a two-stage-heating method. A decalin solution, containing 0.8 wt. % ultrahigh molecular weight polyethylene (molecular weight 3-6 million, Alfa Aesar), is prepared by heating the polymer-solvent mixture at 145 °C [8]. To prevent the degradation of polyethylene, the dissolution was carried out under nitrogen. The solution is then quenched in water to form a gel. The nanofiber pulling system is illustrated in Fig. 5-3. The fabrication of the ultradrawn polyethylene nanofibers in the present work includes two steps. First, a small sample of wet gel is heated by heater 1. After reaching 120 °C, the heater is turned off to reduce the evaporation of the solvent from the gel and a

100-200 μm long suspended fiber is rapidly drawn using a sharp tungsten tip or an AFM cantilever [18, 19], which is fixed on a motorized stage. Second, heater 2, located underneath the fiber and heater 1, is used to heat the fiber and surrounding air to ~ 90 °C. After several seconds, when the two ends of the fiber dry out and solidify, further drawing is conducted by moving the tungsten tip or the AFM cantilever at a speed of ~ 1 μm/s to achieve the higher draw (stretching) ratios.
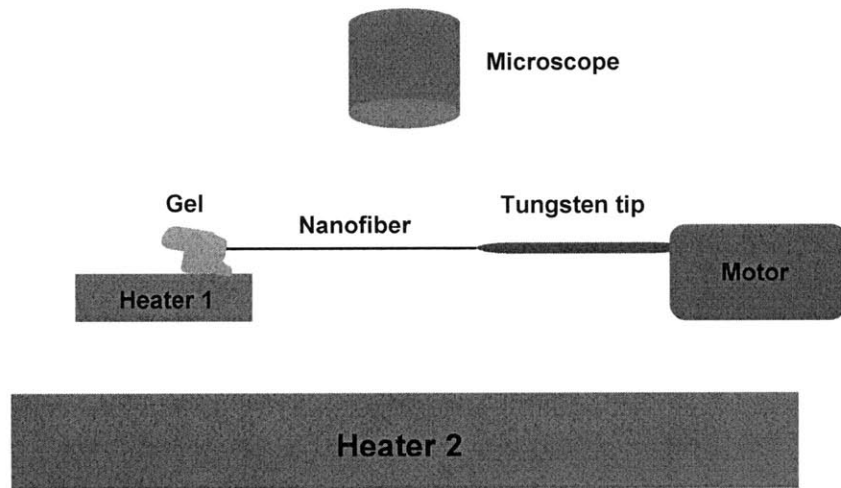
Figure 5- 3: Schematic diagram of experimental setup to fabricate ultradrawn nanofibers

The properties of polyethylene nanofibers are highly dependent on their draw ratio. A higher draw ratio means a better polymer chain alignment, and therefore a higher thermal conductivity or Young's modulus. To estimate the draw ratio in Step 1, we approximate the polyethylene gel, before deformation, as a thick cylinder with diameter D_1 and length L_1 (Fig. 5-4 (a)), and assume that the deformation caused by drawing in Step 1 only occurs in the thick cylinder. In reality, the two ends are conically shaped, but for approximation purposes, we neglect the change in volume within the conical ends.

The end of the AFM cantilever used in the drawing process is ~ 4 μm wide. We assume the diameter of the initial cylinder is $D_1 = \sim 6$ μm, accounting for the heated polymer gel flowing over the cantilever end due to the capillary force when the AFM cantilever dips into it. After the drawing in Step 1, the length of the polyethylene fiber was measured to be $L_2 = 100\text{-}200$ μm and the diameter, $D_2 = 1.5\text{-}2.5$ μm (Fig. 5-4 (b)). Based on volume conservation within the cylindrical section, we can calculate L_1 by $\dfrac{\pi D_1^2 L_1}{4} = \dfrac{\pi D_2^2 L_2}{4}$.

Hence, the draw (stretching) ratio in Step 1 can be estimated to be $\dfrac{L_2}{L_1} = \dfrac{D_1^2}{D_2^2} \approx 6 \sim 16$. In Step 2, the final length of the nanofiber L_3 has been successfully drawn in the range of 1,000-10,000 μm (Fig. 5-4 (c)), thus giving a draw ratio of $\dfrac{L_3}{L_2} \approx 10 \sim 50$. The overall draw ratio in the two steps is thus $\dfrac{L_3}{L_1} = \dfrac{L_3}{L_2} \cdot \dfrac{L_2}{L_1} \approx 60 \sim 800$ for ultradrawn nanofibers.

Such a large range in draw ratio is indicative of our ability to control the geometrical parameters of our nanofiber samples; though certainly, higher draw ratios are more difficult to achieve.

(a)

(b)

(c)
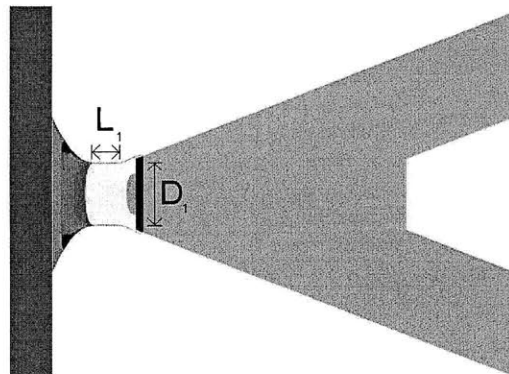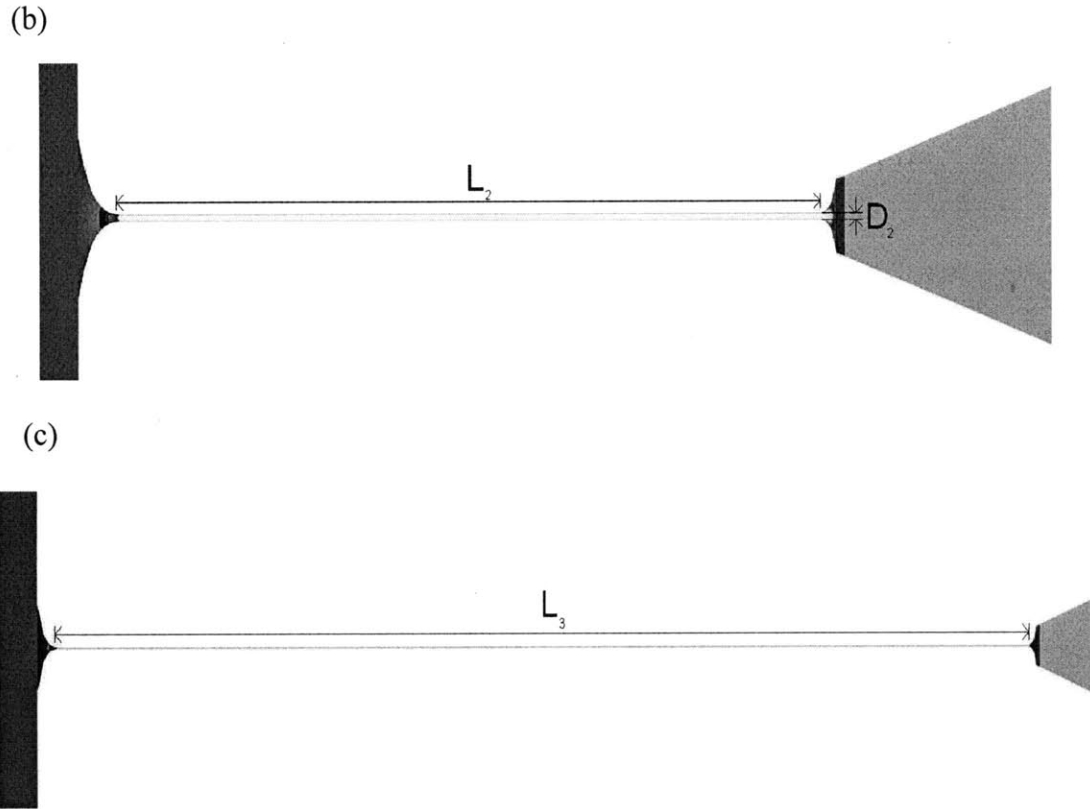
Figure 5- 4: Two-step drawing process for fabricating the nanofibers

Most of the fabricated nanofibers have uniform diameters between 50-500 nm and lengths up to tens of millimeters. Figures 5-5 (a) and (b) show a transmission electron microscope (TEM) micrograph and diffraction pattern for one sample of our ultra-drawn polyethylene nanofibers fabricated by a tungsten tip, respectively. The periodic diffraction spots could be distinctly indexed to an orthorhombic phase with lattice constants $a = 7.422$Å, $b = 4.949$ Å and $c = 2.544$ Å for polyethylene [20]. The arrow in Fig. 5-5 (b) indicates the drawing direction. This pattern shows the strong single crystal nature of the fabricated polyethylene nanofibers, with the c- (molecular) axis lined up in

the drawing direction and the *a*-axis normal to the fiber axis. This confirms that the stretching effect (ultra-drawn) in the nanofibers (Fig. 5-5 (b)) does indeed contribute to the nanoscale restructuring of the polymer chains, with the improvement in fiber quality leading to more "ideal" single crystalline fibers (Fig. 5-2 (c)).

(a)   (b)

500 nm
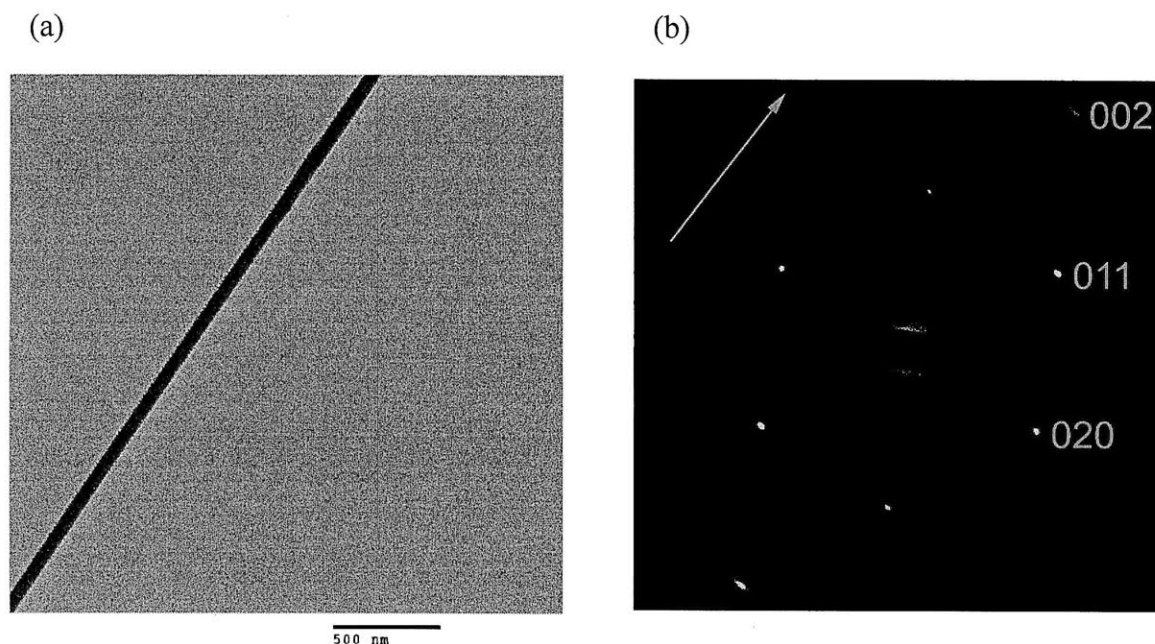
Figure 5- 5: (a) TEM image of an ultradrawn polyethylene nanofiber. (b) TEM diffraction image of the ultradrawn polyethylene nanofiber. The arrow represents the drawing direction.

5.3 Experimental investigation

To measure the thermal conductivity of an individual nanofiber, we have developed a general approach for thermal measurements of compliant nanofibers or nanowires using a sensitive bi-material AFM cantilever, which can resolve power measurements as low as 0.1 nW and energy measurements down to 0.15 pJ [21, 22], as discussed in Chapter 2.

Our experimental setup is illustrated in Fig. 5-6. A nanofiber is directly drawn by a bi-material (Si_3N_4/Au) AFM cantilever, which minimizes the thermal contact resistance between the fiber and the cantilever. The nanofiber is then mechanically cut ~ 300 μm away from the tip to reduce radiation loss from the fiber to the environment. Next, the setup is placed under high vacuum (~ 50 μTorr). A laser (wavelength λ = 650 nm) is focused onto the tip of the cantilever and reflected onto a position sensing detector (bi-cell photodiode), which measures the deflection of the cantilever. The free end of the fiber is attached with conductive silver epoxy to a micro thermocouple (junction diameter of ~ 50 μm), which is mounted onto the tip of a steel needle. Its temperature can be adjusted by heating the needle with a small electrical resistance heater. By varying both the laser power and the temperature of the micro thermocouple, we can determine the conductance of polyethylene nanofiber by measuring the deflection of the cantilever. More technical details will be described in the following sections. To eliminate the effect of thermal expansion, a motorized control stage was used to reduce the distance between the cantilever and the thermocouple until the nanofiber was no longer under tension (Fig. 5-6), which was indicated by the point where the deflection signal stopped changing with further stage movement. We were not successful measuring polymer fibers with diameters in the micron range because the higher stiffness of these fibers affected the deflection of the cantilever via the thermal expansion of the fiber.
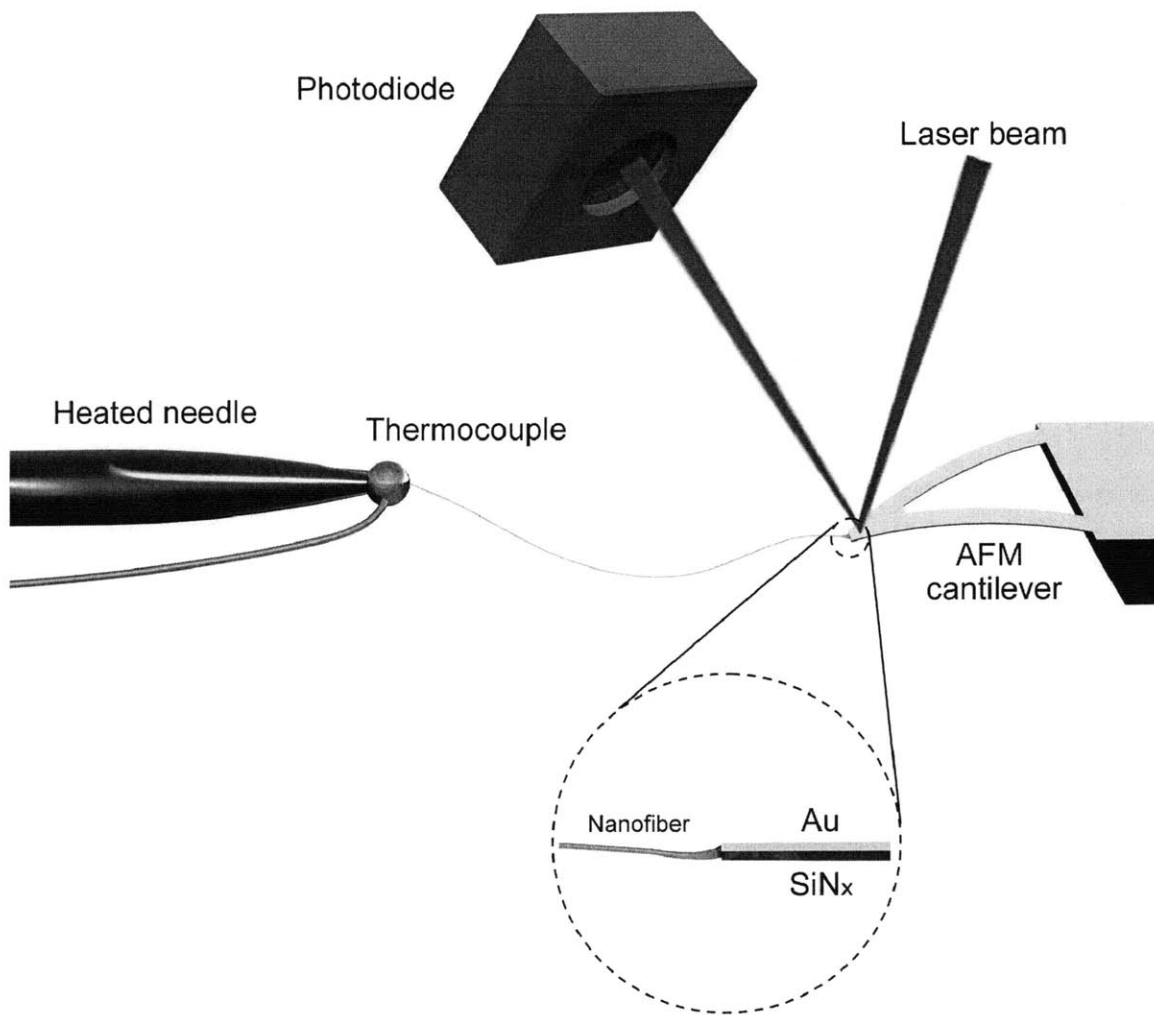
Figure 5-6: Schematic diagram of the experimental setup used to measure the thermal properties of a single ultradrawn nanofiber. The nanofiber drawn from the AFM cantilever is loosely suspended between a micro thermocouple and the AFM cantilever.

5.3.1 Thermal conductivity measurement system

The thermal conductivity measurement system can be represented by a three-junction thermal circuit with two thermal resistances corresponding to the polyethylene nanofiber and the AFM bi-material cantilever, as shown in Fig. 5-7. The two quantities that are varied during the measurement are the laser power absorbed by the cantilever Q_B

and the temperature of the thermocouple T_A. The specific thermal resistance of the nanofiber is ~10^9 K/W, while typical thermal contact resistance between two solids is usually 10^7-10^8 K/W range [23]. In addition, we have also used silver epoxy to join the nanofiber and the thermocouple, thus increasing the contact area. Hence, the thermal contact resistance at the two ends of the nanofiber is neglected in the following analysis. Note that if there is thermal contact resistance, the fiber thermal conductivity will be higher than reported values. The nanofiber is assumed to be uniformly cylindrical along its length. Although irregularities at the ends are possible, they are neglected in this analysis. The SEM images of the nanofiber justify this assumption. All the measurements are done under high vacuum and therefore heat convection from air is negligible. Based on the low emissivity (~ 0.1) of the microfiber [24, 25], the emissivity of the nanofiber is estimated to be smaller than 0.1 according to Rayleigh scattering theory where emissivity is proportional to the volume [26]. Due to such a low emissivity (< 0.1) of the nanofiber and the small temperature difference between the nanofiber and the surroundings, the radiation loss from the fiber is estimated to be < 1 nW, which is negligibly small compared to the heat conduction (~ 100 nW) through the nanofiber. As an approximation, the heat input from the laser can be modeled as an input at point B. But, in reality, the distance between the cantilever tip and the laser spot on the cantilever was estimated to be ~ 20 μm. Since the cantilever is very thermally conductive, as discussed in Chapter 2, the thermal resistance between the cantilever tip and the laser spot is neglected in the heat transfer model. This assumption will be justified in subsequent sections.
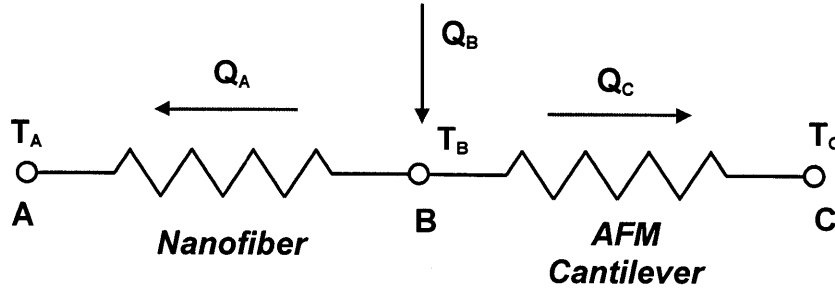
Figure 5-7: Three-junction thermal circuit model for analyzing heat transfer in the experiment

The two-step measurement process developed in this thesis can be understood as follows. In the first step, we calibrate the bending of the cantilever by varying the laser power. In the second step, we measure the heat transfer via the nanofiber by varying the thermocouple temperature. These two steps are further explained below.

Step 1: Calibration via Varying of Laser Power

At steady state, the heat balance of the three junctions at point B in Fig. 5-7 is,

$$Q_B = Q_A + Q_C,$$ (5-1)

where Q_B is the laser energy absorbed by the cantilever. Q_A is heat conduction through the nanofiber and Q_C the heat conduction through the cantilever. Since the thermal conductance of the AFM cantilever G_C (~ 10 μW/K) is around three orders of magnitude larger than the thermal conductance of the nanofiber G_F (~10 nW/K), the heat conduction through the nanofiber ΔQ_A (~ 100 nW) can be ignored compared to the change of the absorbed power ΔQ_B (~ 10 μW) at point B. Equation (5-1) can then be written in differential form as follows,

$$\Delta Q_B = \Delta Q_C,$$ (5-2)

In Fig. 5-8, we can obtain the bending $\Delta B_{(P_1-P_2)}$ when the absorbed power on the cantilever tip changes from P_1 to P_2. Since the bending signal measured by the photodiode is effectively a representation of the cantilever temperature, which is proportional to the heat transfer through the cantilever, Q_C, it can also be shown that,

$$\Delta Q_{C(P_1-P_2)} = \alpha_1 \cdot \Delta B_{(P_1-P_2)}, \tag{5-3}$$

where α_1 is a proportionality constant, determined by the properties and dimensions of the cantilever [27]. From Eqs. (5-2) and (5-3), we have,

$$\alpha_1 = \frac{\Delta Q_{B(P_1-P_2)}}{\Delta B_{(P_1-P_2)}}, \tag{5-4}$$
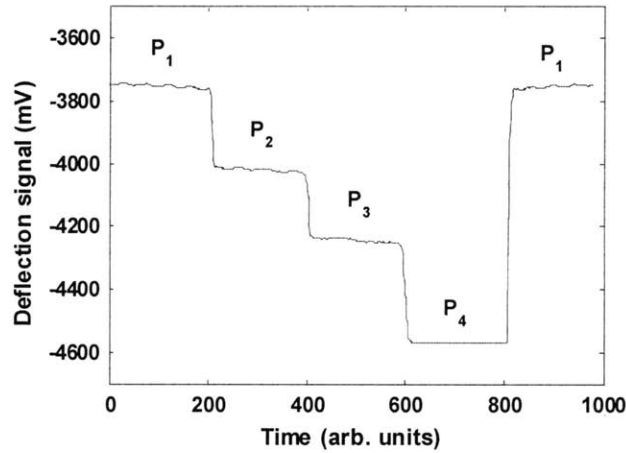
Figure 5-8: Experimental data measured by varying the absorbed power on the end of the AFM cantilever

Step 2: Variation of Thermocouple Temperature

The second step measures the heat transfer changes through the nanofiber when the temperature of the thermocouple is changed. The laser input to the cantilever is held

constant. In Fig. 5-9, when the temperature of the thermocouple T_A changes from T_{A1} to T_{A2}, the heat fluxes through the nanofiber can be expressed as,

$$Q_{A1} = G_F(T_B - T_{A1}),\qquad(5\text{-}5)$$

$$Q_{A2} = G_F(T_B - T_{A2}),\qquad(5\text{-}6)$$

where G_F is the thermal conductance of the nanofiber. Since G_C is much larger than G_F, the temperature of cantilever tip T_B is assumed as a constant during the temperature change of the thermocouple. The heat conducted through the nanofiber in the experiment is estimated to be ~100 nW which corresponds to a ~ 10^{-2} K temperature change on T_B. This justifies our assumption. Thus, subtracting Eq. (5-6) from Eq. (5-5), we have,

$$\Delta Q_{A(T_{A1}-T_{A2})} = -G_F \Delta T_{A1-A2},\qquad(5\text{-}7)$$

where ΔT_{A1-A2} can be obtained by the thermocouple measurement. In Fig. 5-9, we can also obtain the bending $\Delta B_{(T_{A1}-T_{A2})}$ of the cantilever caused by the temperature change from T_{A1} to T_{A2}. Similarly, we can relate the heat flux through the cantilever and the bending of the cantilever by,

$$\Delta Q_{C(T_{A1}-T_{A2})} = \alpha_2 \cdot \Delta B_{(T_{A1}-T_{A2})},\qquad(5\text{-}8)$$

where $\Delta Q_{C(T_{A1}-T_{A2})}$ is the change of the heat flux through the cantilever due to the temperature change from T_{A1} to T_{A2}, and α_2 is a proportionality constant when changing the temperature of the thermocouple. Because this measurement is intrinsically differential, we can measure minute changes in the heat conducted through the nanofiber. Thus, despite the high thermal resistance of the nanofiber, which causes a very small change in bending, this relative change is still clearly discernable due to the high sensitivity of the cantilever (Fig. 5-9).
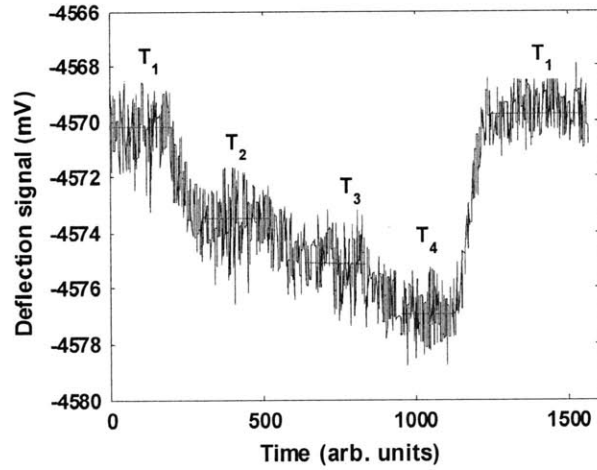
Figure 5-9: Experimental data measured by varying the temperature of the thermocouple

In Step 2, the absorbed laser power Q_B does not change ($\Delta Q_B = 0$). This leads to the following,

$$\Delta Q_A = -\Delta Q_C, \tag{5-9}$$

Thus, based on Eqs. (5-8) and (5-9), we have,

$$\Delta Q_{A(T_{A1}-T_{A2})} = -\Delta Q_{C(T_{A1}-T_{A2})} = -\alpha_2 \cdot \Delta B_{(T_{A1}-T_{A2})}, \tag{5-10}$$

From Eqs. (5-7) and (5-10), the proportionality constant α_2 can be expressed as,

$$\alpha_2 = G_F \cdot \frac{\Delta T_{A1-A2}}{\Delta B_{(T_{A1}-T_{A2})}}, \tag{5-11}$$

In these two cases, the proportionality constants α_1 and α_2 are equal, which will be proved in the next section. In terms of Eqs. (5-4) and (5-11), the thermal conductance of the nanofiber can be expressed by,

$$G_F = \frac{\Delta Q_{B(P_1-P_2)} / \Delta B_{(P_1-P_2)}}{\Delta T_{A1-A2} / \Delta B_{(T_{A1}-T_{A2})}}. \tag{5-12}$$

107

In Fig. 5-10 (a) and (b), the cantilever deflection is plotted as a function of both the power absorbed by the cantilever and the thermocouple temperature, respectively, for two repeated measurements on the same sample. $\Delta Q_{B(P_1-P_2)} \big/ \Delta B_{(P_1-P_2)}$ and $\Delta T_{A(1-2)} \big/ \Delta B_{(T_{A1}-T_{A2})}$ can be obtained from the slopes of Figs. 5-10 (a) and (b), respectively. The thermal conductivity of the fiber can then be found by assuming one-dimensional heat transfer along the fiber,

$$K_F = \frac{4G_F L}{\pi d^2},$$ (5-13)

where L and d are the length and the diameter of the nanofiber, respectively. It should be emphasized that though it may appear that the fiber conductance is independent of the cantilever conductance in Eq. (5-12), the effect of the cantilever conductance is actually embedded within the measured bending signals.

(a)

(b)
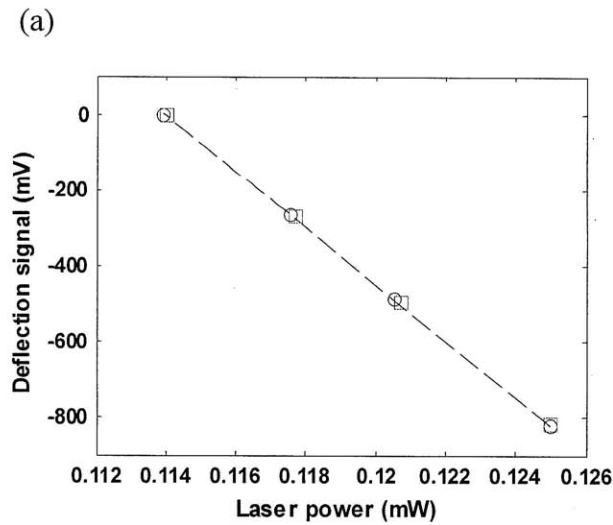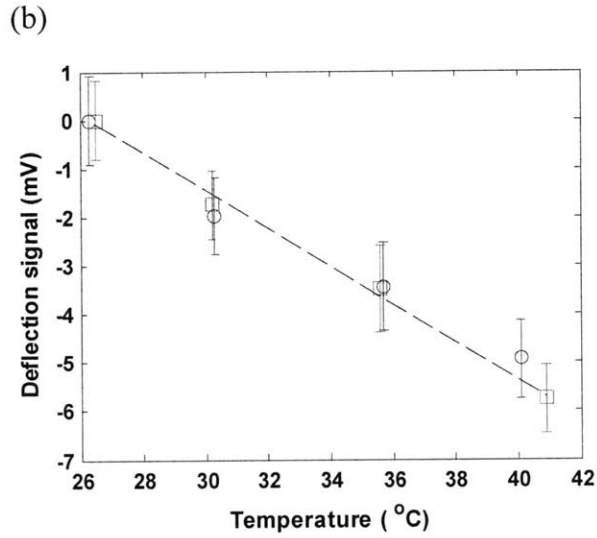
Figure 5- 10: (a) Reduced deflection signals from Fig. (5-7) versus the absorbed power. The data is normalized to the deflection signal at P_1. (b) Reduced deflection signals of the AFM cantilever from Fig. (5-8) versus the temperature of the thermocouple. The data is normalized to the deflection signal at T_1. The data in (a) and (b) are from two repeated trials on one individual sample and marked as blue circles and green squares, respectively. The dashed black lines are the linear fits. The error bar is ~ 0.6 mV in (a).

From the above discussion, we see that the differential heat transfer through the nanofiber is directly measured from the change of the bending in the cantilever, since the initial bending of the cantilever is well recorded by the photodetector (Fig. (5-8) and Fig. (5-9)). Although the nanofiber thermal conductance is much smaller than that of the cantilever, our technique allows direct measurement of very small heat transfer (~ 10 nw) through the nanofiber.

5.3.2 Proportionality constants α_1 and α_2

Based on the beam theory presented in Chapter 2, we will prove that proportionality constants α_1 and α_2 are equal. In calibrating the cantilever bending, the

laser spot inputs heat at a point to the cantilever at some distance x_1 (~20 μm) from the tip. The calibrated bending constant is α_1. In the second step of the experiment, heat is transferred at the tip-nanofiber junction (~x=0) and the corresponding bending constant is α_2. In both cases, the bending of the cantilever is measured at $x = x_1$, where the laser spot is located. We will show that α_1 is equal to α_2.

For case 1, when the laser power is delivered to the cantilever, as shown in Fig. 5-11 (a), the temperature profile at steady state is [22, 28],

$$T(x) - T_0 = \left(1 - \frac{x}{l}\right)\frac{P_1}{G}, \quad \text{for} \quad x_1 \le x \le l, \tag{5-14}$$

where l is the effective length of the cantilever ($l = 200$ μm), G is the effective thermal conductance of the cantilever and P_1 is the absorbed power. The temperature is constant for $0 \le x \le x_1$ because of the adiabatic boundary condition at $x = 0$. By solving Eq.(2-1) using Eq. (5-14), we have,

$$Z(x) = -(\gamma_2 - \gamma_1)\frac{t_1 + t_2}{t_2^2 KG}(l - x)^3 P_1, \quad \text{for} \quad x_1 \le x \le l$$

Thus, the deflection measured at $x = x_1$ (the location of the laser spot) is,

$$Z(x_1) = -(\gamma_2 - \gamma_1)\frac{t_1 + t_2}{t_2^2 KG}(l - x_1)^3 P_1 = \alpha_1 P_1, \tag{5-15}$$

For case 2, when the heat is conducted through the nanofiber, as shown in Fig. 5-11 (b), the temperature profile at steady state is,

$$T(x) - T_0 = \left(1 - \frac{x}{l}\right)\frac{P_2}{G}, \quad \text{for} \quad 0 \le x \le l, \tag{5-16}$$

By solving Eq. (2-1) using Eq.(5-16), we have,

110

$$Z(x) = -(\gamma_2 - \gamma_1)\frac{t_1 + t_2}{t_2^{\,2} KG}(l - x)^3 P_2, \text{ for } 0 \le x \le l$$

Thus, the deflection measured at $x = x_1$ is,

$$Z(x_1) = -(\gamma_2 - \gamma_1)\frac{t_1 + t_2}{t_2^{\,2} KG}(l - x_1)^3 P_2 = \alpha_2 P_2 \, , \tag{5-17}$$

As can be observed, the two proportionality factors, α_1 and α_2, are equal from Eqs. (5-15) and (5-17),

$$\alpha_1 = \alpha_2 = -(\gamma_2 - \gamma_1)\frac{t_1 + t_2}{t_2^{\,2} KG}(l - x_1)^3 P_2$$

(a)

(b)
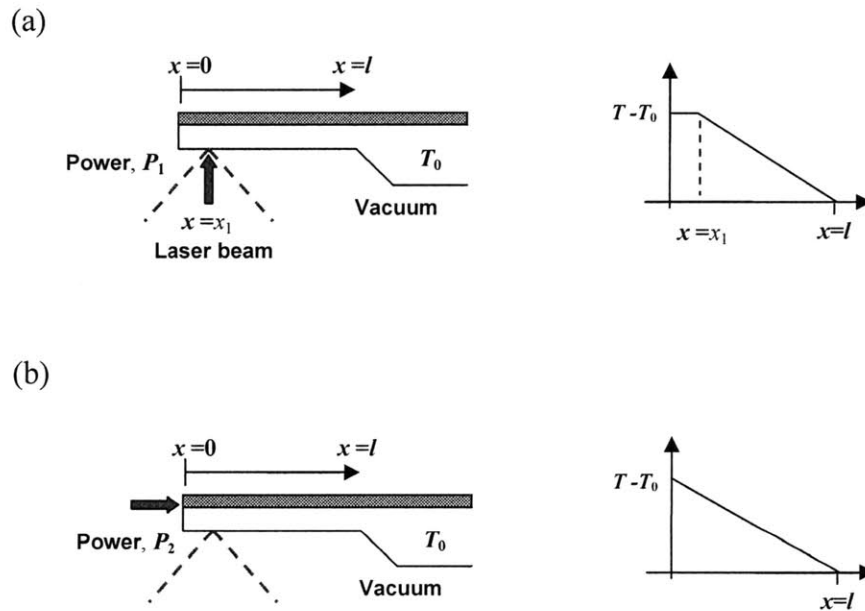
Figure 5- 11: (a) Case 1: configuration and temperature distribution, (b) Case 2: configuration and temperature distribution.

5.3.3 Radiation heat transfer between the cantilever and the needle

Since the whole needle is heated up in order to change the temperature of the thermocouple, the radiative heat transfer between the heated needle and the cantilever also contributes to the bending signals measured in Fig. 5-9. Upon completion of the measurements, both varying the absorbed power of the cantilever and the temperature of the thermocouple, the motorized control stage is used (100 nm step resolution) to move the needle with the thermocouple backwards until breaking the nanofiber. The fiber usually breaks at the fiber-thermocouple attachment due to its high strength; thus the geometry of the thermocouple or the needle will not change. Then, the needle is moved forward to the original location where both measurements were previously conducted and the bending of the cantilever is measured again by varying the temperature of the thermocouple. The observed bending signal without the nanofiber in place is caused only by the radiation transfer between the cantilever and the heated needle (Fig. 5-12). The maximum influence of thermal radiation is ~ 25 %. The deflection signals in Fig. 5-12 and Fig. 5-9 are not in the same range due to the thermal drift of the cantilever. In Fig. 5-10 (b), we have normalized the deflection signals in Fig. 5-12 to ambient temperature (T_1) and subtracted them from the deflection signals in Fig. 5-9. When varying the absorbed power by the cantilever in Fig. 5-8, no correction of radiation is needed because the conductance of the cantilever is much larger.
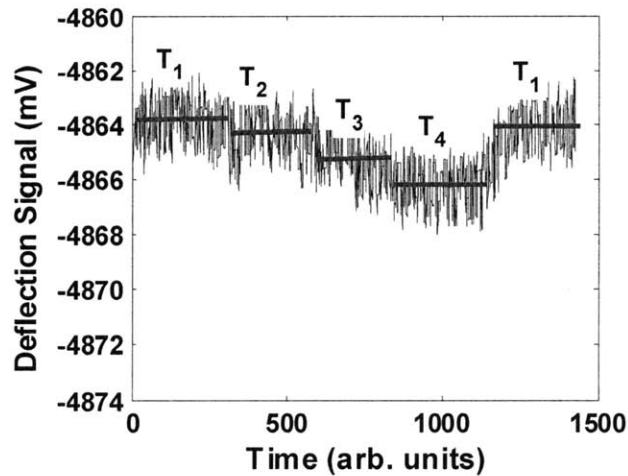
Figure 5- 12: Experimental data of the radiation heat transfer between the heated needle and the AFM cantilever

5.3.4 Laser power absorbed by the cantilever

Following the procedure described in Chapter 2, we measured the radiant power in the incident beam (1.809 mW, 650 nm wavelength), the reflected beam (1.222 mW) and the strayed beam (0.427 mW). Thus, the absorbed power by the cantilever is calculated to be 0.160 mW. The ratio of absorbed to reflected light is 0.131. The accuracy of each power measurement is $\sim$ 0.002 mW which is obtained by multiple measurements. From uncertainty propagation, that would yield an overall error on the absorbed power of $\sim$0.004 mW. The uncertainty of the absorbed power by the cantilever is thus $\sim$ 2.5 %. In Fig. 5-13 (a), the photodiode sum signal of the reflected light is plotted as a function of the reflected laser power. The linear relationship between them corresponds to a slope of 0.6434 mW/V, which is consistent with the measurement in Chapter 2. The absorption of the cantilever can be calculated from the photodiode sum signal as 0.131 $\times$ 0.6434 $\times$ (photodiode sum signal). In Fig. 5-13 (b), we also plot the deflection signal as a function of the sum signal.

(a)

(b)
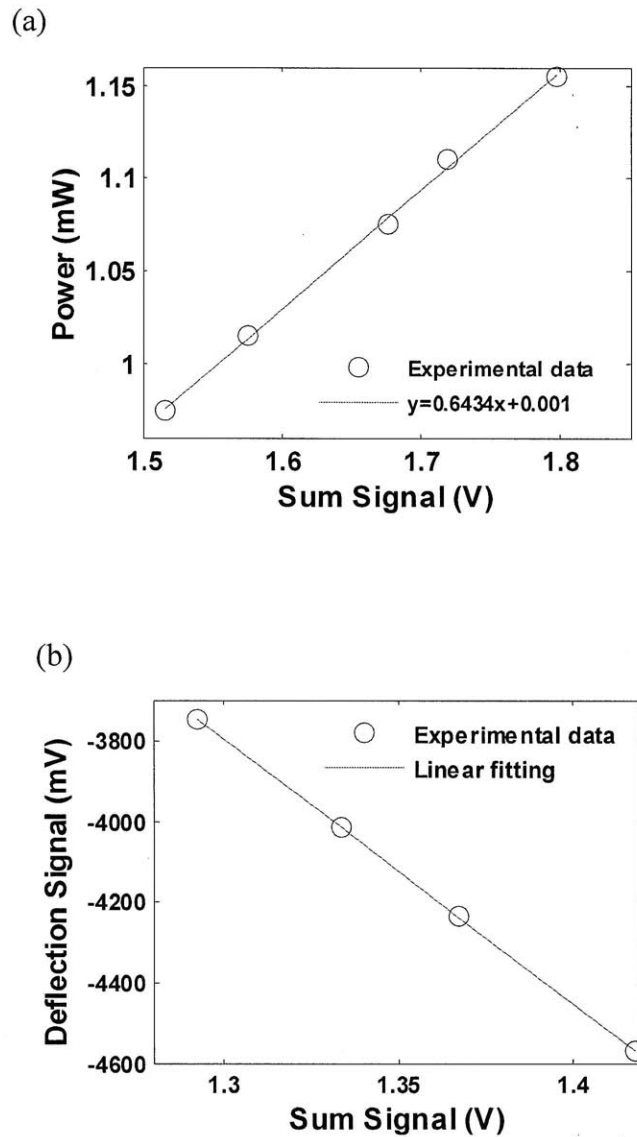
Figure 5- 13: (a) Measured reflected power versus the sum signal of photodiode, (b) Deflection signal versus the sum signal of photodiode.

5.3.5 Thermal conductivity of ultradrawn nanofibers

The length L of each polyethylene nanofiber was measured using optical microscopy and the diameter d was measured using scanning electron microscopy (SEM) at room temperature. Figures 5-14 (a), (b) & (c) show the measured diameters of samples 1, 2 and 3 by SEM, respectively. The uniformity of the samples is evaluated by measuring the

114

diameter at ~ 10 different locations (with varying intervals 2 - 20 μm) along one sample. The standard deviation of the diameter measurements is ~ 12 nm except at the end which is connected with the cantilever. Once the geometry was known, the thermal conductivity of each nanofiber was calculated from the conductance. For each individual sample, two to three measurements were conducted. The results obtained were 103.9 ± 28.1 W/m.K for sample 1 with conductance G = 4.84 ± 0.94 nW/K, diameter d = 131 ± 12 nm and length L = 290 ± 10 μm; 80.4 ± 24.7 W/m.K for sample 2 with G = 5.21 ± 1.35 nW/K, d = 158 ± 12 nm and L = 300 ± 10 μm; 53.3 ± 11.3 W/m.K for sample 3 with G = 5.59 ± 0.95 nW/K, d = 197 ± 12 nm and L = 290 ± 10 μm. The overall draw ratios for three samples are estimated to be: ~ 410 for sample 1, ~ 270 for sample 2 and ~ 160 for sample 3. The measured thermal conductivities for three samples are plotted as a function of draw ratio in Fig. 5-15. We can clearly see that the thermal conductivities of the samples increase with increasing draw ratios. Previous results on micron sized fibers showed that thermal conductivity saturates when the draw ratio is above 100 [11]. The results for our nanofibers, however, are not only significantly higher than previous thermal conductivity values, but also do not exhibit saturation, which indicates that there is still room for significant enhancement.
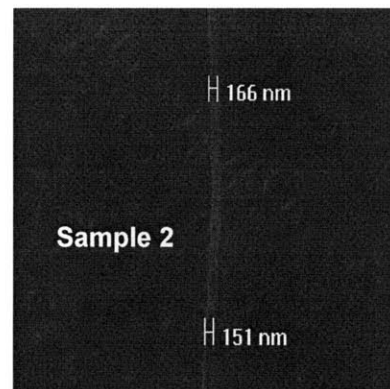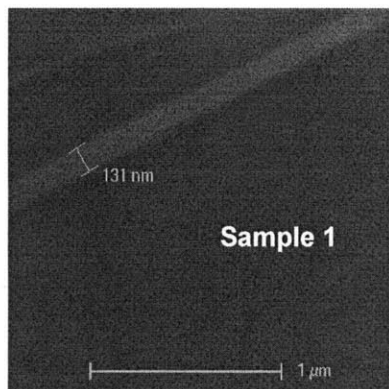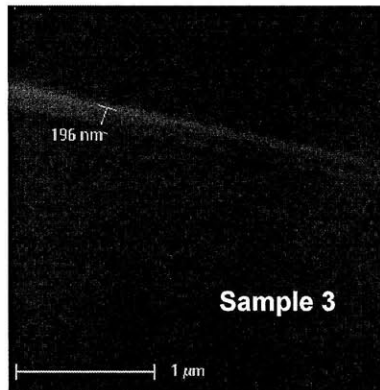
Figure 5-14: SEM images of measured nanofiber samples.
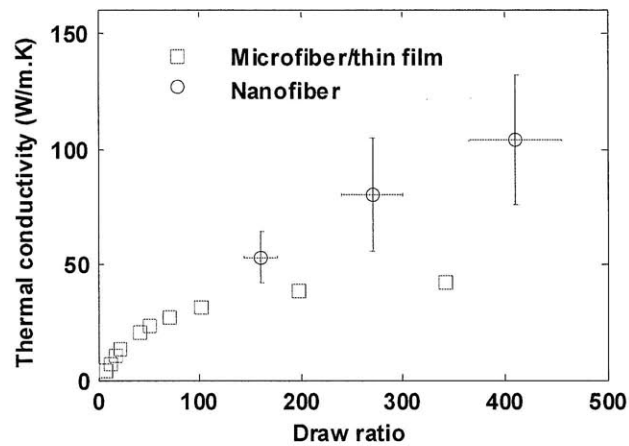
Figure 5- 15: Thermal conductivities of three samples versus their corresponding draw ratios. The data of "Microfiber/thin film" are from Ref. 15.

The highest thermal conductivity of the nanofibers in our work (~ 104 W/m.K) is about 3 times higher than previously reported values for micron sized fibers and approximately 300 times that of bulk polyethylene ~ 0.35 W/m.K. This is significant since the thermal conductivity of condensed matter only spans four orders of magnitude (~ 0.1-1,000). A value of 104 W/m.K is higher than ~ 50% of pure metals such as platinum, iron and nickel [29]. Other metals, in contrast, will have a lower thermal conductivity than pure metals due to alloy and impurity scattering. In comparison, the

previous microfiber samples have thermal conductivities of 30-40 W/m.K [16, 17], which is only in the range of ceramics. To understand the high thermal conductivity of ultradrawn polyethylene nanofibers, we will briefly describe the effect of drawing on the polyethylene structure based on past efforts on drawing micron-sized fibers and thin films [30, 31]. The morphological studies of stretched polyethylene samples confirmed that during the initial drawing process (draw ratio is small), small crystalline blocks are broken off from the crystalline lamellae and incorporated into microfibrils along the draw direction. In these microfibrils, the crystalline blocks are stacked and connected by taut tie molecules (intra-microfibrillar tie molecules) which originate from the partial unfolding of the polyethylene chains. Besides intra-microfibrillar tie molecules, the microfibrils are connected laterally by bridging molecules, which are called inter-microfibrillar tie molecules. Further drawing leads to shear deformation of the microfibrils, resulting in a decrease of the microfibrillar volume fraction and an increase in the number of fully extended interfibrillar tie molecules. Finally, these increasing interfibrillar tie molecules lead to extended chains. The growing chain-extended volume fraction will form a larger average crystal size in the drawing direction. This crystalline region along the drawing direction is the origin for enhanced thermal and mechanical properties. Thus, increasing the length and the volume fraction of the chain-extended crystalline region will enhance the thermal and mechanical properties of ultradrawn polyethylene samples [15].

In nanofibers, the defect density will decrease since inherently larger defects, such as voids, impurities or large entanglement regions, are less likely to be present. Because these types of defects are generally the cause of fracture in the fiber, the successful

drawing of a nanofiber is indicative that a higher quality sample was fabricated, as is also clear from TEM diffraction patterns presented in Fig. 5-5 (b). Smaller defects, such as small entanglement regions and chain ends, may still exist as a part of the amorphous region, but can be partially transformed to become crystalline during the drawing process. As a result, higher draw ratios are more achievable, and a greater volume fraction of the chain extended crystalline region is more attainable at lower draw ratios for the nanofibers. To convey the importance of scale, the diameter of commercial microfibers is typically 10-25 μm. The diameter of nanofibers reported in the current work is 50-500 nm. With identical lengths, the volume of the nanofiber is four orders of magnitude smaller than that of a microfiber; thus, a substantially lower number of defects will exist in the nanofiber than in the microfiber. The improved quality of the nanofibers, when compared to the microfibers, is also supported by plotting thermal conductivity vs. draw ratio (Fig. 5-15). The thermal conductivities of the nanofibers are not only much higher than micron-sized polyethylene materials, but also saturate much slower as a function of draw ratios.

5.3.6 Uncertainty analysis

The total uncertainty incurred during measurement is a composition of multiple uncertainties propagating throughout the experiment. The general formulation for K_F is,

$$K_F = \frac{4G_F L}{\pi d^2} = \frac{4L}{\pi d^2} \cdot \frac{\left(\dfrac{\Delta Q_B}{\Delta B_1} \right)}{\left(\dfrac{\Delta T_A}{\Delta B_2} \right)}$$

From uncertainty propagation rules, the total uncertainty in K_F is,

118

$$\left(\frac{e(K_F)}{K_F}\right)^2 = \left(\frac{e(L)}{L}\right)^2 + 2\left(\frac{e(d)}{d}\right)^2 + \left(\frac{e\left(\frac{\Delta Q_B}{\Delta B_1}\right)}{\left(\frac{\Delta Q_B}{\Delta B_1}\right)}\right)^2 + \left(\frac{e\left(\frac{\Delta T_A}{\Delta B_2}\right)}{\left(\frac{\Delta T_A}{\Delta B_2}\right)}\right)^2, \qquad (5\text{-}18)$$

where the uncertainties of the nanofiber length and diameter are $\sim$ 3% and $\sim$ 8 %, respectively. Therefore, to completely determine the total uncertainty, the uncertainty of each bending measurement must be derived.

In the first measurement where the incident laser power is varied, only the deflection signal and sum signal of the photodector were directly measured. Hence, a conversion is needed to change the sum signal term into absorbed power. This can be accomplished as follows,

$$\Delta Q_B = \left(\frac{P_{absorbed}}{P_{reflected}}\right) \cdot \left(\frac{P_{reflected}}{\Delta Sum}\right) \cdot (\Delta Sum), \qquad (5\text{-}19)$$

where this expression is intentionally written as the product of three terms to utilize previous measurements. The ratio of absorbed to reflected power can be calculated by the power meter data, as previously discussed, and the ratio of the reflected power to the sum signal can be obtained by previous data shown in Fig. 5-13 (a). Thus, the ratio of the absorbed power to the deflection signal is,

$$\frac{\Delta Q_B}{\Delta B_2} = \left(\frac{P_{absorbed}}{P_{reflected}}\right) \cdot \left(\frac{P_{reflected}}{\Delta Sum}\right) \cdot \left(\frac{\Delta Sum}{\Delta B_2}\right), \qquad (5\text{-}20)$$

where the ratio of the sum signal to the bending signal reflects what was actually measured. The estimated error for the absorbed power and the reflected power is thus 0.004 mW and 0.002 mW with averages of 0.160 mW and 1.222 mW, respectively,

$$\left(\frac{e\left(\dfrac{P_{absorbed}}{P_{reflected}}\right)}{\dfrac{P_{absorbed}}{P_{reflected}}}\right) = \left(\frac{e\left(P_{absorbed}\right)}{P_{absorbed}}\right)^2 + \left(\frac{e\left(P_{reflected}\right)}{P_{reflected}}\right)^2 = \left(\frac{2\cdot0.004}{0.160}\right)^2 + \left(\frac{2\cdot0.002}{1.222}\right)^2 = 0.0025$$

In the measurement relating the reflected power to the sum signal (Fig. 5-13 (a)), the standard deviation and range of the reflected power are 0.004 mW and 0.18 mW. Likewise, for the sum signal, they are 0.4 mV and 0.28 V. Note that the reflected power in this instance is different than what was previously used since this quantity is contingent on the sum signal.

$$\left(\frac{e\left(\dfrac{P_{reflected}}{\Delta Sum}\right)}{\dfrac{P_{reflected}}{\Delta Sum}}\right)^2 = \left(\frac{e\left(P_{reflected}\right)}{P_{reflected}}\right)^2 + \left(\frac{e\left(\Delta Sum\right)}{\Delta Sum}\right)^2 = \left(\frac{2\cdot0.004}{0.18}\right)^2 + \left(\frac{2\cdot0.0004}{0.28}\right)^2 = 0.0019$$

Similarly, in the measurement relating the deflection signal of the cantilever to the sum signal (Fig. 5-13 (b)), the standard deviation and range of the deflection signal is 2.21 mV and 823.3 mV. For the sum signal, they are 0.4 mV and 0.125 V. Again, the sum signal considered in this case is different from what was previously used.

$$\left(\frac{e\left(\dfrac{\Delta Sum}{\Delta B_2}\right)}{\dfrac{\Delta Sum}{\Delta B_2}}\right)^2 = \left(\frac{e\left(\Delta Sum\right)}{\Delta Sum}\right)^2 + \left(\frac{e\left(\Delta B_2\right)}{\Delta B_2}\right)^2 = \left(\frac{2\cdot0.0004}{0.125}\right)^2 + \left(\frac{2\cdot2.21}{823.3}\right)^2 = 6.98E-5$$

The total uncertainty of Eq. (5-19) is thus,

$$\left(\frac{e\left(\dfrac{\Delta Q_B}{\Delta B_2}\right)}{\dfrac{\Delta Q_B}{\Delta B_2}}\right)^2 = \left(\frac{e\left(\dfrac{P_{absorbed}}{P_{reflected}}\right)}{\dfrac{P_{absorbed}}{P_{reflected}}}\right)^2 + \left(\frac{e\left(\dfrac{P_{reflected}}{\Delta Sum}\right)}{\dfrac{P_{reflected}}{\Delta Sum}}\right)^2 + \left(\frac{e\left(\dfrac{\Delta Sum}{\Delta B_2}\right)}{\dfrac{\Delta Sum}{\Delta B_2}}\right)^2$$

$$\rightarrow \left(\frac{e\left(\frac{\Delta Q_B}{\Delta B_2}\right)}{\frac{\Delta Q_B}{\Delta B_2}}\right)^2 = 0.0025 + 0.0019 + 6.98E - 5 = 0.00447, \tag{5-21}$$

In the second measurement where the temperature of the heated needle is varied, the temperature is directly measured by an attached thermocouple with a resolution of 0.1 K, as shown in Fig. 5-10(b) in the manuscript. The standard deviation of the deflection signal is $\sim$ 0.6 mV. Because the deflection signal in Fig. 5-10(b) is found by subtracting the radiation signal, caused by the heated needle, from the total signal, an additional error is incurred. Thus the final standard deviation of the deflection signal in Fig. 5-9 is $\sim \sqrt{2} \cdot 0.6\,\mathrm{mV}$. The range of the temperature and deflection considered, is 40 K and 7 mV, respectively, from Fig. 5-10 (b). Note that it was assumed the error was normally distributed, hence two times of standard deviations were taken for a 95% confidence interval. This will be assumed for all subsequent parameters. This results in the following uncertainty,

$$\left(\frac{e\left(\frac{\Delta T_A}{\Delta B_2}\right)}{\frac{\Delta T_A}{\Delta B_2}}\right)^2 = \left(\frac{e(\Delta T_A)}{\Delta T_A}\right)^2 + \left(\frac{e(\Delta B_2)}{\Delta B_2}\right)^2 = \left(\frac{2 \cdot 0.1}{40}\right)^2 + \left(\frac{2 \cdot \sqrt{2} \cdot 0.6}{7}\right)^2 = 0.059, \tag{5-22}$$

Upon substitution of the uncertainties in Eqs. (5-21) and (5-22) into Eq. (5-18),

$$\left(\frac{e(K_F)}{K_F}\right) = \sqrt{(0.03)^2 + 2 \cdot (0.08)^2 + 0.059 + 0.00447} = 0.278 = 27.8\%$$

The values of thermal conductivities of three samples in the main text were averaged based on two or three repeated measurements on one individual sample, and the largest

error among the repeated measurements on each sample was chosen as the error of the sample.

In summary, our measurements of the thermal conductivity for ultra-drawn polyethylene nanofibers (104 W/m.K) have set a new record for the highest thermal conductivity ever reported for a polymer [32]. Our experimental results clearly show the potential of using polymers as a cheaper alternative to conventional metallic heat transfer materials used throughout many industries. This is especially true for applications where directional heat conduction is important, such as in heat exchanger fins, cell-phone casing, plastic packaging for computer chips, *etc*. Furthermore, high thermal conductivity polymers may also have other technological advantages that can be exploited, since they can be lightweight, electrically insulating, and chemically stable. Clearly, more work lies ahead for taking the laboratory results to real world applications.

5.4 References

[1] Sperling, L. H., *Introduction to Physical Polymer Science* (Wiley-Interscience, New Jersey, 2006)

[2] Baur, J. & Silverman, E. Challenges and opportunities in multifunctional nanocomposite structures for aerospace applications. *MRS Bull.* **32**, 328-334 (2007).

[3] Winey, K. I., Kashiwagi, T. & Mu, M. F. Improving electrical conductivity and thermal properties of polymers by the addition of carbon nanotubes as fillers. *MRS Bull.* **32**, 348-353 (2007).

[4] Kim, P., Shi, L., Majumdar, A. & McEuen, P. L. Thermal transport measurements of individual multiwalled nanotubes. *Phy. Rev. Lett.* **87**, 215502 (2000).

[5] Moniruzzaman, M. & Winey, K. I. Polymer nanocomposites containing carbon nanotubes. *Macromolecules* **39**, 5194-5205 (2006).

[6] Huxtable, S. T. *et al.* Interfacial heat flow in carbon nanotube suspensions. *Nat. Mater.* **2**, 731-734 (2003).

[7] Kanamoto, T., Tsuruta, A., Tanaka, K., Takeda, M. & Porter, R.S. Superdrawing of ultrahigh molecular-weight polyethylene .1. effect of techniques on drawing of single-crystal mats. *Macromolecules* **21**, 470-477 (1988).

[8] Choy, C. L., Wong, Y. W., Yang, G. W. & Kanamoto, T. Elastic modulus and thermal conductivity of ultradrawn polyethylene. *J. Polym. Sci. Part B: Polym. Phys.* **37**, 3359-3367 (1999).

[9] Henry, A. & Chen, G. High thermal conductivity of single polyethylene chains using molecular dynamics simulations. *Phys. Rev. Lett.* **101**, 235502 (2008).

[10] Fermi, E., Pasta, J. & Ulam, S. Studies of nonlinear problems. *Los Alamos Report* No. LA1940 (1955).

[11] Wang, Z., Carter, J. A., Lagutchev, A., Koh, Y. K., Seong, N., Cahill, D. G. & Dlott, D. D. Ultrafast flash thermal conductance of molecular chains. *Science* **317**, 787-790 (2007).

[12] Wang, R.Y., Segalman, R. A. & Majumdar, A. Room temperature thermal conductance of alkanedithiol self-assembled monolayers. *Appl. Phys. Lett.* **89**, 173113 (2006).

[13] Chae, H. G. & Kumar, S. Making strong fibers. *Science* **319**, 908-909 (2008).

[14] Smith, P. & Lemstra, P. J. Ultra-high-strength polyethylene filaments by solution spinning/drawing. *J. Mater. Sci.* **15**, 505-514 (1980).

[15] Choy, C. L., Fei, Y. & Xi, T.G. Thermal-conductivity of gel-spun polyethylene fibers. *J. Polym. Sci. Part B: Polym. Phys.* **31**, 365-370 (1993).

[16] Poulaert, B., Chielens, J. C., Vandenhende, C., Issi, J. P.& Legras, R. Thermal conductivity of highly oriented polyethylene fibers. *Polym. Commun.* **31**,148-151 (1990).

[17] Fujishiro, H., Ikebe1, M., Kashima, T. & Yamanaka, A. Drawing effect on thermal properties of high-strength polyethylene fibers. *Jpn. J. Appl. Phys.* **37**, 1994-1995 (1998).

[18] Harfenist, S. A., *et al.* Direct drawing of suspended filamentary micro- and nanostructures from liquid polymer. *Nano Lett.* **4**, 1931-1937(2004).

[19] Nain, A. S., Amon, C. & Sitti, M. Proximal probes based nanorobotic drawing of polymer micro/nanofibers. *IEEE Trans. Nanotechnol.* **5**, 499-510 (2006).

[20] Smith, P., Chanzy, H. D. & Rotzinger, B. P. Drawing of virgin ultrahigh molecular-weight polyethylene - an alternative route to high-strength high modulus materials .2. influence of polymerization temperature. *J. Mater. Sci.* **22**, 523-531 (1987).

[21] Majumdar A. Scanning thermal microscopy. *Annu. Rev. Mater. Sci.* **29**, 505-585 (1999).

[22] Barnes, J. R., Stephenson, R. J., Welland, M. E., Gerber, C. & Gimzewski, J. K. Photothermal spectroscopy with femtojoule sensitivity using a micromechanical device. *Nature* **372**, 79-81 (1994).

[23] Shi, L. & Majumdar, A. Thermal transport mechanisms at nanoscale point contacts *J. Heat Transfer* **124**, 329-337 (2002).

[24] Marla, V. T., Shambaugh, R. L. & Papavassiliou, D. V. Use of an infrared camera for accurate determination of the temperature of polymer filaments. *Ind. Eng. Chem. Res.* **46**, 336-344 (2007).

[25] Fujikura, Y., Suzuki, T. & Matsumoto, M. Emissivity of chlorinated polyethylene. *J. Appl. Polym. Sci.* **27**, 1293-1300 (1982).

[26] Modest, M. *Radiative Heat Transfer* (Academic Press, 2003).

[27] Shen, S., Narayanaswamy, A., Goh, S. & Chen, G. Thermal conductance of bimaterial microcantilevers. *Appl. Phys. Lett.* **92**, 63509 (2008).

[28] Lai, J., Perazzo, T., Shi, Z., & Majumda A. Optimization and performance of high-resolution micro-optomechanical thermal sensors. *Sens. Actuators A* **58**, 113 (1997).

[29] Mills, A. F. *Heat Transfer*, 2nd ed. (Prentice Hall, NJ, 1999).

[30] Peterlin, A. Drawing and extrusion of semi-crystalline polymers. *Coll. & Polym. Sci.* **265**, 57-382 (1987).

[31] Van Aerle, N. A. J. M. & Braam, A. W. M. A structural study on solid state drawing of solution-crystallized ultra-high molecular weight polyethylene. *J. Mater. Sci.* **23**, 4429-4436 (1988).

[32] Shen, S., Henry, A., Tong, J., Zheng, R. T. & Chen, G. Polyethylene nanofibres with very high thermal conductivities. *Nature Nano.* **5**, 251-255 (2010).

Chapter 6 : Summary and future directions

6.1 Summary

By developing new experimental techniques based on bi-material cantilevers used in the Atomic Force Microscopes (AFM), this thesis has studied several extraordinary energy transfer phenomena at the nanoscale including near-field radiation beyond Planck's law (Chapter 3), the optical absorption of micro/nanostructures (Chapter 4) and high thermal conductivity polymers (Chapter 5).

Blackbody radiation, as predicted by Planck's law, is usually treated as the maximum thermal radiation emitted by an object. Theoretical calculations show that surface phonon polaritons can lead to a breakdown of the Planck's blackbody radiation law in the near field. Surface phonon polaritons are demonstrated in this thesis to enhance energy transfer between two surfaces at small gaps by measuring radiation heat transfer between a microsphere and a flat surface down to 30 nm separation. The corresponding

heat transfer coefficients at nanoscale gaps are three orders of magnitude larger than that of the blackbody radiation limit. This work will have practical impacts in areas such as thermophotovoltaic energy conversion, radiative cooling, and magnetic data recording.

Bulk polymers are generally poor thermal conductors and have a typical thermal conductivity of ~ 0.1 W/m.K. A new technique is developed to fabricate ultra-drawn polyethylene nanofibers. Using the AFM cantilever as a new measurement platform, we demonstrate that these ultradrawn nanofibers can have a thermal conductivity of along the fiber direction as high as ~ 100 W/m.K, which is about a 3 orders of magnitude enhancement compared to bulk polymers. Such high thermal conductivity polymers can potentially provide a cheaper alternative to conventional metal-based heat transfer materials that are used extensively throughout a variety of industries and applications.

The optical properties of nanostructured solar cells over the solar spectrum are crucial for their performance. Previous research measured the optical absorption of individual nanostructures by indirectly measuring their photocurrent. An experimental setup is presented to directly measure the spectral absorption of individual micro/nanostructures in applications to solar photovoltaics. Further refinement on experimental technique and characterization using the platform will guide the optimization of dimension, shape, and materials selections of nanostructures in order to maximize the efficiencies of solar cells.

6.2 Future directions

Theory has predicted that at extremely small gaps (< 5 nm), near-field radiation saturates with a decrease in gap size due to the non-local effects of dielectric functions [1]. Technically, atomically smooth surfaces with a surface roughness less than 1 nm are achievable. By minimizing the vibrations inside a vacuum chamber, it is possible to use the present experimental setup to demonstrate the non-local effects and the saturation of near-field radiation at a gap of less than 5 nm. To extend the present measurement to other configurations, the measurement of the near-field radiation between two spheres is also feasible, though the alignment between two spheres is difficult. Instead of using proximity theory in the sphere-plate problem, the experimental results for the two-sphere problem can be compared with the numerical calculations conducted by Narayanaswamy [2].

Though we demonstrate that the ultradrawn polyethylene nanofibers can have a very high thermal conductivity, the physics of the heat conduction in the nanofibers has not been fully understood. For nanofibers with small diameters (for example, 10 nm in diameter), the boundary scattering of phonons may dominate the heat conduction along the nanofiber. It will be very interesting to measure the thermal conductivity of nanofibers under low temperatures (1-100 K) and their temperature and size dependences. To optimize the present experimental setup for measuring the thermal conductivity of nanofibers, the temperature of the micro thermocouple can be modulated by using a periodic heating. Then, a lock-in amplifier is used to measure the bending of the cantilever and thus increase the sensitivity of the technique.

Some preliminary results about the optical absorption of micro/nanostructures are presented in this thesis. The present experimental setup has the potential to directly measure the optical absorption of a single nanowire. The next step is to measure the optical absorption of single nanowires with different sizes, incidence angles of light, *etc.*, and compare the measurement with the predictions from Mie theory.

6.3 References

[1] Chapuis, P.-O., Volz, S., Henkel, C., Joulain, K. & Greffet, J.-J. Effects of spatial dispersion in near-field radiative heat transfer between two parallel metallic surfaces. *Phys. Rev.* B **77**, 035431 (2008).

[2] Narayanaswamy, A. & Chen, G. Thermal near-field radiative transfer between two spheres. *Phys. Rev. B* **77**, 075125 (2008).